Magnetic Resonance Experiments on Doped Single Crystals Sodium Chloride and Potassium Cobalt Hexacyanide

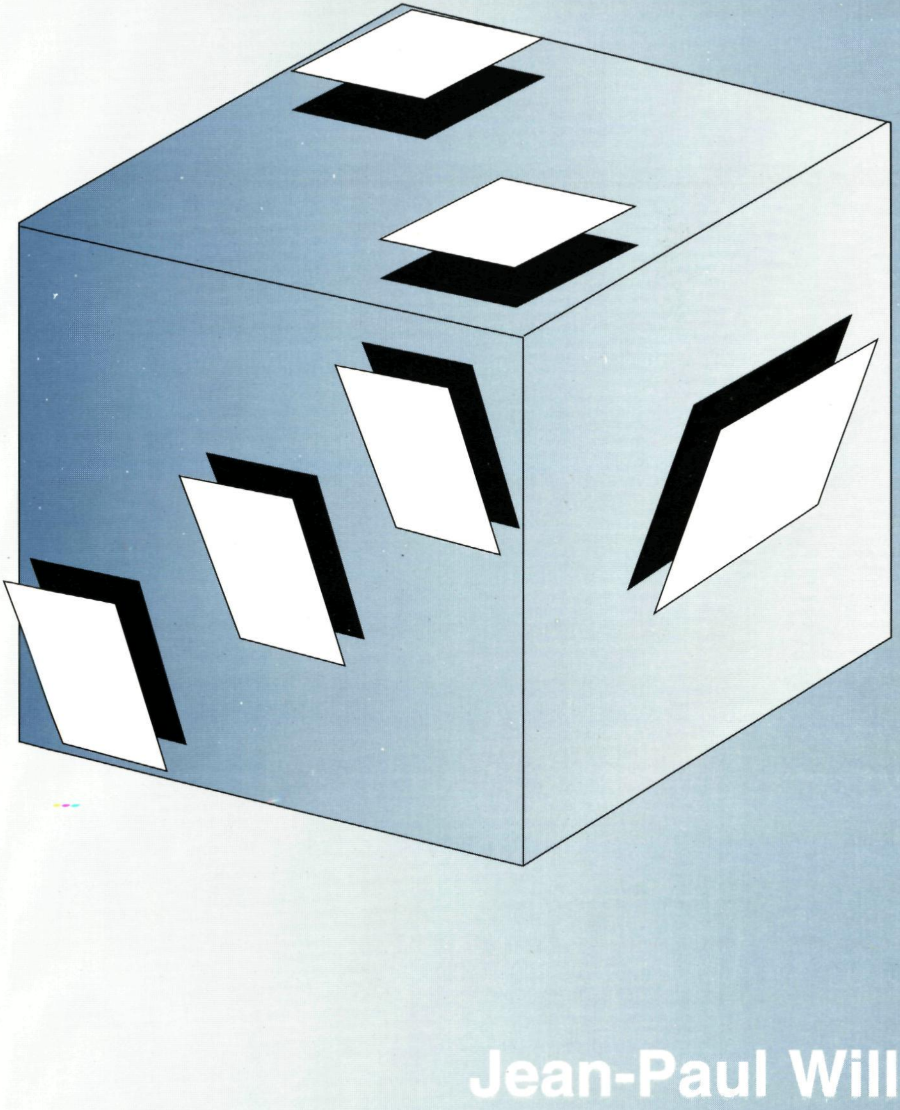

Jean-Paul Willems

Magnetic Resonance Experiments on Doped Single Crystals of Sodium Chloride and Potassium Cobalt Hexacyanide

Bij de omslag:
De kristalstuctuur van Natrium Chloride (keukenzout) is zeer goed bekend: een éénkristal van dit materiaal is opgebouwd uit kleine kubussen. De kristalstuctuur van Kalium Kobalt Hexacyanide is minder eenduidig: een éénkristal kan zijn opgebouwd uit rechthoekige blokken, maar ook uit parallellopipeda. Voorafgaand aan het schrijven van dit proefschrift zijn éénkristallen van deze laatste genoemde verbinding onderzocht die zijn opgebouwd uit kleine parallellopipeda, uit 'grote' parallellopipeda (drie maal groter dan de kleine) en uit rechthoekige blokken. Vooralsnog is de uitkomst van het groeiproces voor dit soort kristallen even (on)voorspelbaar als het resultaat van een te werpen dobbelsteen.

Note to the cover:
The crystal structure of Sodium Chloride (kitchen salt) is very well known: a single crystal of this compound is composed of small cubes. The crystal structure of Potassium Cobalt Hexacyanide is less unambiguous: a single crystal can either be built by rectangular blocks, or by parallelopipeda. Preceding writing this thesis, single crystals of former compound have been investigated which were built by small parallelopipeda, by 'large' parallelopipeda (three times as large as the small ones) and by rectangular blocks. Until now, the result of the growing process of these kind of crystals is as (un)predictable as the result of a dice which will be turned.

Cover design (in random order): Jean-Paul Willems, Adri Klaassen en Geert-Jan van Moorsel.
Technical realisation: Ton de Best (UDN)

Magnetic Resonance Experiments on Doped Single Crystals of Sodium Chloride and Potassium Cobalt Hexacyanide

een wetenschappelijke proeve op het gebied van de Natuurwetenschappen

Proefschrift

ter verkrijging van de graad van doctor
aan de Katholieke Universiteit Nijmegen,
volgens besluit van het College van Decanen
in het openbaar te verdedigen op
maandag 24 april 1995 des namiddags te 1.30 uur precies

door
Adrianus Paulus Rudolfus Maria Willems
geboren 27 juni 1967 te Nijmegen

Universiteits Drukkerij Nijmegen

Promotor: Prof. Dr. E. de Boer

ISBN 90-9008075-9

Voorwoord

Omdat het werk dat ik de afgelopen vier jaar op de afdeling Mol. Spec. heb verricht, beslist geen solo actie is geweest, wil ik van deze gelegenheid gebruik maken om een aantal mensen te bedanken. Hoewel zeer velen op een directe of indirecte manier hebben bijgedragen tot de totstandkoming van dit boekje, kan ik er maar een beperkt aantal met name noemen:

Allereerst professor *de Boer* die mij gedurende vier jaar heeft begeleid. Een deel van deze begeleiding bestond er uit om mij te leren mijn uiterst summiere taalgebruik te vervangen door een woordkeus die minder inspanning zou vergen van de lezer/toehoorder.

Desiree van der Wey ben ik zeer erkentelijk omdat zij, als secretaresse, een onmisbare steun is en vraagbaak voor alle zaken die maar enigszins samenhangen met het reilen en zeilen van de afdeling.

De technici van de afdeling, *Adri Klaassen* en *Gerrit Janssen*, wil ik bedanken voor de hulp, de adviezen en het commentaar (al of niet op technisch gebied) die ik van hen heb ontvangen.

Niet in de laatste plaats gaat mijn dank uit naar *Fer Derksen* (Selfservice Instrumentmakerij) die altijd klaar stond met hulp, advies en droge humoristische opmerkingen, wanneer ik weer wat te draaien en/of te frezen had.

Nu ik toch in de technische hoek zit: *Rob Kasman*, *Wim Schut* en alle leden van de Service Instrumentmakerij, bij deze nogmaals mijn dank! *Piet Hombergen* wil ik bedanken voor het vervaardigen van de resonator die beschreven is in hoofdstuk 4, *Eef Janssen* ben ik erkentelijk voor de moeite die hij heeft getroost bij het maken van ENDOR spoeltjes, en de magazijnmeester *Giel van Hoorn* bij deze bedankt voor de coulante service.

Dit boekje zou nooit in ongeveer vier jaar tot stand zijn gekomen als ik geen hulp had gehad van *Marcel Clephas*, die mij gedurende een jaar heeft geholpen als student. In dit jaar werd de basis gelegd voor de laatste twee hoofdstukken in dit proefschrift, Marcel bedankt!

Ed Reijerse wil ik bedanken voor het kritisch doorlezen van dit manuscript.

Reinhart Kirmse möchte ich danken weil er der inhalt dieses dissertation controliert hatte. Ich bin ihm dankbar für die gastliche aufnahme damals in Leipzig.

I would like to express my gratitude to *Deming Wang* who initiated the EPR research on $Fe(CN)_6^{3-}$ doped into single crystals at this department.

Mijn collega promovendi: *Pieter van Dam*, *André van der Pol*, *Ernst van Eck* en *Jaap Shane* (afdeling Mol. Spec.), *John Michiels* en *Michiel van Buuren* (afdeling SSS), wil ik bedanken voor de goede sfeer op de afdeling en hun vele (on)gevraagde, nuttige en nutteloze opmerking.

Professor van der Avoird en *Harry Sommerdijk* ben ik erkentelijk voor de theoretische

berekeningen die zij hebben uitgevoerd.
Last but not least wil ik *Wilko Konings* (MTS stagiaire), *Geert-Jan van Moorsel*, *Marcel Franse* en *Michiel van der Meer* (ex-student/studenten) bedanken omdat zij bijgedragen hebben aan de levendige sfeer, die Mol. Spec. zo typeert.

Saudacões	*Greetings!*
Dá licénca um momento	*Excuse me, one moment*
Te lembró	*I remind you*
Que amanhã	*That tomorrow*
Será tudo ou será nanoua	*It will be all or it will be nothing*
Depence	*It depends*
Será breve ou será grande	*It will be brief or it will be great*
Depende da paixão	*It depends on the passion*
Será sujo, será sonho	*It will be dirty, it will be a dream*
Cuidado	*Be carefull*
Será útil, será tarde	*It will be useful, it will be late*
Se esmera	*Do your best*
E confia	*And have trust*
Na força do amanhã	*In the power of tomorrow*

Based on "Spirit voices", by Paul Simon

Voor mijn ouders

Manuscriptcommissie: Dr. E. J. Reijerse
Prof. Dr. R. Kirmse

Contents

Chapter 1

Introduction

Magnetic resonance techniques are excellently suitable to obtain information about the structure of a material, because they are non-destructive. The experiments described in this thesis are performed on diamagnetic crystals which are doped by small amounts of paramagnetic material. Only the paramagnetic atoms are detectable by utilising magnetic resonance techniques, the host material is invisible. It seems strange that one is able to obtain information about material which is undetectable. In order to explain this apparent contradiction, the paramagnetic atoms in the diamagnetic host can be compared with small lamps in a dark environment. Figure 1.1 shows a satellite photograph of a small part of Europe, showing bright spots in a dark background. These light spots are caused

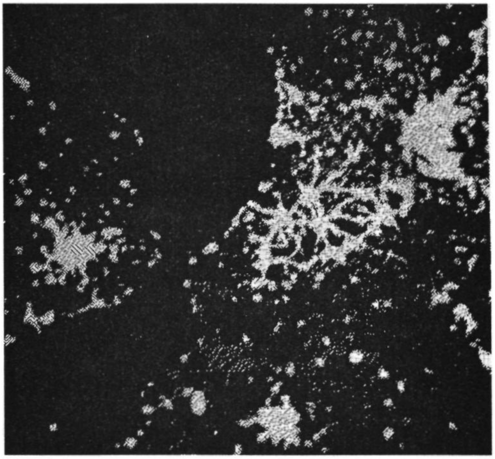

Figure 1.1
A satellite photograph, made by the Landsat satellite, of a small part of Europe. The figure shows a part of the UK (left), the northern part of France (bottom), the western part of Germany (right) and The Netherlands (top). The bright spots are caused by the (city)lights on the surface. Notice that the major cities are visible by a large blot: Paris is visible in the lower part, London is discernible in the left of the figure. Note that the highways in Belgium are lighted at night, so that they appear as bright lines in the figure.

by lights on the surface of the earth. It is evident that these bright spots are not randomly distributed over the figure: the positions of some major cities as London and Paris are clearly observable by the blotches. Thus, such a figure reveals information about the structure on the surface of this part of Europe. Like the bright spots in the figure, the paramagnetic atoms in the diamagnetic host, are not randomly organised. In a similar manner as the spots displayed in the figure, the positions of the paramagnetic atoms reveal information about the structure of the doped material.

Figure 1.1 presents general structural information, but a detailed picture about the local structure of, for instance a single city, can be obtained by an analogous procedure. In a similar manner, general structural data can be revealed using one type of magnetic resonance technique, and local structural facts are acquired by employing another kind of resonance technique.

This thesis reports about the results obtained by performing single-crystal studies on the paramagnetic complex $Fe(CN)_6^{3-}$, doped into various diamagnetic hosts. By utilising magnetic resonance techniques, information could be obtained about the general structure of the host crystal and about the local structure in the direct neighbourhood of the $Fe(CN)_6^{3-}$ complex.

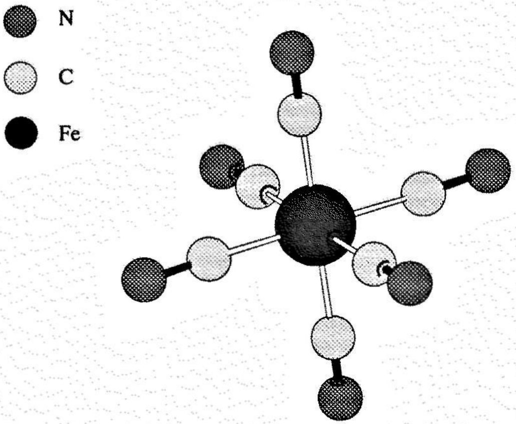

Figure 1.2
The $Fe(CN)_6^{3-}$ complex.

Potassium iron hexacyanide may be known under the name of 'red prussian of potash'. This compound is/was used for the preparation of 'Berlin Blue' (Fe(III)$Fe(CN)_6$): a colour pigment for printing devices. From a technological point of view, $Fe(CN)_6^{3-}$ is interesting because it can be used in semi-conductor materials [1]. However, the reason for taking this compound as a dope material lies only secondarily in the technological aspects. The major reason can be found in the fact that it is an excellent model system for several hexa coordinated 3d transition-metal complexes, which are present in e.g. proteins. The former argument was one of the motivations for performing the experiments described in chapters 5 and 6.

$Fe(CN)_6^{3-}$ is quite suitable as a dope compound in materials/crystals which are investigated by means of magnetic resonance techniques. Because it is a low spin complex, it facilitates the interpretation of the spectra. This property makes the complex suitable as a 'spin marker', as has been done in the experiments reported in chapters 7 and 8. Utilising this spin marker, information can be obtained about the local structure in the direct environment of the iron complex (chapter 8), but it also yields information about the general structure of the doped crystal. Note that in these last two chapters, attention will be paid mainly to the host crystal, whereas in chapters 5 and 6 the complex itself will be concerned.

Chapter 4 differs from the rest of the chapters in this thesis, because it describes one of the 'technological' aspects of the experiments. The properties of a resonator which is used to perform the experiments of chapters 5 to 7 will be considered in this chapter.

References

[1] Rader, W.S., Solujio, I., Milosavljevic, F.R., Hendrix, J.I., and Nelson, J.H., 1993, *Environmental Science & Technology*, **27**, 1875

Chapter 2

Theoretical Foundations

Electron Paramagnetic Resonance (EPR) is a technique which is specifically suitable for determining the electron distribution around a paramagnetic centre. Several types of magnetic interactions can be determined such as the electron Zeeman interaction, the hyperfine interaction and the nuclear quadrupole interaction. By determining these interactions, information can be obtained about e.g. the delocalisation of the unpaired electron and about the electric field gradient. To reveal this information the g, hyperfine[1] and quadrupole tensors have to be resolved. The hyperfine and the nuclear quadrupole interactions manifest themselves through splittings in the EPR spectrum. In some cases, however, these splittings are too small to be detected by EPR. This will be the case if the hyperfine splitting falls within the EPR linewidth. Other spectroscopic techniques like ENDOR (Electron Nuclear Double Resonance) or ESEEM (Electron Spin Echo Envelope Modulation) are especially suitable in these situations. Although ENDOR and ESEEM are rather similar concerning their possibilities to detect small couplings, their theoretical frameworks differ significantly. A remarkable result of this difference is that both techniques are complementary. In this thesis both ENDOR and ESEEM experiments are described, therefore a brief qualitative description will be given about the theoretical concepts of ENDOR as well as that of ESEEM.

2.1 ENDOR

There are a number of text books [1-5] which extensively describe the theoretical basics of ENDOR. In this section only a short introduction will be given, necessary to understand the experimental difficulties encountered when designing an ENDOR cavity as described in chapter 4 and to understand the experimental possibilities of ENDOR as described in the fifth and sixth chapters of this thesis.

The fundamentals of ENDOR can best be described by taking the example of a simple four level system ($S=\frac{1}{2}$, $I=\frac{1}{2}$). The energy levels of this system can be obtained by solving the Hamiltonian:

$$\mathcal{H} = \beta_e\, \vec{B}_0 \cdot \bar{\bar{\mathrm{g}}} \cdot \vec{S} + \vec{S} \cdot \bar{\bar{\mathrm{A}}} \cdot \vec{I} - g_n\, \beta_n\, \vec{B}_0 \cdot \vec{I}.$$

---

[1] Strictly according to the mathematical definition, the expressions 'g tensor' and 'hyperfine tensor' are not correct, see section 2.5.

If the system is in thermal equilibrium, the Boltzmann distribution holds for the electron population ratio over these four levels (see figure 2.1a and equation 2.1):

$$\frac{N3}{N2} = \frac{N4}{N1} = e^{-\Delta E/kT} \approx 1 - \frac{\Delta E}{kT} \equiv 1 - \varepsilon. \tag{2.1}$$

During a normal EPR experiment microwave radiation is used to excite electrons from level 1 to level 4. In case the 1↔4 transition is saturated, the population density of level 4 (N4) equals the population density of level 1 (N1) see figure 2.1b: the EPR signal decreases. If in this situation, the electrons from level 4 are excited to level 3 by means of radio frequency (RF) radiation, the saturation is (partially) lifted because the electrons in level 4 are offered a second relaxation path to level 1 through the 4↔3 transition (using the RF radiation) and the 3↔1 transition (via the cross relaxation), see figures 2.1c and 2.2. The cross-relaxation time should be less than the nuclear-relaxation time in this case, hence the relaxation path involving a nuclear relaxation can be ignored. This relation is generally found for paramagnetic centres in solids. For radicals in solution, one generally finds another relaxation path: via 4↔3 transition (using the RF radiation), the

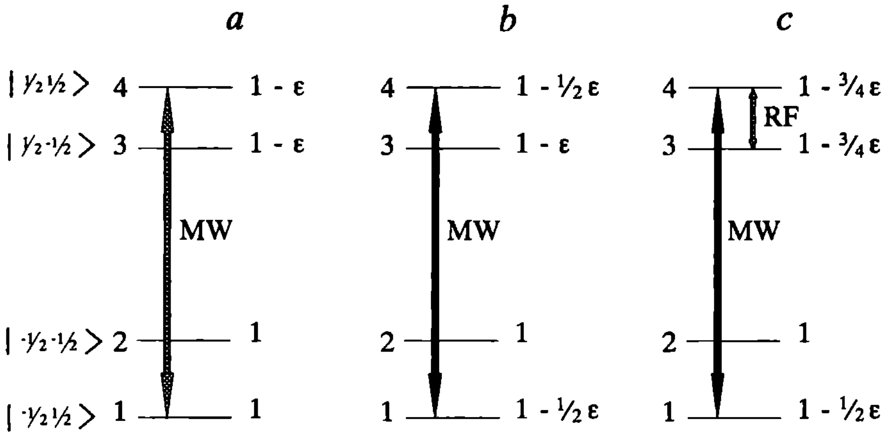

Figure 2.1
In these figures the symbol ε equals $\frac{\Delta E}{kT}$ and the characters MW denote the microwave radiation.
a: The relative population distribution over the energy levels when the EPR transition is not saturated. It is assumed that the two lowest levels are equally populated: the population of these levels is assumed to be 1.
b. The relative population distribution over the energy level when the EPR transition is saturated: the levels 1 and 4 become equally populated.
c: The relative population distribution over the energy level when an RF frequency is applied on the transition 3↔4. The microwave power is the same as in figure 'b'. As a result of the RF frequency the population of level 4 diminishes, so the saturation of the EPR transition 1↔4 is (partially) lifted.

3↔2 transition (through the electron spin relaxation) and the 2↔1 transition (using the nuclear relaxation). In this case, the nuclear-relaxation time is smaller than the cross-relaxation time. Thus, the relaxation path containing a cross relaxation can be neglected. This thesis reports on the (ENDOR) results found for paramagnetic centres in solids, so in the following parts of this thesis the relaxation path containing a nuclear relaxation time will be disregarded.

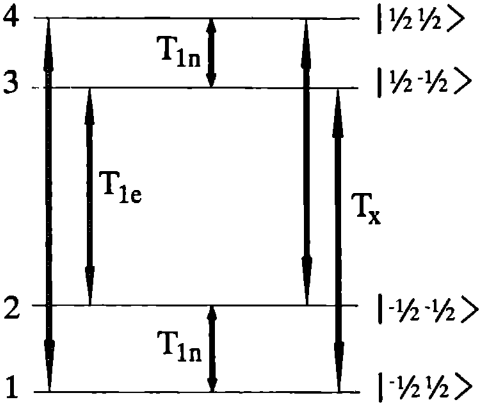

Figure 2.2
The three most important relaxation times: The electron-relaxation time T_{1e}, the nuclear-relaxation time T_{1n} and the cross-relaxation time T_x.

If the saturation of the EPR transition is lifted, the intensity of the EPR signal will increase. This increased intensity of the saturated EPR signal is the measured ENDOR signal. The ENDOR signal intensity amounts just a few percent of the intensity of the EPR signal. This simple example shows already four basic demands necessary for doing ENDOR:

- The signal to noise ratio of the EPR signal should be as good as possible, since it is directly related to the signal to noise ratio of the ENDOR signal.

- An EPR signal has to be saturable. This means that the electron spin relaxation time T_{1e} has to be relatively long. For solids at room temperature T_{1e} is in the order of microseconds, which usually is too short. The electron spin relaxation process can be retarded by cooling the sample.

- The cross-relaxation time T_x has to be comparable to the relaxation time T_{1e}. If this time is too long the population in the levels 1, 4 and 3 will become equal when applying an RF frequency: the EPR transition 1↔4 will still be saturated and the EPR signal will not show an increase in intensity so an ENDOR signal will be undetectable.

- The nuclear-relaxation time T_{1n} should not be too small. If this relaxation time is small, the population in levels 3 and 4 will become equal even in the absence of RF radiation. For solids at room temperature T_{1n} is in the order of seconds.

In practice these demands make ENDOR only possible in a narrow temperature window.

For a system with $S=\frac{1}{2}$ and $I=\frac{1}{2}$ the ENDOR spectra can be described by the spin Hamiltonian:

$$\mathcal{H} = \beta_e \vec{B}_0 \cdot \bar{\bar{g}} \cdot \vec{S} + \vec{S} \cdot \bar{\bar{A}} \cdot \vec{I} - g_n \beta_n \vec{B}_0 \cdot \vec{I}.$$

For an isotropic hyperfine tensor the two ENDOR frequencies (ν_+ and ν_-) are given by:

$$\begin{aligned} \nu_\pm &= \left| \frac{A}{2h} \pm \frac{g_n \beta_n B_0}{h} \right| \\ &\equiv \left| \frac{A}{2h} \pm \nu_l \right|, \end{aligned} \tag{2.2}$$

where ν_l is the Larmor frequency.

This equation shows that the ENDOR lines can be centred around $\frac{1}{2}$A while the splitting between the lines amounts $2\nu_L$. This occurs if $\frac{A}{2h} \geq \nu_L$. If $\frac{A}{2h} \leq \nu_L$ the ENDOR lines are centred around ν_L while the splitting between the lines measures A/h.

2.2 Enhancement effect

The RF field acting upon the nuclear spin can be larger than the external applied RF field $\vec{B}_2$ due to the so called enhancement effect. In this section a classical explanation of this effect will be given [4]. If the hyperfine tensor (A) is isotropic, the spin vector (S_z) will align (anti)parallel to the external applied magnetic field ($\vec{B}_0$). The hyperfine tensor will induce a magnetic field $\vec{B}_n$ near the nucleus which is (anti)parallel to $\vec{S}_z$ (see figure 2.3). This magnetic field $\vec{B}_n$ can be expressed in terms of the hyperfine coupling by rewriting the hyperfine energy term in a form of a nuclear Zeeman interaction, as follows:

$$\begin{aligned} S_z A I_z &= -g_n \beta_n B_n I_z \\ \Rightarrow B_n &= \frac{-A m_s}{g_n \beta_n}. \end{aligned} \tag{2.3}$$

If an RF field ($\vec{B}_2$) is applied perpendicular to $\vec{B}_0$, $\vec{S}_z$ and thus $\vec{B}_n$ will align (anti)parallel to the direction of the resulting external field (see figure 2.3b). The magnetic field $\vec{B}_n$ can be separated into a component parallel to the RF field ($\vec{B}_{n2}$) and into a component parallel to $\vec{B}_0$ ($\vec{B}'_n$). It is evident that

$$\frac{B_2}{B_0} = \frac{B_{n2}}{B'_n} \approx \frac{B_{n2}}{B_n} \quad (B'_n \gg B_{n2}). \tag{2.4}$$

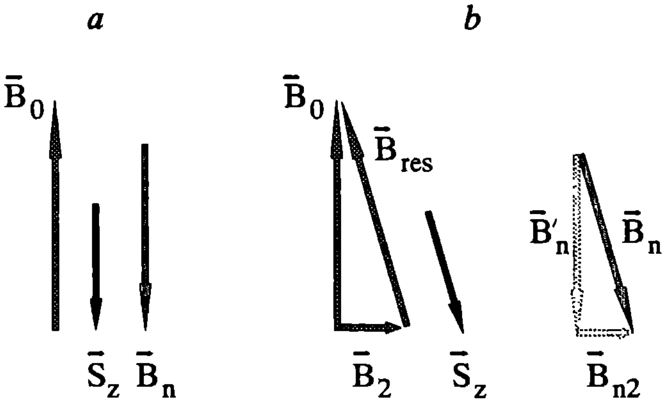

Figure 2.3
a: If the RF field is absent, the spin vector $\vec{S}_z$ and thus the induced magnetic field at the position of the nucleus $\vec{B}_n$ are aligned (anti)parallel to the external magnetic field $\vec{B}_0$.
b: If the RF field $\vec{B}_2$ is present, the spin vector, and consequently, $\vec{B}_n$ are aligned parallel to the resulting field of $\vec{B}_0$ and $\vec{B}_2$, $\vec{B}_{res}$.

Combining former equations, one finds for the total RF field at the nucleus (B_2^{tot}):

$$B_2^{tot} = B_2 + B_{n2} = B_2 \left| 1 - \frac{m_s A}{g_n \beta_n B_0} \right| . \tag{2.5}$$

From equation 2.5 it can be inferred that the enhancement effect is larger as the nuclear g factor (g_n) is smaller. It is also noteworthy that the enhancement is absent for $m_s = 0$ which can be important for triplet states. From equation 2.5 it can also be deduced that the intensity of the ENDOR lines generally increases with increasing frequency, provided that g_n is positive, because for the high frequency ENDOR lines the relation $m_s A < 0$ holds. The derivation as followed above is only valid if the hyperfine tensor is isotropic, because if the hyperfine tensor is anisotropic, the electron spin vector is not necessarily directed parallel to the external magnetic field and the magnitude of $\vec{B}_n$ will no longer be given by equation 2.3.

2.3 Triple resonance

In an ENDOR experiment the saturation of an EPR transition is (partially) lifted by exciting an NMR transition, thereby creating an additional relaxation pathway via an NMR transition and a cross relaxation. The intensity of an ENDOR line could be enhanced if another relaxation pathway could be opened which would bypass the cross relaxation. This can only be done if a second NMR transition is excited by an additional RF frequency. Thus, triple resonance utilises two independent RF frequencies and one microwave frequency in order to create an efficient relaxation pathway, resulting in an enhancement of the signal intensity belonging to the NMR transition(s).

Employing two independent RF frequencies, it is possible to excite two NMR transitions belonging to the same atom (this is called special triple resonance), but it is also possible to excite two NMR transitions belonging to different atoms (called general triple resonance)

Special triple resonance

Special triple resonance can be explained by taking the example of a four level system: one electron (S = $\frac{1}{2}$) and one nucleus with a nuclear spin of I = $\frac{1}{2}$. The ENDOR spectrum of this system contains two lines centred around the Larmor frequency (in case $\frac{A}{2h} < \nu_I$, see equation 2.2). If both RF frequencies are initially set at the Larmor frequency and subsequently both frequencies are simultaneously swept in opposite directions (one is swept to higher values, the other one is swept to lower values) then these frequencies will simultaneously excite an NMR transition: one RF frequency will excite an NMR transition belonging to the $m_s = +\frac{1}{2}$ manifold, the second RF frequency will excite an NMR transition belonging to the m_s = -$\frac{1}{2}$ manifold. When this happens an additional and efficient relaxation path is created which does not contain a cross relaxation:

> The EPR transition is excited by the microwave radiation.
>
> An NMR transition is excited by one of the RF frequencies.
>
> The system relaxes using T_{1e} relaxation.
>
> The second NMR transition in the other m_s manifold, is excited by the second RF radiation, so that the system returns to its initial energy state.

Special triple resonance offers a few advantages compared to ENDOR:

- The sensitivity is enhanced because the efficiency of the relaxation path is increased.
- Because a special triple resonance experiment depends no longer critically on the cross-relaxation time, the temperature dependence of the experiment is reduced.

In the simple case discussed above one NMR transition will be observed at $\frac{A}{2h}$. In the general case, the spectrum of a special triple resonance experiment shows signals at frequency values corresponding to half the hyperfine values.

General triple resonance

The magnitudes of the hyperfine values can be determined by means of an ENDOR experiment, but the relative signs of the couplings cannot be assessed. These relative signs can be determined by applying general triple resonance. In the general triple resonance experiment, introduced by Biehl et al. [6] in 1975, one RF frequency is fixed at an NMR transition, while the other RF frequency is swept. If the second RF frequency excites an NMR transition, the original ENDOR signal can be either decreased or enhanced depending on the relative signs of the hyperfine values.

Figure 2.4 shows the energy level scheme of an eight level system, created by one electron ($S = \frac{1}{2}$) and two $I = \frac{1}{2}$ atoms; the hyperfine coupling constants and the nuclear g factors are taken positive. The hyperfine splitting due to atom 1 has been denoted as $\frac{1}{2}A_1$ and the hyperfine splitting caused by atom 2 as $\frac{1}{2}A_2$. In this example the nuclear spin of both atoms are equal, but triple resonance can also be performed on a system where different atoms are involved, having different nuclear g values and/or different nuclear spins. A level labelled '+ - +' in this figure belongs to an m_s state of $+\frac{1}{2}$, an m_I state of -$\frac{1}{2}$ for atom 1 and an m_I state for atom 2 of $+\frac{1}{2}$. In figure 2.4 the low frequency NMR transitions (which are degenerate) of atom 1 (+ - + ↔ + + +) and (+ - - ↔ + + -) are excited by means of a fixed RF frequency (labelled as 'Triple (fixed)' in the figure). All four EPR transitions are saturated by means of a microwave frequency (denoted as 'MW'), the second RF frequency is swept. If this swept frequency (not indicated in the figure) excites the high NMR transition of atom 1 (- + + ↔ - - +), an efficient relaxation path is opened, for instance:

> $- + + \leftrightarrow + + +$ (microwave frequency)
>
> $+ + + \leftrightarrow + - +$ (the fixed RF frequency excites the low frequency NMR transition of atom 1)
>
> $+ - + \leftrightarrow - - +$ (T_{1e} relaxation)
>
> $- - + \leftrightarrow - + +$ (the swept RF frequency excites the high frequency NMR transition of atom 1)

Note that this relaxation path only uses a T_{1e} relaxation: a relaxation path which uses a cross relaxation as in an ordinary ENDOR experiment is bypassed. Therefore, the signal intensity belonging to the high frequency NMR transition of atom 1 is enhanced compared to the signal intensity belonging to this transition in an ordinary ENDOR experiment.

If the swept RF frequency excites the high frequency NMR transition of atom 2, as is shown by figure 2.4, another relaxation path is opened which, again, bypasses the relaxation path containing a cross relaxation. For instance:

> The swept RF frequency induces a transition from the - + + level to the - + - level (the high frequency NMR transition of atom 2).
>
> The microwave radiation causes a transition from the - + - level to the + + - level.
>
> The fixed RF frequency creates a transition from the + + - level to the + - - level (the low frequency NMR transition of atom 1).
>
> Due to T_{1e} relaxation the system relaxes to the - - - level.
>
> The swept RF frequency induces a relaxation from the - - - level to the - - + level.

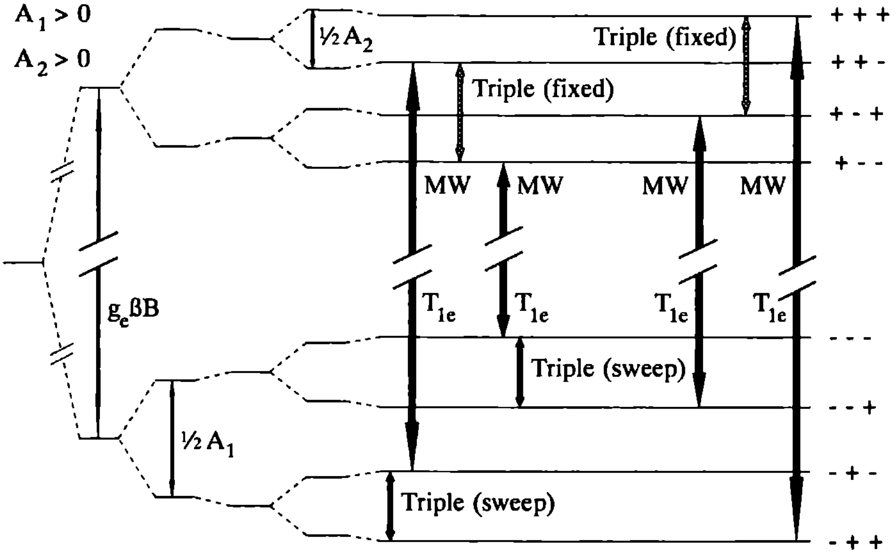

Figure 2.4
The fixed RF frequency induces the low frequency NMR transition of atom 1. The high frequency NMR transition of atom 2 is excited by the swept NMR transition. The indicated relaxation path does not contain a cross relaxation, so the signal intensity of the high frequency NMR transition of atom 2 is enhanced.

The microwave frequency invokes a transition from the - - + level to the + - + level.

A transition from the + - + level to the + + + level is induced by the fixed RF frequency.

The system relaxes to the initial energy level - + + by T_{1e} relaxation.

The result is that the signal intensity belonging to the high frequent NMR transition of atom 2 is enhanced.

A signal intensity can also be reduced as a consequence of the fixed triple frequency as is shown by figure 2.5. In this figure the energy levels of figure 2.4 are displayed: the population of the levels has been indicated like in figure 2.1. The figure shows that if the low frequency NMR transition of atom 1 (+++ ↔ +-+) is excited, the saturation of the EPR transition (-++ ↔ +++) is already (partially) lifted. In case the swept RF frequency excites the low frequency NMR transition of atom 2, the desaturation of the EPR transition is less efficient compared to an ordinary ENDOR experiment: the population of level +++ decreases by $\frac{1}{4}\varepsilon$ (from 1 - $\frac{1}{2}\varepsilon$ to 1 - $\frac{3}{4}\varepsilon$) in an ordinary ENDOR experiment (see figure 2.1), but is decreases only by $\frac{1}{8}\varepsilon$ (from 1 - $\frac{3}{4}\varepsilon$ to 1 - $\frac{7}{8}\varepsilon$) in a triple resonance experiment, see figure 2.5. This means that if the low frequency NMR transition

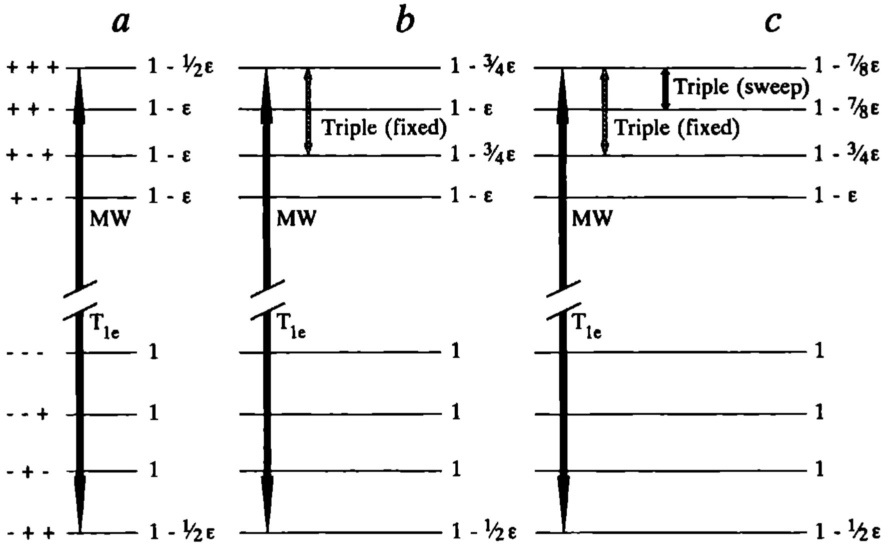

Figure 2.5
The energy level scheme of a system with one electron ($S = \frac{1}{2}$) and two atoms ($I = \frac{1}{2}$). The hyperfine coupling constants for both atoms have the same sign, so this energy level scheme is similar as that displayed in figure 2.4, but now the population of the levels has been indicated. Like in figure 2.1 the population of the lowest levels is assumed to be 1 and that of the highest levels is assumed to be 1 - ε, were $\varepsilon = \frac{\Delta E}{kT}$, provided that the system is in thermal equilibrium.
a The EPR transition has been saturated: the population of level -++ equals that of level +++.
b The saturation of the EPR transition is already (partially) lifted by the fixed RF frequency: the population of the levels +++ and +-+ are equal (this is the low frequency NMR transition of atom 2).
c Like in an ordinary ENDOR experiment, the swept RF frequency lifts the saturation of the EPR transition, but now the efficiency of the process of desaturation has been diminished. Therefore, the signal intensity belonging to the +++ ↔ ++- transition (the low frequency NMR transition of atom 1) decreases.

of atom 1 is excited by means of a fixed RF frequency, the intensity of the low frequency NMR transition of atom 2 decreases.

Figure 2.6 shows the energy level scheme in case the hyperfine values of atom 1 and 2 have opposite signs. As in figure 2.4 the high NMR transition of atom 1 is excited by a fixed RF frequency. In this case an efficient relaxation path can be opened if the high NMR transition of atom 2 is excited:

> The swept RF frequency creates a transition from the + + - level to the + + + level (the high frequency NMR transition of atom 2).

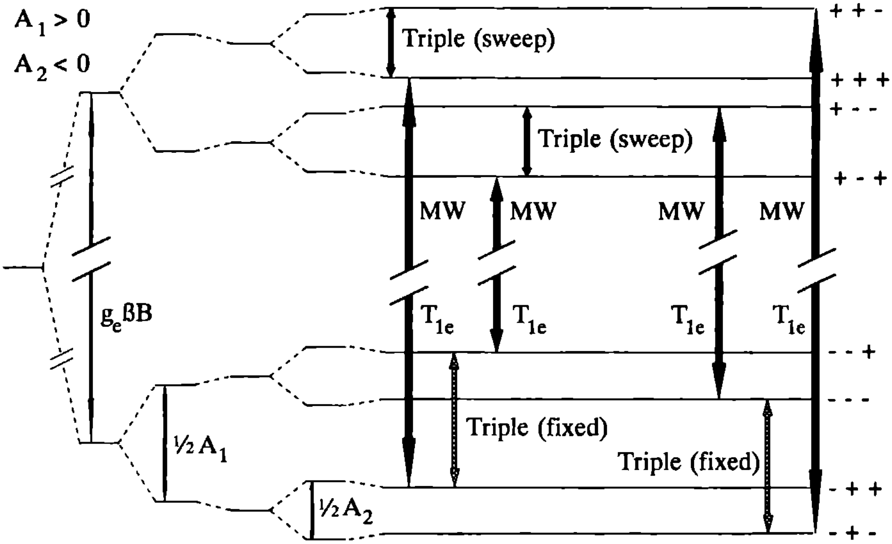

Figure 2.6
The high frequency NMR transition of atom 2 is excited by the swept NMR transition. The fixed RF frequency induces the high frequency NMR transition of atom 1. The indicated relaxation path does not contain a cross relaxation, therefore, the signal intensity of the high frequency NMR transition of atom 2 is enhanced.

The system relaxes to the - + + level by means of a T_{1e} relaxation.

The fixed RF frequency induces a transition from the - + + level to the - - + level (the high frequency NMR transition of atom 1).

The microwave radiation causes the transition from the - - + to the + - + level.

From the + - + level the system will be excited to the + - - level by the swept RF frequency.

By means of T_{1e} relaxation the system relaxes to the - - - level.

A transition from the - - - level to the - + - level is induced by the fixed RF frequency.

The system is excited to the initial energy level + + - by the microwave radiation.

The result is again, that the signal intensity belonging to the high frequent NMR transition of atom 2 is enhanced. According to the explanation given on page 15, one can deduce that the signal intensity of the low frequent NMR transition of atom 2 will be decreased.
These observations can be summarised as follows:

- If the low frequency NMR transition of atom 1 is excited, and the signal intensity belonging to the high frequency NMR transition of atom 2 is enhanced and the low frequency NMR transition of atom 2 is decreased, then the hyperfine values of the two atoms have equal signs. The signal intensity of the high frequency NMR transition of atom 1 is also enhanced.

- If the high frequency NMR transition of atom 1 is excited, and the signal intensity belonging to the high frequency NMR transition of atom 2 is enhanced and the signal intensity belonging to the low frequency NMR transition of atom 2 is decreased, then the hyperfine values of the two atoms have opposite signs. The signal intensity of the low frequency NMR transition of atom 1 is also enhanced.

Thus, a triple resonance experiment furnishes information about the relative signs of the hyperfine coupling constants. Note that the NMR transition which is excited by the fixed frequency, is always in another m_s manifold as the NMR transition which signal intensity is enhanced. Some nuclei like e.g. ^{15}N have a negative g_n value. If such nuclei are present in the system, the results of a triple resonance experiment may easily be misinterpreted. In this case the rules described above should be replaced by different ones, because the high frequency NMR transitions belong to a different m_s manifold.

2.4 ESEEM

ESEEM is a pulsed technique and is extensively described in numerous articles and textbooks [5,7,8]. Again a brief overview will be given in order to understand the ESEEM results described in chapter 8.

The fundamentals of ESEEM can best be described by taking again the example of a simple four level system ($S=\frac{1}{2}$, $I=\frac{1}{2}$). In this section the theory of ESEEM will be described in three different ways, each revealing a different aspect of the theory. The first and most simple description uses the intuition of the reader, the second uses a classical vector model, while the third and most thorough description makes use of the density operator formalism.

The intuitive approach

If the hyperfine interaction is anisotropic and the external magnetic field is not along one of the principal axes of the hyperfine tensor, the first order 'forbidden' transitions become 'permitted' to some extend. These 'forbidden' transitions are represented in figure 2.7 by the shaded arrows. A simple two-pulse ESEEM experiment will be described: $\frac{1}{2}\pi_y - \tau - \pi_y - \tau$-echo ($\pi_y$ denotes a π pulse around the y axis). The external magnetic field is assumed in the z direction. If the microwave field is strong enough to excite all spins, the spins will rotate in the xy plane after the first $\frac{1}{2}\pi_y$ pulse (see figure 2.8). The π_y pulse following the $\frac{1}{2}\pi_y$ pulse causes that spins from level 1 can be excited to level 4 (a permitted transition) but also to level 3 (a forbidden transition). Consequently, after

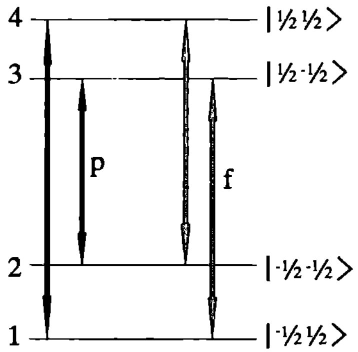

Figure 2.7
The transitions which are labelled 'p' are the permitted transitions ($\Delta m_i = 0$, $\Delta m_s = \pm 1$). The transitions which are labelled 'f' are the forbidden transitions ($\Delta m_i = \pm 1$, $\Delta m_s = \pm 1$).

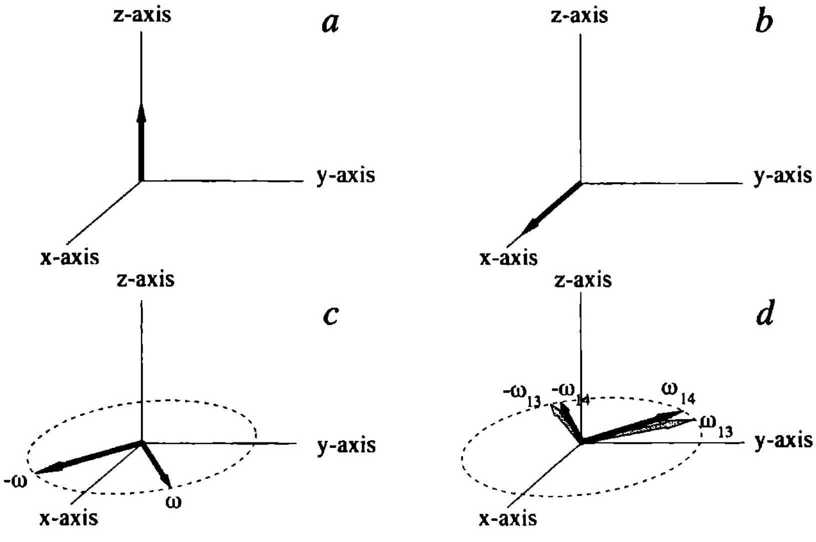

Figure 2.8
a: If the system is in equilibrium, the spins are aligned parallel to the external magnetic field which is taken parallel to the z axis
b: After the first $\frac{1}{2}\pi$ pulse around the y axis, the spins are parallel to the x axis.
c: The spin packages will rotate with a frequency $\pm\omega$ around the z axis.
d: After the π pulse along the y axis, those spin packages which made a permitted transition will rotate with a frequency ω_{14}, those spin packages which made a forbidden transition will rotate with a frequency ω_{13}.

the π_y pulse some spins will rotate in the xy plane with a frequency ν_{14} and other spins will rotate in this plane with a frequency ν_{13}. The magnetisation at the x axis at a time τ after the π_y pulse is now given by:

$$M_x \sim \cos\left(2\pi\tau(\nu_{14} - \nu_{23})\right). \tag{2.6}$$

In other words: the intensity of the echo is modulated with a frequency of $\nu_{14} - \nu_{13}$. This difference is exactly equivalent with the energy difference between the levels 3 and 4: an NMR-frequency. The intensity of these modulations can be as much as 100% of the total echo intensity.

The vector model

Like in the former subsection, again a four level system (S=$\frac{1}{2}$, I=$\frac{1}{2}$) is considered. The Hamiltonian for this system is given by:

$$\mathcal{H} = \beta_e\, \vec{B}_0 \cdot \bar{\bar{\mathrm{g}}} \cdot \vec{S} + \vec{S} \cdot \bar{\bar{\mathrm{A}}} \cdot \vec{I} \; - \; g_n\, \beta_n\, \vec{B}_0 \cdot \vec{I}. \tag{2.7}$$

The hyperfine term induces a magnetic field $\vec{\mathrm{B}}_\mathrm{n}$ at the position of the nucleus, given by:

$$g_n\, \beta_n\, \vec{B}_n \cdot \vec{I} = -\vec{S} \cdot \bar{\bar{\mathrm{A}}} \cdot \vec{I}.$$

Replacing the hyperfine term in equation 2.7 by the expression containing $\vec{\mathrm{B}}_\mathrm{n}$ and using the strong field approximation, equation 2.7 becomes:

$$\mathcal{H} = g\, \beta_e\, B_0\, S_z - g_n\, \beta_n \left(\vec{B}_0 \; + \; \vec{B}_n\right) \cdot \vec{I}. \tag{2.8}$$

Figure 2.9 shows the effective magnetic field $\vec{\mathrm{B}}_\mathrm{eff}$ at the position of the nucleus for two possible orientations of $\vec{B}_n$, namely $\vec{B}_{n-}$ and $\vec{B}_{n+}$. The reversal of the electron spin changes the local field at the nucleus e.g. from $\vec{B}_{eff+}$ to $\vec{B}_{eff-}$. Because the electron spin flip is much faster than the nuclear spin relaxation, the nuclear spin will precess around the effective magnetic field $\vec{\mathrm{B}}_\mathrm{eff-}$. This precession causes an oscillating field at the position of the electron spin which will give rise to the modulation effect in the intensity of the echo signal. If the hyperfine tensor is isotropic, the magnetic field at the nucleus is oriented along the external magnetic field, thus the effective magnetic field $\vec{\mathrm{B}}_\mathrm{eff}$ will also be parallel to $\vec{\mathrm{B}}_0$. As a consequence there will not be any oscillating field at the position of the electron spin, thus the modulation effect will be absent. The same situation occurs when the external magnetic field is oriented parallel to one of the principal axes of the hyperfine tensor.

The quantum mechanical description

Although former descriptions of a two pulse experiment may give some qualitative insight in the mechanisms of ESEEM, a description of the echo intensity can better be derived by using the density operator formalism.

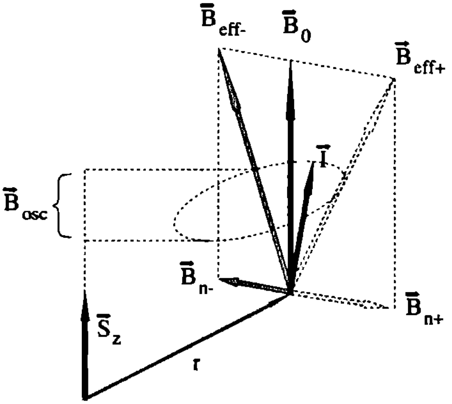

Figure 2.9
The electron spin flip induces a local magnetic field $\vec{B}_{n\pm}$ at the position of the nucleus. Because this electron spin flip is much faster than the nuclear spin relaxation, the nuclear spin $\vec{I}$ will precess around the effective magnetic field $\vec{B}_{eff}$. This precession causes an oscillating field $\vec{B}_{osc}$ at the position of the electron spin which results in the modulation effect.

Intermezzo

The expectation value of an observable O (denoted by $\langle O \rangle$) can be evaluated quantum mechanically as: $\langle O \rangle = \mathrm{Tr}\,(\rho O)$, where ρ is the density operator. An expression for the density operator at a time t is given by $\rho(t) = |\psi(t)\rangle \langle \psi(t)|$, where $|\psi(t)\rangle$ is a state vector for the system at a time t. If one wants to determine the value of $\langle O \rangle$ at a time t, it is necessary to know the expression for $\rho(t)$ i.e. the expression for $|\psi(t)\rangle$. The latter expression can be found by using the Schrödinger equation [9]:

$$\begin{aligned} i\hbar \frac{d\,|\psi(t)\rangle}{dt} &= \mathcal{H}\,|\psi(t)\rangle \\ \Rightarrow |\psi(t)\rangle &= e^{-i\mathcal{H}t/\hbar}\,|\psi(0)\rangle \quad \text{(Assuming a time independent Hamiltonian).} \end{aligned}$$

Therefore, the time dependence of the density operator is given by:

$$\begin{aligned} \rho(t) &= e^{-i\mathcal{H}t/\hbar}\,|\psi(0)\rangle \langle \psi(0)|\, e^{i\mathcal{H}t/\hbar} \\ &\equiv e^{-i\mathcal{H}t/\hbar}\,\rho_0\, e^{i\mathcal{H}t/\hbar}. \end{aligned} \tag{2.9}$$

An expression for the density operator for a system which is in thermal equilibrium (ρ_0) is defined by

$$\rho_0 = \frac{e^{-\mathcal{H}/kT}}{Tr\,(e^{-\mathcal{H}/kT})}. \tag{2.10}$$

A pulse operator can be regarded as a rotation operator working on spins. The general expression for a rotation operator which rotates spins over an angle ϕ around a unit axis $\vec{u}$ is given by [9]:

$$\begin{aligned}
R_u(\phi) &= e^{-i\phi\vec{S}\cdot\vec{u}} \\
&= 1 - i\phi\vec{S}\cdot\vec{u} + \frac{1}{2!}(i\phi)^2\left(\vec{S}\cdot\vec{u}\right)^2 - \frac{1}{3!}(i\phi)^3\left(\vec{S}\cdot\vec{u}\right)^3 + \ldots \\
\text{using } \left(\vec{S}\cdot\vec{u}\right)^2 &= \left(\tfrac{1}{2}u\right)^2 = \left(\tfrac{1}{2}\right)^2 \text{results in :} \\
R_u(\phi) &= 1 - \frac{1}{2!}\left(\tfrac{1}{2}\phi\right)^2 + \cdots - 2i\vec{S}\cdot\vec{u}\left[\tfrac{1}{2}\phi - \frac{1}{3!}\left(\tfrac{1}{2}\phi\right)^3 + \cdots\right] \\
&= \cos\left(\tfrac{1}{2}\phi\right) - 2i\vec{S}\cdot\vec{u}\sin\left(\tfrac{1}{2}\phi\right). \qquad (2.11)
\end{aligned}$$

The spinvector $\vec{S}$ can be rewritten in terms of the Pauli spin matrix vector $\vec{\sigma}$: $\vec{S} = \frac{1}{2}\vec{\sigma}$. Replacing the spinvector by the Pauli spin matrix vector in equation 2.11 can be rewritten as:

$$R_u(\phi) = \cos\left(\tfrac{1}{2}\phi\right) - i\vec{\sigma}\cdot\vec{u}\sin\left(\tfrac{1}{2}\phi\right). \qquad (2.12)$$

Thus the pulse operators can be expressed in terms of Pauli spin matrices using equation 2.12

A single electron

A simple two level system (S=$\frac{1}{2}$, I=0) will be subjected to the two-pulse sequence described on page 17. The echo intensity depends upon the magnetisation which is denoted by M. In a two-pulse experiment the observable at a time t is the magnetisation at a time t, which on its turn is a function of the density operator at a time t. An expression for $\rho(t)$ can be found using equation 2.9. For a two pulse experiment, ρ(t) in the rotating frame is given by:

$$\rho(t) = R_t\, R_\pi\, R_\tau\, R_{\frac{1}{2}\pi}\, \rho_0\, R^{-1}_{\frac{1}{2}\pi}\, R^{-1}_\tau\, R^{-1}_\pi\, R^{-1}_t. \qquad (2.13)$$

where $R_{t\,(\tau)}$ describes the precession of a spin package during a time t (τ), R_π describes a π pulse, $R_{\frac{1}{2}\pi}$ describes a $\frac{1}{2}\pi$ pulse and $\rho(0)$ describes the density operator at time t=0. If the external magnetic field $\vec{B}_0$ is taken parallel to the z axis and the microwave field $\vec{B}_1$ is assumed along the y axis, an expression can be deduced for the two pulse operators using equation 2.12:

$$\begin{aligned}
R_{\frac{1}{2}\pi} &= \frac{1}{\sqrt{2}}(I - i\sigma_y), \\
R_\pi &= -i\sigma_y.
\end{aligned}$$

The operator describing the precession of spin package j around the z axis during a time t with a frequency of ω_j is, according to equation 2.12, expressed by:

$$\begin{aligned}
R_j(t) &= \cos\left(\tfrac{1}{2}\omega_j\, t\right) - i\,\sigma_z \sin\left(\tfrac{1}{2}\omega_j\, t\right) \\
&= \begin{pmatrix} e^{-\frac{1}{2}i\omega_j t} & 0 \\ 0 & e^{\frac{1}{2}i\omega_j t}. \end{pmatrix}.
\end{aligned}$$

According to equation 2.10 the density operator for this spinsystem at time t=0 is given by:

$$
\begin{aligned}
\rho_0 &= \frac{e^{-\mathcal{H}/kT}}{Tr\left(e^{-\mathcal{H}/kT}\right)} \\
&\approx I - \mathcal{H}/kT \\
&= I - \frac{g\beta_e B_0}{kT} S_z \\
&= I - \frac{g\beta_e B_0}{2kT} \sigma_z .
\end{aligned}
$$

In order to derive an expression for the echo intensity at a time t, one needs to find an expression for the magnetisation parallel to the x axis:

$$
\begin{aligned}
\langle M \rangle &= \sum_j Tr\left(\rho M_{x_j}\right) \\
M_{x_j} &= \tfrac{1}{2} g\beta_e \sigma_{x_j} .
\end{aligned}
\tag{2.14}
$$

Where M_{x_j} is the magnetisation along the x axis due to spin package j. After inserting the corresponding matrices for the operators in equations 2.13 and 2.14 one finds for the magnetisation:

$$
\langle M \rangle \sim \sum_j -\cos\left(\omega_j \tau - \omega_j t\right). \tag{2.15}
$$

Equation 2.15 shows that an echo arises at a time t = τ as was expected.

A nucleus with a single electron

For the more complicated of S = $\frac{1}{2}$, I = $\frac{1}{2}$, the echo intensity can also be derived by using equations 2.13 and 2.14. The only difference is that one needs 4 × 4 matrices to describe this four level system. Hence, ρ_0, $R_{\frac{1}{2}\pi}$, R_π, R_t and M_x are represented by:

$$\rho_0 = \frac{g\beta_e B_0}{2kT}\begin{pmatrix} 1 & 0 & & \\ 0 & 1 & & \\ & & -1 & 0 \\ & & 0 & -1 \end{pmatrix}$$

$$R_{\frac{1}{2}\pi} = \frac{1}{\sqrt{2}}\begin{pmatrix} 1 & 0 & f & p \\ 0 & 1 & -p^\dagger & f^\dagger \\ -f^\dagger & p & 1 & 0 \\ -p^\dagger & -f & 0 & 1 \end{pmatrix}$$

$$R_\pi = \begin{pmatrix} & & f & p \\ & & -p^\dagger & f^\dagger \\ -f^\dagger & p & & \\ -p^\dagger & -f & & \end{pmatrix}$$

$$R_t = \begin{pmatrix} e^{-\frac{1}{2}it(\omega_{12}+\omega_j)} & 0 & & \\ 0 & e^{\frac{1}{2}it(\omega_{12}-\omega_j)} & & \\ & & e^{-\frac{1}{2}it(\omega_{34}-\omega_j)} & 0 \\ & & 0 & e^{\frac{1}{2}it(\omega_{34}+\omega_j)} \end{pmatrix}$$

$$M_x = g\beta_e\begin{pmatrix} & & f & p \\ & & -p^\dagger & f^\dagger \\ -f^\dagger & p & & \\ -p^\dagger & -f & & \end{pmatrix}.$$

In these equations f denotes a forbidden transition and p denotes a permitted transition (see also figure 2.7). In order to find an expression for the echo intensity again one needs to calculate the magnetisation at a time τ according to equation 2.14. The value for the density matrix at a time τ is presented by:

$$\rho(\tau) \;=\; R_\tau\, R_\pi\, R_\tau\, R_{\frac{1}{2}\pi}\, \rho_0\, R^{-1}_{\frac{1}{2}\pi}\, R^{-1}_\tau\, R^{-1}_\pi\, R^{-1}_\tau \tag{2.16}$$

for a two pulse sequence ($\frac{1}{2}\pi - \tau - \pi - \tau -$ echo)

and :

$$\rho(\tau) \;=\; R_\tau\, R_{\frac{1}{2}\pi}\, R_T\, R_{\frac{1}{2}\pi}\, R_\tau\, R_{\frac{1}{2}\pi}\, \rho_0\, R^{-1}_{\frac{1}{2}\pi}\, R^{-1}_\tau\, R^{-1}_{\frac{1}{2}\pi}\, R^{-1}_T\, R^{-1}_{\frac{1}{2}\pi}\, R^{-1}_\tau \tag{2.17}$$

for a three pulse sequence ($\frac{1}{2}\pi - \tau - \frac{1}{2}\pi - T - \frac{1}{2}\pi - \tau -$ echo).

Inserting the expressions for the matrices into the equation 2.16 and 2.17 one can derive an expression for ρ at time $t = \tau$, inserting that expression into equation 2.14 one finds for the echo intensity E:

two pulse :

$$E(t=\tau) = |f|^4 + |p|^4 + |f|^2|p|^2\left[2\cos(\omega_{12}\tau) + 2\cos(\omega_{34}\tau) - \cos((\omega_{12}+\omega_{34})\tau) - \cos((\omega_{12}-\omega_{34})\tau)\right]. \quad (2.18)$$

three pulse :

$$E(t=\tau) = |f|^4 + |p|^4 + 2|f|^2|p|^2 \left[1 + \sin^2\left(\tfrac{1}{2}\omega_{12}\tau\right)\left(\cos\left(\omega_{34}[\tau+T]\right) - 1\right) + \sin^2\left(\tfrac{1}{2}\omega_{34}\tau\right)\left(\cos\left(\omega_{12}[\tau+T]\right) - 1\right)\right]. \quad (2.19)$$

Conclusions

Regarding the former pages a few concluding remarks can be made about an ESEEM experiment:

- As has been shown on page 19 the hyperfine tensor should be anisotropic in order to observe modulation on the echo.
- If the external magnetic field is oriented parallel to one of the principal axis of the hyperfine tensor, the ESEEM signal will be absent (see page 19).
- The equation for the echo intensity for a two pulse sequence (equation 2.18) contains besides the normal NMR frequencies (ω_{12} and ω_{34}) also the sum and difference of these frequencies. Therefore, frequency peaks are visible in an ESEEM spectrum which has been recorded using a two pulse sequence at the frequencies ω_{12}, ω_{34}, $\omega_{12}+\omega_{34}$ and $\omega_{12}-\omega_{34}$.
- In an ESEEM spectrum which has been recorded using a three pulse sequence, an NMR frequency can be suppressed as can be deduced from equation 2.19. For instance if T is chosen so that $\cos(\omega_{12}[\tau+T]) = 1$, the frequency ω_{34} is suppressed. In the ESEEM experiments described in chapter 8 this effect can result in the disappearance of the line intensity of one transition, while the signal intensity of another transition remains unchanged.

HYSCORE

An experiment which is very helpful for data analyses is a so called HYSCORE (Hyperfine Sublevel Correlation Spectroscopy) experiment [10]. A HYSCORE experiment consists of a four pulse sequence $\frac{1}{2}\pi - \tau - \frac{1}{2}\pi - T1 - \pi - T2 - \frac{1}{2}\pi - \tau -$ echo. Compared to the three pulse sequence described above, a HYSCORE sequence contains one additional π pulse between the second and the third $\frac{1}{2}\pi$ pulse. This additional pulse causes the correlation of the NMR frequencies from different m_s states of the same electron. This can be verified by calculating the echo intensity at a time t = τ using equation 2.14. The density operator at a time t = τ is given by:

$$\rho(\tau) = R_\tau\, R_{\frac{1}{2}\pi}\, R_{T2}\, R_\pi\, R_{T1}\, R_{\frac{1}{2}\pi}\, R_\tau\, R_{\frac{1}{2}\pi}\, \rho_0\, R^{-1}_{\frac{1}{2}\pi}\, R^{-1}_\tau\, R^{-1}_{\frac{1}{2}\pi}\, R^{-1}_{T1}\, R^{-1}_\pi\, R^{-1}_{T2}\, R^{-1}_{\frac{1}{2}\pi}\, R^{-1}_\tau.$$

During a HYSCORE experiment the times T1 and T2 are independently increased which results in a two dimensional spectrum. After Fourier transformation of this spectrum cross peaks will be visible at the frequency coordinates (ω_{12},ω_{34}) and (ω_{34},ω_{12}). These cross peaks indicate that the frequencies ω_{12} and ω_{34} originate from the same atom. Consequently, the interpretation of ESEEM spectra containing signals from multiple atoms is simplified by performing HYSCORE experiments.

2.5 About tensors and matrices

Neither the g matrix nor the hyperfine matrix may be called tensors, because they do not transform as a tensor. A tensor $\overline{\overline{\mathrm{T}}}$ transforms as:

$$\overline{\overline{T}}\,' = R^{-1} \cdot \overline{\overline{T}} \cdot R.$$

In this equation R denotes a transformation matrix, for instance a rotation matrix. It can be shown that the g matrix does not transform as a tensor by considering the electron Zeeman term in the Hamiltonian [11]:

$$\begin{aligned}
\mathcal{H} &= \beta_e\, \vec{B}_0 \cdot \overline{\overline{g}} \cdot \vec{S} \\
&= \beta_e\, \vec{B}_0\, R_l\, R_l^{-1} \cdot \overline{\overline{g}} \cdot R_s\, R_s^{-1}\, \vec{S} \\
&\equiv \beta_e\, \vec{B}\,'_0 \cdot \overline{\overline{g}}\,' \cdot \vec{S}\,'
\end{aligned}$$

where : R_l denotes a transformation with respect to the laboratory axis system

R_s denotes a transformation with respect to the spin axis system

$\vec{B}\,'_0 = \vec{B}_0\, R_l$

$\vec{S}\,' = R_s^{-1}\, \vec{S}$

$\overline{\overline{g}}\,' = R_l^{-1} \cdot \overline{\overline{g}} \cdot R_s.$

This means that the g matrix only transforms as a tensor if R_l equals R_s. The argument reported above, also holds for the hyperfine matrix. Only the quadrupole tensor transforms as a real tensor. Despite of this argument g is still referred to as a tensor in literature and also in this thesis. A justification can be that in an EPR experiment only energy differences are measurable which is directly related to the g^2 tensor, which transforms as a real tensor as can be shown easily:

$$\begin{aligned}
\overline{\overline{g}}\,'^2 = \left(R_l^{-1} \cdot \overline{\overline{g}} \cdot R_s\right)^2 &= R_l^{-1} \cdot \overline{\overline{g}} \cdot R_s\, R_s^{-1} \cdot \overline{\overline{g}}^{\,T} \cdot R_l \\
&= R_l^{-1} \cdot \overline{\overline{g}}\,\overline{\overline{g}}^{\,T} \cdot R_l \\
&= R_l^{-1} \cdot \overline{\overline{g}}^{\,2} \cdot R_l.
\end{aligned}$$

The fact that the g^2 tensor is directly accessible from the measurements can best be illustrated by taking a two level spin system S=$\frac{1}{2}$ described by the Hamiltonian $\mathcal{H} = \beta_e \vec{\mathrm{B}}_0 \cdot \bar{\bar{\mathrm{g}}} \cdot \vec{\mathrm{S}}$. This Hamiltonian can be rewritten as a matrix:

$$\frac{1}{2}\beta_e \begin{pmatrix} \sum\limits_{j=x}^{z} B_{0j}\, g_{jz} & \sum\limits_{j=x}^{z} B_{0j}\, (g_{jx} - i g_{jy}) \\ \sum\limits_{j=x}^{z} B_{0j}\, (g_{jx} + i g_{jy}) & -\sum\limits_{j=x}^{z} B_{0j}\, g_{jz} \end{pmatrix}.$$

The energy difference ΔE can be found by diagonalising this matrix and subtracting the eigenvalues:

$$\begin{aligned} \Delta E &= \beta_e \left[\left(\sum_{j=x}^{z} B_{0j} g_{jx} \right)^2 + \left(\sum_{j=x}^{z} B_{0j} g_{jy} \right)^2 + \left(\sum_{j=x}^{z} B_{0j} g_{jz} \right)^2 \right]^{\frac{1}{2}} \\ &= \beta_e \left[\sum_{i,j=x}^{z} B_{0j} g_{jx} g_{ix} B_{0i} + \sum_{i,j=x}^{z} B_{0j} g_{jy} g_{iy} B_{0i} + \sum_{i,j=x}^{z} B_{0j} g_{jz} g_{iz} B_{0i} \right]^{\frac{1}{2}} \\ &= \beta_e \left[\vec{B}_0 \cdot \bar{\bar{g}}^{\,2} \cdot \vec{B}_0 \right]^{\frac{1}{2}}. \end{aligned}$$

Consequently an EPR experiment reveals the g^2 tensor rather than the g matrix. The principle values of the g 'tensor' reported in this thesis are obtained by taking the square root of the principle values of the g^2 tensor. With more effort but using a similar example it can be shown that an EPR experiment reveals the A^2 tensor rather than the hyperfine matrix. Again, the principle values of the hyperfine 'tensor' reported in this thesis are obtained by taking the square root of the principle values of the A^2 tensor.

references

[1] Dorio, M.M., and Freed, J.H., 1979, *Multiple Electron Resonance Spectroscopy* (Plenum Press, New York)

[2] Kurreck, H., Kirste, B., and Lubitz, W, 1988, *Electron Nuclear Double Resonance Spectroscopy of Radicals in Solution* (VCH Publishers, Inc.)

[3] Freeman, A.J., and Frankel, R.B., 1967, *Hyperfine Interactions* (Academic Press, New York)

[4] Kevan, L., and Kispert, L.D., 1976, *Electron Spin Double Resonance Spectroscopy* (John Wiley & Sons, New-York)

[5] Slichter, C.P., 1992, *Principles of Magnetic Resonance* (Springer-Verlag, New- York)

[6] Biehl, R., Plato, M. and Möbius, K., 1975, *J. Chem. Phys.*, **63**, 3515

[7] Reijerse, E.J., 1986, *Electron Spin Echo Spectroscopy on Transition Metal Complexes* (Sneldruk, Enschede)

[8] Shane, J.J., 1993, *Electron Spin Echo Envelope Modulation Spectroscopy of Disordered Solids* (FEBOdruk, Enschede)

[9] Cohen-Tannoudji, C., Diu, B. and Laloë, F., 1977, *Quantum Mechanics Volumes 1 and 2*, (John Wiley & Sons, New York)

[10] Höfer, P., Grupp, A., Nebenfür, H. and Mehring, M. 1986, *J. Chem. Phys.*, **132**, 279

[11] Callens, F.J., 1991, *Elektronen Paramagnetische Resonantie van Enkele Atomaire en Moleculaire Defecten in Alkalihalogeniden, Synthetische en Biologische Carbonaat-bevattende Apatieten*

Chapter 3

Experimental Considerations

The experimental results described in this thesis are obtained by making use of three different resonance techniques: EPR (Electron Paramagnetic Resonance), ESEEM (Electron Spin Echo Envelope Modulation) and ENDOR (Electron Nuclear Double Resonance). The experimental configuration necessary to perform EPR measurements is considered to be well known, thus a description about the EPR set-up will be omitted. The experimental set-up concerning the ESEEM measurements is extensively described elsewhere [1] therefore it is only mentioned briefly in this chapter (section 3.2). The ENDOR set-up will be considered in more detail, because descriptions of ENDOR resonators especially suitable for single crystal experiments are not too common. Therefore, chapter 4 is dedicated to a description of an ENDOR resonator suitable for single crystal measurements. Section 3.4 reports about the details of a computer program which controls the ENDOR measurements. Because this thesis describes the results of single crystal measurements, section 3.1 will focus upon one of the major aspects involved in single crystal experiments: the rotation of the crystal.

3.1 Single crystals

In a single crystal all atoms are organised according to rules imposed by the crystal symmetry class of that crystal. As a result the g, hyperfine and the quadrupole tensors can be completely determined by recording the angular dependence of the EPR, ENDOR and/or ESEEM signals in three mutually perpendicular planes. This means that these spectra have to be recorded for different orientations of the crystal with respect to the external magnetic field. This implies a severe demand upon the experimental set-up: it has to be possible to rotate the crystal or the external magnet around two independent not coinciding axes. The magnet is a so called rotational base magnet which means that the external magnetic field can be rotated around a vertical axis (the z axis in the figures 3.1a to 3.1c). The range of this rotation extends at least from -80° to +80°. Because it is technically infeasible to rotate the magnet around a horizontal axis as well, the crystal has to have the possibility to rotate around a horizontal axis. For this reason the crystal is mounted on a rod which is oriented perpendicular to the axis of rotation of the magnet: the x axis in figures 3.1. The rod can be rotated around this x axis by means of a worm wheel construction. By rotating the magnet and the rod, spectra can be recorded for

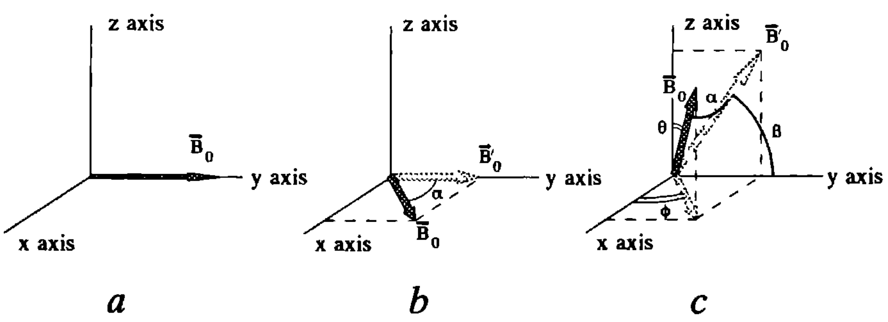

Figure 3.1
The orientation of the external magnetic field $\vec{B}_0$ in the crystal axes system, xyz.
a: Neither the external magnetic field, nor the crystal has been rotated; The external magnetic field vector $\vec{B}_0$ is parallel to the y axis.
b: The external magnetic field has been rotated around the z axis by an angle α, α is defined as the angle between $\vec{B}_0$ and $\vec{B}'_0$. The vector $\vec{B}'_0$ is the projection of $\vec{B}_0$ on the yz plane.
c. The crystal has been rotated by an angle β around the x axis and the external magnetic field has been rotated around the z axis by an angle α. Note that α is the angle between $\vec{B}_0$ and $\vec{B}'_0$, while the spherical angle ϕ denotes the angle between the projection of $\vec{B}_0$ on the xy plane and the x axis. The spherical angle θ is defined as the angle between the z axis and $\vec{B}_0$, while β is the angle between the y axis and $\vec{B}'_0$.

(almost) every desired orientation of the crystal with respect to the external magnetic field. If the magnet is rotated over an angle α and the rod is rotated over an angle β, the angles α and β do not coincide with the spherical angles ϕ and θ as is clearly demonstrated by figure 3.1c. $\vec{B}'_0$ is the projection of the magnetic field vector $\vec{B}_0$ on the yz plane, α is the angle between $\vec{B}_0$ and $\vec{B}'_0$, and β is the angle between $\vec{B}'_0$ and the y axis. Therefore, the coordinates of $\vec{B}_0$ in the crystal frame xyz, are given by: ($\sin\alpha$, $\cos\alpha\cos\beta$, $\cos\alpha\sin\beta$). Using figure 3.1 it is possible to deduce a relation between the spherical angles ϕ and θ, and the angles α and β:

$$\begin{aligned} \sin\alpha &= \sin\theta\,\cos\phi \\ \sin\beta &= \frac{\cos\theta}{\sqrt{\sin^2\theta\,\sin^2\phi + \cos^2\theta}}. \end{aligned}$$

The majority of the resonance spectra described in this thesis are recorded in the planes spanned by the three g tensor axes: the (g_1,g_2) , (g_1,g_3) and (g_2,g_3) plane. The measurement strategy is to find an orientation for $\vec{B}_0$ so that $\vec{B}_0$ is parallel to a principal g tensor axis. If this orientation is found spectra can be recorded in a plane perpendicular to this axis. An example: the g_1 axis is found for an orientation of $\vec{B}_0$ defined by the angles α (indicating the angle of the rotational base magnet) and β (indicating the angle of the rod), the (g_2,g_3) plane is specified by the angles α' and β' where

$$\beta' = \beta - \arccos\left(-\tan\alpha * \tan\alpha'\right). \tag{3.1}$$

The values of α and β are known so for every value of α' the corresponding value of β' can be calculated using equation 3.1. Another measurement strategy would be to find two different orientations for $\vec{B}_0$ ($\vec{B}_{01}$ and $\vec{B}_{02}$) and subsequently to record the spectra in a plane spanned by these two vectors. In this case $\vec{B}_{01}$ is defined by the angles α_1 and β_1 while $\vec{B}_{02}$ is defined by the angles α_2 and β_2. The vector $\vec{B}_\perp$ which is perpendicular to both $\vec{B}_{01}$ and $\vec{B}_{02}$, is specified by the angles α and β:

$$\begin{aligned}\tan\alpha &= -\frac{\cos(\beta_1-\beta)}{\tan\alpha_1}\\ \tan\beta &= -\frac{\tan\alpha_1\cos\beta_2-\tan\alpha_2\cos\beta_1}{\tan\alpha_1\sin\beta_2-\tan\alpha_2\sin\beta_1}.\end{aligned}$$

The plane spanned by $\vec{B}_{01}$ and $\vec{B}_{02}$ which is specified by the angles α' and β' is, evidently, perpendicular to $\vec{B}_\perp$. Therefore, the angle β' can be calculated using equation 3.1.

3.2 ESEEM

Figure 3.2 shows the experimental set-up used to perform ESEEM measurements.

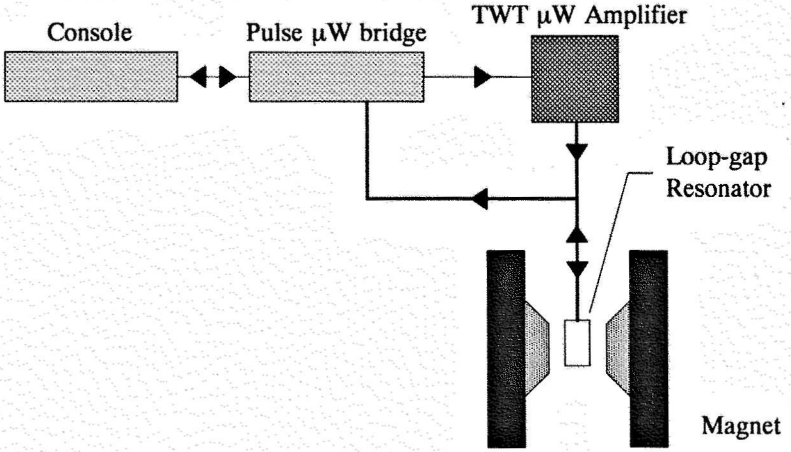

Figure 3.2
A schematic presentation of the experimental ESEEM set-up

The console is a Bruker 380 FT-EPR pulse spectrometer, the pulse microwave bridge (Bruker ESP 380 -1010) contains, among others, the klystron and the detector i.e. this bridge generates the pulses and detects the ESEEM signal. The TWT amplifier (M square microtek inc M303) amplifies the microwave pulses. The resonator used is a home built three-loop/two-gap resonator shown in figure 3.3. Notice the hole in the side wall of the

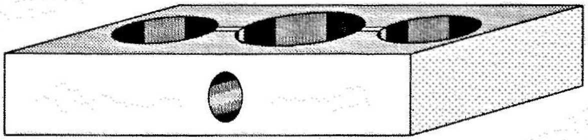

Figure 3.3
A loop-gap resonator suitable to perform single crystal ESEEM measurements.

resonator which is used to insert the rod on which the crystal is mounted. This resonator has its equivalence in a resonant scheme consisting of two capacitors (the gaps) with a capacity C and three coils (the loops) with an inductance L. To a good approximation the resonance frequency ν_{res} can be calculated accordingly to $\nu_{res} = \frac{1}{2\pi\sqrt{LC}}$.

3.3 Fourier Transformation

All the information yielded by an ESEEM spectrum is stored in a time domain spectrum. The interpretation of such a spectrum is rather complicated if not impossible. Therefore, the spectrum is transformed into a frequency domain spectrum by means of a Fourier transformation. This transformation process can generally be separated in a number of separate steps which all can effect the resulting spectrum:

a Baseline correction

b Apodisation

c Zero filling

d Fast Fourier transformation (FFT)

e Magnitude calculation

These steps are visualised in the figures 3.4a to 3.4f. In order to avoid misinterpretations due to artifacts which can arise by application of the former mentioned steps, a brief description will be given about their effect(s) on the resulting spectrum.

Baseline Correction

The decay of the echo intensity is generally described by an exponential function. On this decay the modulations are present, hence, to reveal these modulation the decay has to be removed. The procedure of removing the exponential decay is called 'baseline correction'. If the decay of the echo intensity is only minute, it is tempting to omit the baseline correction. However, it is likely that, as a result of this omittance, artificial frequency peaks will arise at low frequencies in the spectrum as is shown in the figures 3.5a and b. In figure 3.5a the baseline has been fitted by a sixth order polynomial, which is a much better fit than the linear function which is used in figure 3.5b.

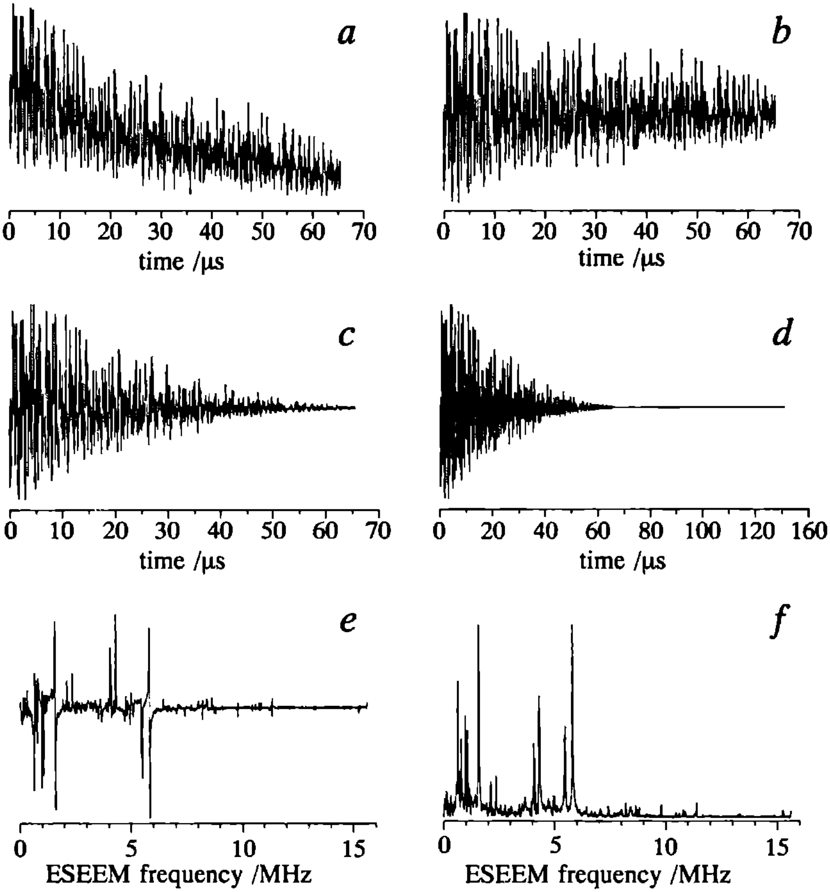

Figure 3.4
Six steps which transform a time domain spectrum into a frequency domain spectrum.
a: A measured time domain spectrum.
b: The resulting spectrum after a baseline correction has been applied on the spectrum displayed in figure 'a': the exponential decay has been removed.
c: The resulting spectrum after apodising the spectrum showed in figure 'b'.
d: The resulting spectrum after the spectrum presented in figure 'c' has been zero filled. Note that the spectrum extends over a longer period.
e: The resulting spectrum after Fourier transforming the spectrum showed in figure 'd'. Only the real part of the spectrum is been displayed.
f: The final ESEEM spectrum.

Apodisation

A Fourier transformation applicable for transforming a time domain spectrum is given by:

$$I(\nu) = \int_0^\infty I(t)e^{-it\nu}dt \tag{3.2}$$

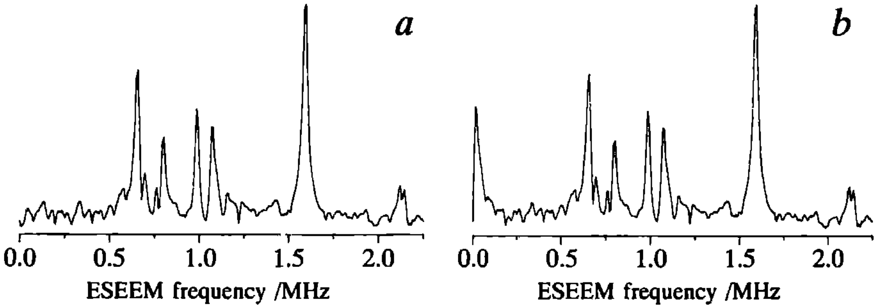

Figure 3.5
Effect of the 'baseline correction' on the spectrum.
a: The decay of the echo intensity has been fitted by means of a sixth order polynomial function. The 'baseline' described by this function has successively been subtracted from the time domain spectrum. The resulting ESEEM spectrum is shown.
b. The decay of the echo intensity has been fitted by means of a linear function. This function has successively been subtracted from the time domain spectrum. The resulting ESEEM spectrum is shown. Clearly visible is an additional artificial peak at low frequency.

with $I(t)$ describing the signal in the time domain spectrum
$I(\nu)$ describing the signal in the frequency domain spectrum.

Equation 3.2 shows that one should take an infinite integral from the time domain spectrum. In practise however, a time domain spectrum consists of only a finite number of measured points. The integral in equation 3.2 should therefore be replaced by a summation, which results in:

$$I(k\Delta\nu) = \sum_{n=0}^{N} I(n\Delta t)e^{-ink/N} \quad k,n \in \mathbb{N} \tag{3.3}$$

with : $\Delta\nu$ the frequency difference between two adjacent points in the frequency domain spectrum.
Δt the time difference between two adjacent points in the time domain spectrum.
N the number of measured points in the domain spectrum.

Fourier transformation of this finite spectrum will result in the occurrence of small artificial signals on both sides of an actual frequency peak. In order to remove these factitious signals one can 'apodise' the spectrum by multiplying the spectrum by a so called window function. A window function is a function which has a maximum of one and is approaching zero. Figure 3.6 shows a few examples of different window functions. Unfortunately, apodisation has the disadvantage that the frequency peaks are broadened: the smoother the window function approaches zero, the less intense the artificial signals will be, but

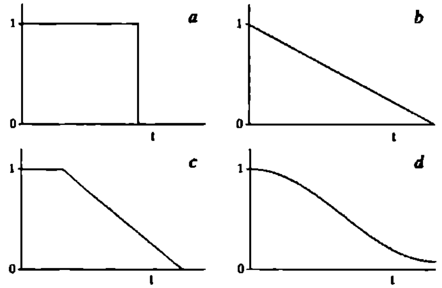

Figure 3.6
A few examples of commonly used window functions:
a: A 'Boxcar' window.
b: A 'Triangle' window.
c: A 'Trapezium' window.
d: A 'Hamming' window.

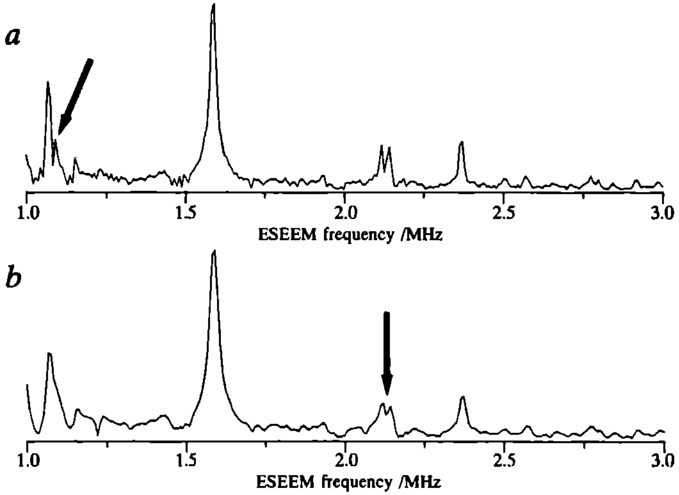

Figure 3.7
Effect of the apodisation on the time domain spectrum.
a: The time domain spectrum preceding this ESEEM spectrum has not been apodised. This results in narrow ESEEM lines which show additional side peaks as is indicated by the arrow.
b: The time domain spectrum preceding this ESEEM spectrum has been apodised using a Hamming window. This results in broader ESEEM lines, but this time without additional side peaks. The broadening of the lines can cause overlap between two closely spaced lines as indicated by the arrow.

also the broader the peaks will become, as is shown by figure 3.7. Broadening of peaks can cause overlap between two closely spaced peaks. If the modulations decay to zero, apodisation of the spectrum is unnecessary and can better be omitted in order to avoid artifacts.

Zero Filling

Zero filling means that the span of the time domain spectrum is enlarged by placing zeroes following the original spectrum. According to equation 3.3 the spacing between two

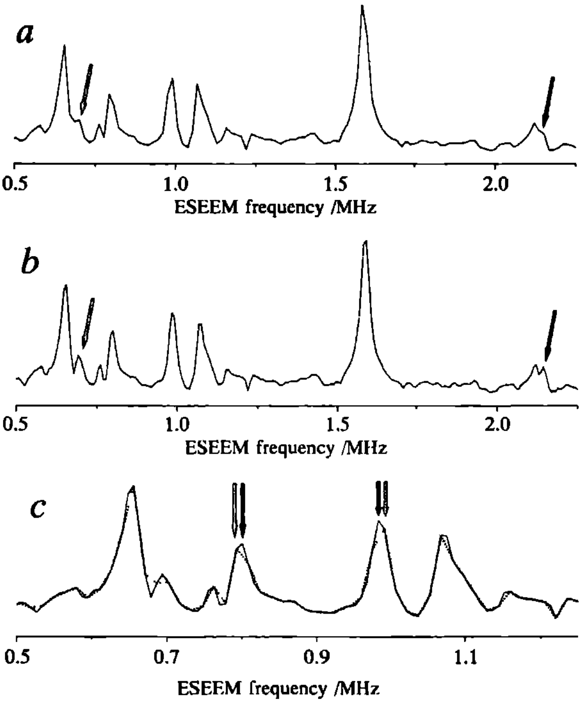

Figure 3.8
Effect of zero filling the time domain spectrum
a: The time domain spectrum preceding this ESEEM spectrum has not been zero filled. This results in an ESEEM spectrum with a low resolution
b. The time domain spectrum preceding this ESEEM spectrum has been zero filled, which results in an ESEEM spectrum having a higher resolution. The arrows indicate the positions on which the increase of resolution is clearly visible.
c: Dotted line: The time domain spectrum preceding this ESEEM spectrum has not been zero filled. Solid line: The time domain spectrum preceding this ESEEM spectrum has been zero filled. Note that some ESEEM peaks seem to be located on slightly different positions.

adjacent points in the frequency domain spectrum $\Delta\nu$ is related to the spacing between two adjacent points in the time domain spectrum Δt by: $\Delta\nu = \frac{1}{N\Delta t}$. Thus, adding zeroes to the time domain spectrum increases the total number of points N and therefore decreases $\Delta\nu$ i.e. increases the resolution of the frequency domain spectrum. Figures 3.8a and b show the differences between spectra resulting from a spectrum which has not been zero filled (figure a) and which has been zero filled (figure b). Increasing the resolution by zero filling does not mean that the corresponding frequency domain spectrum contains more information than the frequency spectrum obtained without zero filling. However, the positions of the frequency peaks which are revealed by the time domain spectrum, are described more accurately if the spectrum is zero filled as is shown in figure 3.8c.

Magnitude

The time domain spectrum produced by a stimulated echo ESEEM experiment only contains positive cosine terms [2]. Therefore, the real part of the frequency domain is a sufficient representation of the ESEEM spectrum. Obviously, the cosine part can only be

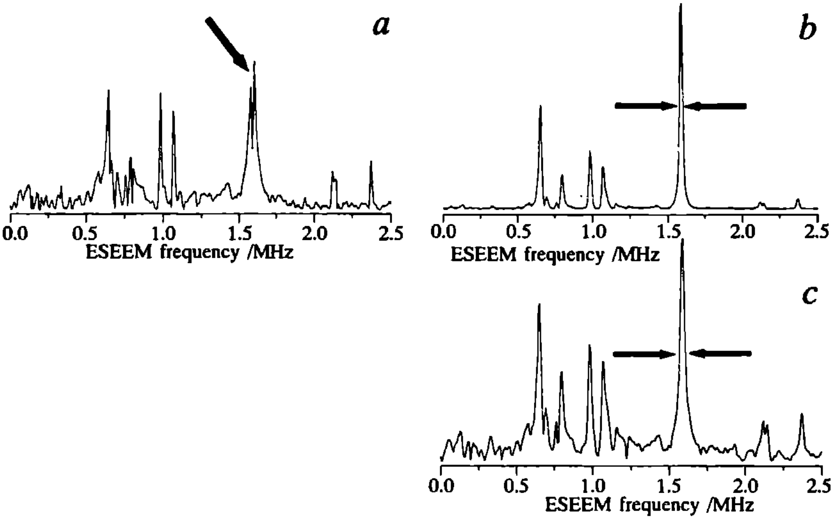

Figure 3.9

a: The absolute value has been taken of the real part of the Fourier transformed spectrum. Note that a line (indicated by the arrow) seems to be split, because information about the phase of the peak is neglected.

b: The 'power' value of the Fourier transformed spectrum has been taken, the information about the phase of a line has been included but the lines seem to be narrower as they actually are.

c: The 'magnitude' value of the Fourier transformed spectrum has been taken, the information about the phase of a line has been included and the lines have their actual width.

obtained after a proper phase correction which compensates for the experimental dead-time. This is not a trivial procedure and therefore the 'amplitude mode' is used for the spectral analysis in this thesis. Figures 3.9a to 3.9c explain the term 'amplitude mode':

fig a Take the absolute value of the real part of the spectrum. All phase information will be lost which can result in an artificial linesplitting. This option can only be used if a phase correction is applied and if the cosine terms describing the time domain spectrum are not damped. Because this is generally not the case in a measured ESEEM spectrum, the option shown in figure 3.9a is not applied.

fig b Add the squares of the real and the imaginary part of the Fourier transformed spectrum, yielding a power spectrum. In a power spectrum the phase information is included in the lineshape and the signal to noise ratio is better than in the spectrum of 'a', but the linewidths are artificially smaller. This option is, like the previous option, generally not used.

fig c Take the square root of the power spectrum. The phase information is again included in the lineshape, while the lines have their 'natural' width. The 'amplitude mode' ESEEM spectra shown in this thesis are obtained using this option.

Line intensity

Because the ESEEM spectrum is digitally stored it consists of a finite set of data points. This means that an ESEEM signal in the frequency domain spectrum is described by a small number of points. This number of points depends upon the width of the ESEEM line, the resolution of the total spectrum and the total frequency width of the ESEEM spectrum. Artifacts arise if the frequency difference between two adjacent points is of the order of the linewidth, so that an ESEEM peak is only described by a few data points.

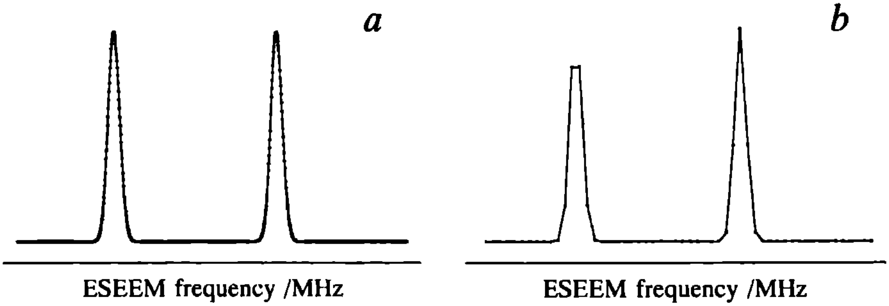

Figure 3.10
a: The frequency difference between to adjacent data points is much smaller than the linewidth of an ESEEM line.
b: The frequency difference between to adjacent data points is almost equal to the linewidth of an ESEEM line, the lines appear to have different intensities.

The result in this case may be that lines which actually have equal intensity, appear to have different intensities as is shown in the figures 3.10a and b.

3.4 ENDOR

Figure 3.11 shows the block diagram of the experimental CW ENDOR set-up (see also [3-4]. Besides the usual EPR set-up (containing an EPR console, an EPR X-band bridge and a magnet) it consists of a radio frequency (RF) sweeper, a lock-in amplifier, an ENDOR cavity, a RF amplifier and a PC-486 computer. A description of the ENDOR resonator will be given in chapter 4.

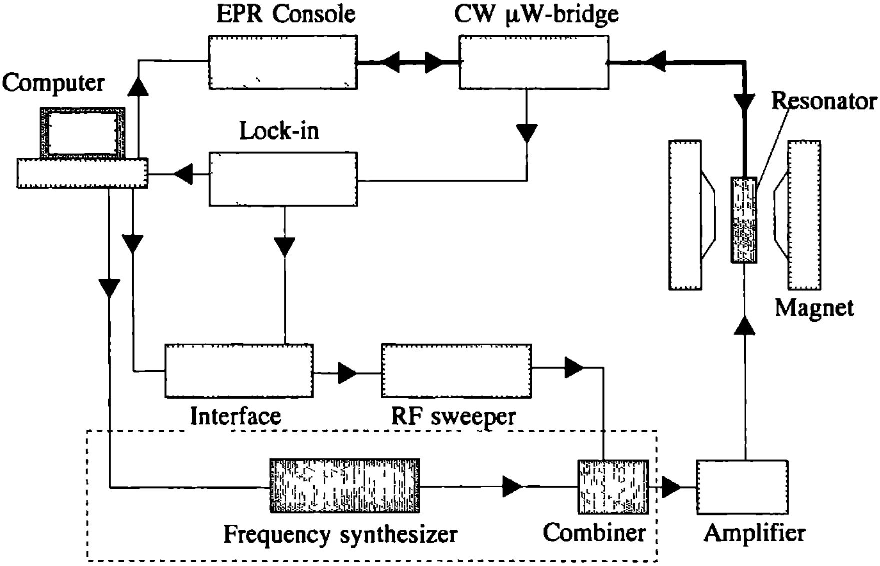

Figure 3.11
The experimental ENDOR set-up The part in the dashed box is used exclusively for general triple resonance experiments

The lock-in amplifier (PAR model 124A) has a double function:

a it reads the (modulated) ENDOR signal from the EPR bridge.

b it generates the modulation frequency for the RF frequency.

The RF sweeper can be controlled externally by a voltage: the more negative the voltage, the higher the RF frequency. A DC voltage is generated by converting a binary code using a 16 bit DAC (digital to analog converter), in the interface box. The binary code, on its turn, is generated by the computer. In order to be able to employ a phase sensitive detection, the RF frequency needs to be modulated with a low frequency modulation amplitude. For this purpose an AC voltage is generated by the lock-in amplifier. The AC and DC voltages are added in the interface and the resulting voltage is send to the RF sweeper. Consequently, a frequency sweep can be performed by sending a modulated voltage ramp to the RF sweeper, generating a modulated RF frequency. This voltage ramp is generated by sending an array containing different binary codes to the DAC. The actual frequency can be read by the computer by means of an IEEE port on the frequency counter. Data transfer through an IEEE port is subjected to a so called 'handshaking' protocol. Due to this protocol the data can be transferred at a maximum rate of 13 transfers per second. This rate restricts the lower limit of the scan time of one ENDOR sweep. A much more rapid scan can be performed if the frequency is not read: a typical spectrum consisting of 1024 points can then be recorded in as less as 11 seconds. The practical use of such a fast scan, however, is questionable.

The frequency synthesizer used to perform general triple resonance experiments can be controlled directly by a computer. During a general triple experiment, the synthesizer produces the fixed RF frequency (see section 2.3), while the sweeper generates the swept frequency. Both frequencies are combined and send to the amplifier. Only the swept frequency is modulated.

The computer program

The main advantage of a computer controlled ENDOR set-up is that a spectra can be accumulated thus increasing the signal to noise ratio. In this way even signals buried in the noise can be recorded. A second advantage is the ease of data storage and data manipulation.

The programming environment Labview® is used for implementing the ENDOR acquisition program. This programming environment runs under windows on a MS-DOS computer and offers several preprogrammed communication protocols between the computer and externally connected devices. In contrast to most well known programming languages as C, or Pascal, Labview is a graphical programming environment. One of the main advantages of Labview is that a programmer does not have to worry about the command syntax. The mathematical functions, subroutines etc in a Labview program are represented by triangles or squares. Data flow is accomplished by drawing lines from one symbol to another. As a result a Labview program looks like an electronic print: with chips, resistors etc which are connected by wires. Basic demands when writing the program were that the resulting program would be flexible, easy to use even without reading a manual, and that it would protect the experimental set-up against mistakes of an experimentator which can be harmful for the equipment. The ENDOR data program consists of three parts: a part for the acquisition of a spectrum, a part for the phase adjustment of the signals and a part to read a previously stored spectrum from disk. All parts of this program have been programmed in a modular way which facilitates the adjustment or expansion of the program.

Data acquisition

Figures 3.12a and 3.12b show examples of a few parts of a Labview program. The square marked 'Port Write' in figure 3.12a is a preprogrammed communication protocol for communication via a digital input/output board. The square in figure 3.12b labelled 'AI one PT' is another example of a preprogrammed communication protocol. This square 'reads' the actual ENDOR data signal. The heart of the ENDOR acquisition program consists of the repeated execution of the sequence:

- Set an ENDOR frequency (figure 3.12a).
- Wait a time (optional).
- Read the actual frequency value as indicated by the frequency counter (optional).

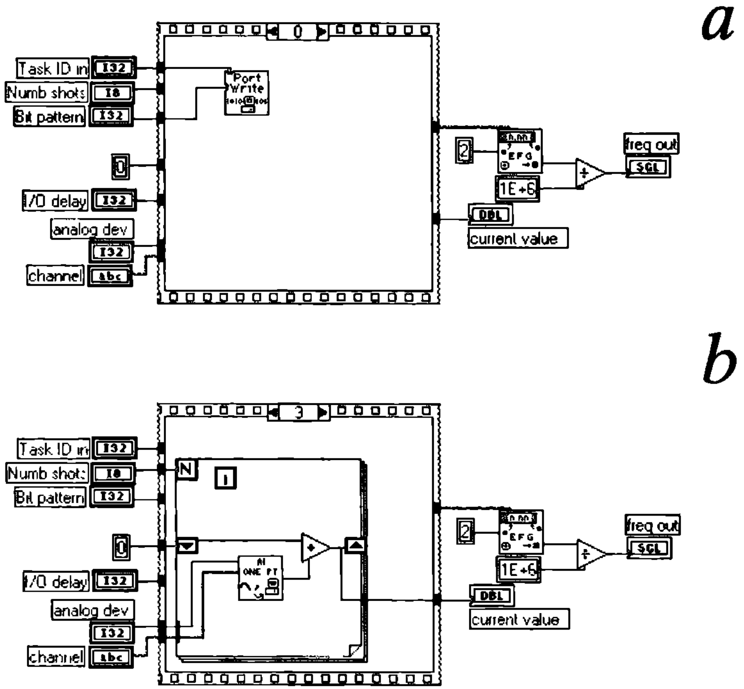

Figure 3.12
a The part of the program which sets the ENDOR frequency
b The part which reads the ENDOR data signal. This signal can be read multiple times, adding each new value to the previously acquired signal. The rectangular labelled 'current value' is the recorded ENDOR signal. The parameter labelled 'Numb shots' controls the number of times a signal is read.

- Read the ENDOR data value, if desired this value can be read multiple times to increase the signal to noise ratio (figure 3.12b).

The former sequence will be repeated N times for N different RF frequencies, thus the resulting ENDOR spectrum consists of N data points, which are put into a data array. An option is available to increase the signal to noise ratio by recording a spectrum multiple times. If this option is utilised each new data point is added to the corresponding data point of the previous spectrum. In order to avoid problems when recording the first spectrum, this data array is initialised with zeroes: the zeroth spectrum equals a zero line. After a complete spectrum has been acquired the data can be saved in a file which consists of two columns: the first column contains the frequency value, the second column contains the data values of the ENDOR signal. A file like this can be used easily as an input for several plotting programs, consequently a spectrum can be printed in a desired format. The interaction with the user of the program is accomplished by a so called 'front panel'. This front panel contains graphical representations of buttons, lamps, graphs etc. The information indicated by a few of these objects are totally refreshed after a new data point has been read. The result of it is that the user is provided with 'up to date' information but a disadvantage is that the program consumes a lot of computer memory and a lot of time. The time needed to acquire a complete spectrum can be reduced by showing all information only after a complete spectrum has been acquired. A disadvantage of it is that the possibilities to interrupt a measurement or to change an acquisition parameter during a measurement have severely been diminished.

references

[1] Shane, J.J., 1993, *Electron Spin Echo Envelope Modulation Spectroscopy of Disordered Solids* (FEBOdruk, Enschede)

[2] Mims, W., 1972, *Electron Paramagnetic Resonance* (Plenum Press, New-York)

[3] Kurreck, H., Kirste, B., and Lubitz, W, 1988, *Electron Nuclear Double Resonance Spectroscopy of Radicals in Solution* (VCH Publishers, Inc.

[4] Kevan, L., and Kispert, L.D., 1976, *Electron Spin Double Resonance Spectroscopy* (John Wiley & Sons, New-York)

Chapter 4

A CW-ENDOR Resonator for Single Crystal Studies[1]

The design of an ENDOR (Electron Nuclear Double Resonance) resonator suitable for single crystal studies is reported. An outline is given of the mechanical and electronic construction of the resonator. This chapter will focus on the construction suitable for studies at 4.2 K, but the design can be easily adapted to a flow cryostat for variable temperature measurements. The RF coil efficiency has been measured and is high and fairly constant over the frequency range from 0.3 to 20 MHz. Measurements on a test compound, show that the baseline stability is good over the frequency range mentioned above. Even for low abundant nuclei as ^{13}C , the signal to noise ratio is very good.

4.1 Introduction

In Electron Nuclear Double Resonance (ENDOR) experiments a sample in a static magnetic field is subject to electromagnetic irradiation of two different wavelengths. At X band, the electron spin transitions are pumped with a microwave frequency of approximately 9 GHz. Simultaneously, the nuclear spins which are coupled to the paramagnetic centre are excited by a RF frequency. This frequency is swept slowly in the range 0.3 - 20 MHz, depending on the type of nucleus and the magnitude of the coupling. Usually a cavity resonator with some RF coil arrangement is used.

The ENDOR spectroscopy was first successfully applied by Feher in 1956. Since this time, several ENDOR resonators have been designed. However, only a few of them are suitable to perform single crystal studies. In 1967 Hutchison and Pearson [1] described an ENDOR resonator for single crystal work. This design is based upon a TE102 resonator and contains a flat single turn rectangular RF-coil in the plane of maximum microwave magnetic field. One of the first commercially available ENDOR resonators [2] was a TE011 cylindrical cavity. Four axially positioned silver rods in the cavity are connected to form a two turn RF coil. The microwave performance of this resonator is excellent but the low RF-coil efficiency makes it unsuitable for low frequency ENDOR.

---

[1] Except for section 4.6, the contents of this chapter has been published in Rev. Sci. Instrum., **63**, November 1992, pages 5362 to 5365 by J.-P. Willems, A. A. K. Klaassen, E. J. Reijerse, G. L. Janssen and E. de Boer.

Möbius and Biehl [3] used a TM110 cavity with an axially oriented helical RF coil. As the resonance frequency of a TM110 cavity does not change with the length of the cavity, this design can easily be adapted for large sample volumes. Another advantage of this arrangement is the easy sample access. The disadvantages are the usually low microwave quality factor and the low filling factor for small samples. The limited sample rotation possibility makes this design less suitable for single crystal studies.

The ENDOR resonator described by Böttcher and Heinhold [4] is based upon the design of Hutchison and Pearson, though they used a three turn RF coil. The main advantage is the excellent power efficiency of the RF coil. However, sample change is very complicated and the rotation is still limited to one axis. Because of the special sample size required in the case of this flat coil, introduction of powdered or liquid samples into the resonator leads to severe difficulties.

In this chapter we describe an ENDOR resonator based on a TE102 cavity that is optimised for single crystal studies. The design allows rotation around two mutually perpendicular axes and has a good RF-coil efficiency, especially at low RF frequencies.

4.2 The resonator

Figure 4.1 shows a view of the ENDOR resonator. The cavity and coupling iris are made of one piece of copper by means of electroforming. In order to prevent corrosion and

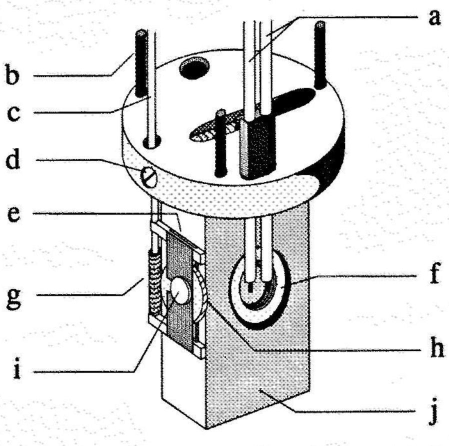

Figure 4.1
The ENDOR resonator.

a. Stainless steel RF coaxial cables	*b. Mounting screws*
c. Drive bar for rotation of the crystal	*d. Adjustable iris*
e. Rectangular frontplate of RF-coil assembly	*f. EPR modulation coil*
g. Worm which drives the crystal rotation wheel	*h. Crystal rotation wheel*
i. Crystal mounting rod glued into the rotation wheel	*j. TE102 cavity*

hence degradation of the performance the entire cavity is gold plated. The Q of the cavity without RF coil is about 4600.

In the centre of the cavity side walls there are circular area of reduced wall thickness. This wall thickness is 0.2 mm, allowing the 12.5 kHz field modulation to penetrate into the resonator. This configuration allows a modulation amplitude (B_m) of at least 15 Gauss, using our standard EPR equipment. In the middle of the front and rear walls there are rectangular slots, which serve to mount the ENDOR coil assembly.

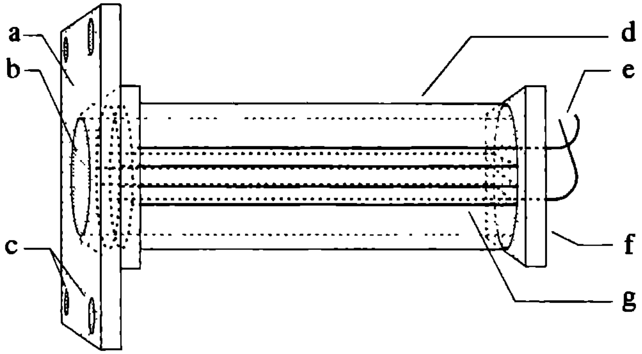

Figure 4.2
RF-coil assembly.
a. Front plate with mounting holes *b. Crystal access hole*
c. Mounting holes *d. Perspex tube*
e. Wires connecting the RF coil to the amplifier *f. Rectangular endplate*
g. Four turn RF coil

Figure 4.2 shows the RF-coil assembly used in our laboratory. A four turn RF coil is glued to the outside of a perspex tube which is inserted into the cavity at the place where the magnetic field components of the microwaves is at maximum. Care has been taken that everywhere in the cavity the coil windings are perpendicular to the microwave electric field. The position of the coil assembly is secured by rectangular endplates that fit exactly in the slots in the front and rear walls. Inserting the RF-coil assembly reduces the Q to 3500. The positioning of the coil assembly is critical, a slight misalignment degrades the quality of the resonator considerably.

The crystal is mounted at the end of a perspex rod in the centre of a rotor. This rod slides into the RF-coil tube so that the sample is in the middle of the cavity. The position of a fifteen turn potmeter dial, mounted on top of the insert, is transferred to the rotor via a stainless steel drive bar and a wormwheel arrangement (see figure 4.3). In this way, the accuracy of the crystal rotation is about 0.2°, which is satisfactory for single crystal studies. In addition to the rotor, the magnetic field can also be rotated with a rotating base magnet. This rotation, however, is restricted to approximately 160°, depending on the signal intensity (80° to either side of the zero position where all fields are perpendicular). This limitation is due to the fact that the microwave field (B_1) in the

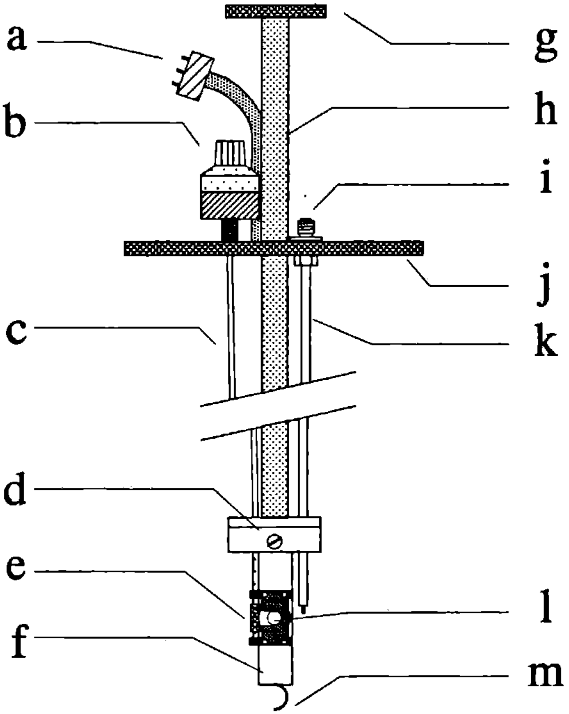

Figure 4.3
Overview of the resonator insert.
a. Multipin feedthrough
b. Potmeter dial
c. Drive bar
d. Adjustable iris
e. Wormwheel which drives the rotor wheel
f. TM102 rectangular cavity
g. Vacuum tight mylar microwave window mounted on top of waveguide
h. Stainless steel waveguide
i. Hermetically sealed bulkhead feedthrough
j. Top flange insert
k. One of the two coaxial cables
l. Sample mounting rod attached to rotor wheel
m. Brass spring used as a thermal contact

cavity is perpendicular to the magnet rotation axis, and hence, the external magnetic field will end up parallel to the B_1 field as the rotation angle approaches 90°. Furthermore, because the modulation coils are mounted on the cavity the component of the B_m field parallel to the external magnetic field, drops to zero at this position of the magnet. The perspex rod can easily be exchanged for a quartz sample tube, allowing us to perform experiments on powders or frozen solutions.

Figure 4.3 gives an overview of the CW-ENDOR (bath) cryostat insert as used in our laboratory. Microwaves are coupled to the resonator via a thin-walled stainless steel waveguide. From the top of the insert two .141" stainless steel coaxial cables are connected to the RF coil.

Boiling helium in the resonator causes excessive noise and degrades the spectrometer performance. Therefore, a cavity shielding pod encloses the entire insert and prevents liquid helium from entering the resonator (this shielding pod is not shown in figure 4.3 for clarity reasons). Except for the lower copper section, this pod is made of stainless steel. Thermal contact between the cavity and the lower end of the pod is made via a brass spring. Apart from the waveguide feedthrough, the sample rotation port and the two RF connectors the insert flange contains a multipin feedthrough for field modulation and temperature measurement at the resonator wall. For the latter purpose a 82 Ω Allen-Bradley resistor is used.

4.3 Impedance matching of the RF-coil

CW-ENDOR applications usually require large RF sweeps. In order to keep the amplitude of the RF field (B_2) constant, the impedance of the coil has to be matched to the output impedance of the amplifier over this sweep range. A broad band matching circuit is described by Colligiani et al. [5]. However, this circuit is very complicated and limits the sample to a very small volume. By placing a capacitor to ground after every coil winding one creates a π system or low-pass filter. If such a system is terminated by a 50 Ω load, the passband shows good matching. This method puts no limits on the sample size but it is still very complicated and difficult to construct.

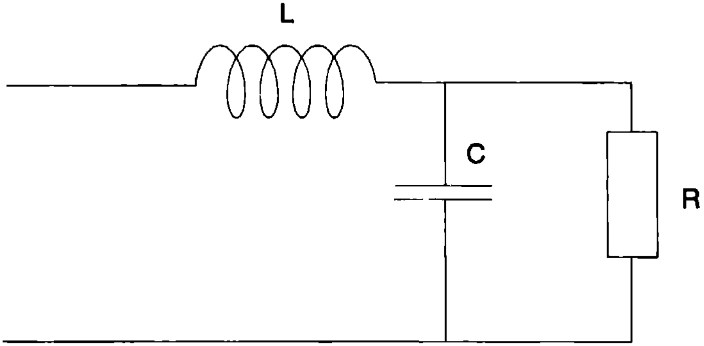

Figure 4.4
Electronic scheme of the RF-coil assembly.
$L \approx 0.5 \mu H$, $C = 100\ pF$, $R = 50\ \Omega$

We decided for a compromise between simplicity and broad band operation: a single capacitor to ground is placed parallel to the 50 Ω termination (figure 4.4). Since the minimum length of the RF input line in our cryostat is 1 m, it cannot be neglected for the calculation of the input impedance. The input impedance of a transmission line terminated by an impedance Z_n is given by:

$$Z = Z_0 \frac{Z_n \cos(kl) + jZ_0 \sin(kl)}{Z_0 \cos(kl) + jZ_n \sin(kl)}$$

where : l is the length of the input line,
k is the wave number
Z_0 is the characteristic impedance.

For a transmission line with an ENDOR coil and a load Z_0 in series $Z_n = j\omega L + Z_0$, where L is the inductance of the ENDOR coil (which is for our setup typically 0.5 μH) and ω is the frequency in rad/s. Figure 4.5 presents the calculated input impedance of this circuit as a function of the length of the input line at a frequency of 15 MHz and 20 MHz (Figure 4.5a and 4.5b, respectively). Figure 4.5a shows that the input impedance is 50 Ω when the input line has a length of approximately 4.5 m. At 20 MHz however this length has to be approximately 3 meters. As a compromise an input line length of 4 m has been taken. Figure 4.6a shows the calculated input impedance of this circuit as a function of the frequency. Figure 4.6b gives the input impedance for the circuit which is indicated in figure 4.4. In this case, $Z_n = j\omega L + (j\omega C + 1/Z_0)^{-1}$, where C is the capacity. From figure 4.6 it is clear that the frequency dependence of the circuit with a capacitor, is smoother than that of the circuit without one.

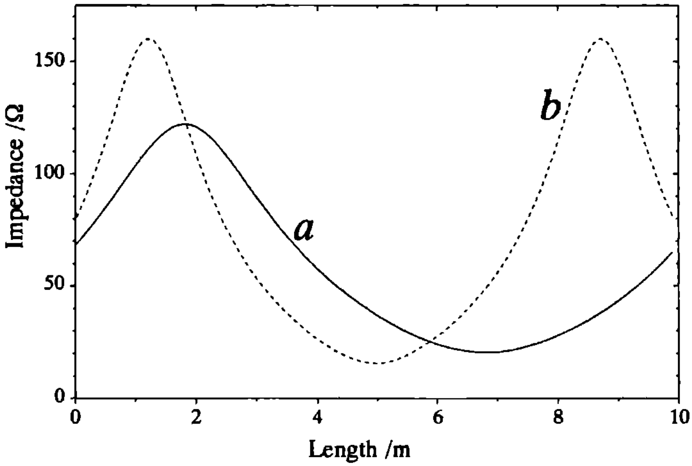

Figure 4.5
Calculated input impedance of the RF-coil assembly as a function of the length of the input line
a RF frequency: 15 MHz (solid line)
b RF frequency: 20 MHz (dashed line)

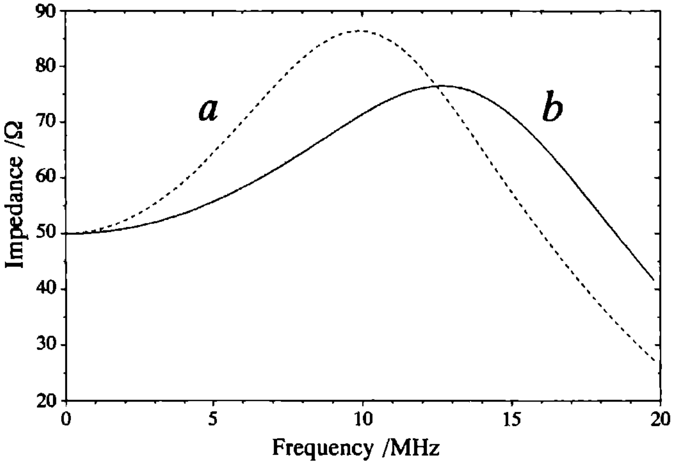

Figure 4.6
Calculated frequency dependence of the RF-coil assembly. The length of the input line is 4 m.
a With a 50 Ω load (dashed line)
b With a 50 Ω load and a 100 pF capacitor (solid line)

4.4 The spectrometer

The CW-ENDOR insert was tested with a home built ENDOR accessory on a Bruker ESP300 spectrometer. The RF excitation part consists of a HP8601 RF generator and an ENI A300 power amplifier[2]. Frequency sweep is accomplished via the FM port of the generator with a homemade ramp generator which is also used to drive the recorder X axis. The modulation signal from a lock- in amplifier is added to the ramp in a summing amplifier. This combined signal is then fed to the FM port of the RF generator. The RF modulation amplitude is also controlled by the ramp generator. Modulation amplitudes up to 0.7 MHz are feasible, though rarely used. The modulation frequency can be varied from 0.2 to 210 kHz. For ENDOR measurements a typical modulation frequency of 2 kHz is used. The RF sweepwidth can be continuously varied up to 20 MHz. The RF sweeptime can be varied from 10 to 9990 s in steps of 10 s. After detection by the crystal detector in the microwave bridge, the ENDOR signals are amplified and demodulated in a PAR 124A lock-in amplifier.

---

[2] The experimental ENDOR setup described here was the setup used until 1993. In the middle of 1993 the setup was 'upgraded' by means of a computer controlled RF frequency sweeper, resulting in the set up shown in figure 3.11 in chapter 3.

4.5 Results

The RF fields in the resonator were measured with the method described by Miyagawa et al.[6]. In table 4.1 the magnitude of the RF fields in the rotating frame for a number of frequencies are listed. In this table also, the coil efficiency factor Λ defined as $\Lambda = B/\sqrt{P}$ is given.

Table 4.1
The magnitude of the RF fields in the rotating frame and the coil efficiency factor Λ, for a number of frequencies.

	Frequency /MHz					
	8	10	12	15	17	20
B_2 /G	6.1	4.5	4.1	4.8	5.2	4.3
$\Lambda/G\,W^{-\frac{1}{2}}$	1.1	0.8	0.7	0.9	0.9	0.8

As a test compound NaCl doped with 0.5% $K_3Fe(CN)_6$ [7] (see also chapter 5) was used. A single crystal (size 2×2×2 mm) was mounted on the perspex rod and oriented with the magnetic field ($\vec{B}_0$) parallel to the crystallographic XY plane. All measurements

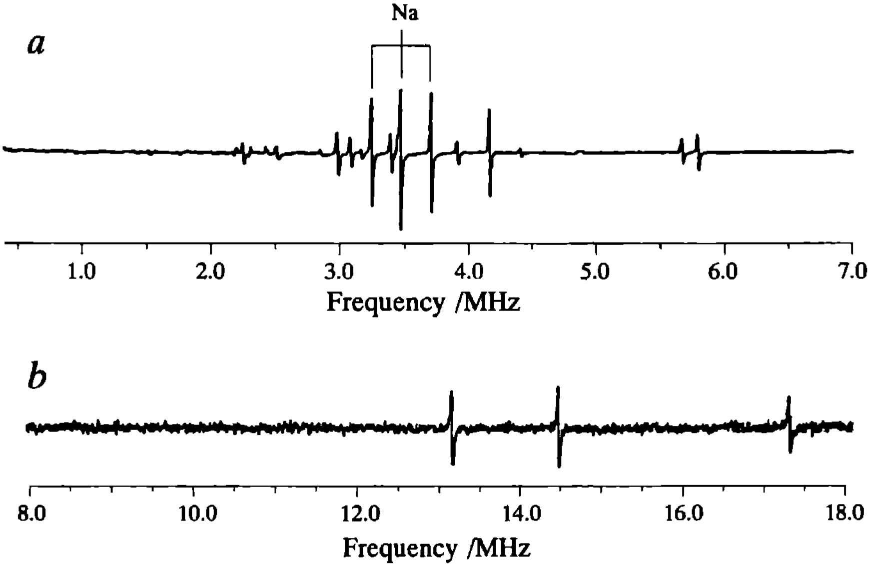

Figure 4.7
a A typical low frequency ENDOR spectrum of $K_3Fe(CN)_6$ in NaCl. Microwave power P_{EPR}= 0.1 mW, RF power P_{RF} = 5 W
b ^{13}C ENDOR spectrum of $K_3Fe(CN)_6$ in NaCl. Microwave power P_{EPR}= 0.1 mW, RF power P_{RF} = 31 W

were carried out in a bathcryostat at 4.2 K. The microwave power used to saturate the EPR-transitions was 0.1 mW.

Figure 4.7a shows a typical ENDOR spectrum in the low frequency range. The ENDOR response was measured with a RF power of 5 W. In the spectrum ^{14}N and ^{23}Na ENDOR lines can be distinguished. The assignment is made from the different angular dependencies of the ^{14}N and ^{23}Na signals in the spectrum [7] (see chapter 5). Figure 4.7b shows a ^{13}C ENDOR spectrum with ^{13}C in natural abundance. In this case the RF power had to be raised to 31 W in order to measure the spectrum. Due to the low natural abundance (1.1%) the signal to noise ratio of the ^{13}C spectrum is less than that of ^{14}N or ^{23}Na . The minimum linewidth measured with this setup was 10 kHz which is acceptable for most ENDOR studies.

4.6 EPR Modulation

In order to optimise the sensitivity of the ENDOR resonator, the electric losses of the microwaves have to be minimised. Therefore, the conductivity of the resonator walls has to be as high as possible. In our resonator this has been realised by gold plating the copper walls. The high conductivity of the walls has one disadvantage: the modulation field, needed to detect an EPR signal, will be severely attenuated while travelling through these walls. When electromagnetic waves travel through a conducting material the oscillating electromagnetic field of these waves introduces currents in the conducting material. A part of the energy of the waves is used to drive these currents. Therefore, electromagnetic waves travelling through a conducting material will be reduced. These waves can be described by the differential equation for a damped oscillating wave travelling in the z direction given by:

$$\frac{\partial^2 B}{\partial z^2} = \mu\mu_0\sigma\frac{\partial B}{\partial t}. \tag{4.1}$$

In this equation σ denotes the conductivity of the material. The general solution for equation 4.1 is presented by:

$$\begin{aligned} \vec{B} &= \vec{B}_0\, e^{j(\omega t - z/\delta)} e^{-z/\delta} \\ \text{where } \frac{1}{\delta} &= \sqrt{\tfrac{1}{2}\mu\mu_0\sigma\omega}. \end{aligned} \tag{4.2}$$

The quantity δ measures how rapidly the wave is attenuated and is called the skin depth. As is shown by equation 4.2, the skin depth depends upon the conductivity σ of the material and on the frequency ω of the electromagnetic wave. Figure 4.8 displays the relation between the frequency of the EM wave and the distance the wave travels through the conducting material. This figure shows that the modulation field having a frequency of 100 kHz is attenuated so that less than 40 % of its original strength remains after it has travelled 0.2 mm through a copper material, while a modulation field having a frequency of 1 kHz has 90 % of its original strength after it has travelled the same distance. The wall

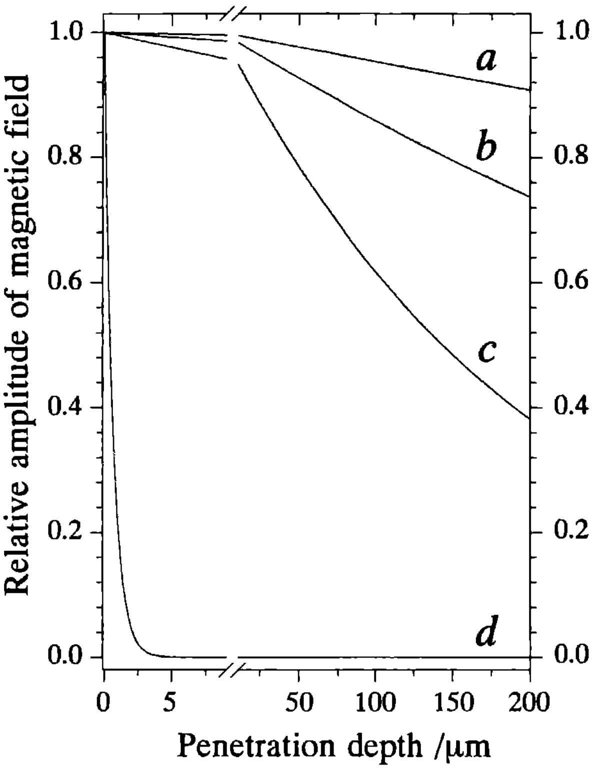

Figure 4.8

The calculated relative magnetic amplitude of a travelling electromagnetic wave as a function of the travelling distance through a copper medium, for four different frequencies, ν_{EM}. The travelling distance has been denoted as 'Penetration depth' in the figure. The horizontal axis has been expanded between 0 and 10 μm.

a: ν_{EM} = 1 kHz

b: ν_{EM} = 10 kHz

c: ν_{EM} = 100 kHz

d: ν_{EM} = 10 GHz

thickness at the position of the modulation coils is approximately 0.2 mm, so a modulation frequency of less than 100 kHz is suitable, see also figure 4.8. From figure 4.8 it can be deduced that a conducting resonator wall thickness of 10 μm is enough to detain the microwave field inside the cavity. To improve the mechanical strength of the resonator the walls can in principle be thickened by a non conducting material, though the actual construction of such a resonator is rather problematic.

There are a few disadvantages of a low modulation frequency. The most important one is that the so called "1/f noise" increases by decreasing the modulation frequency. As a result the signal to noise ratio of the EPR spectrum will be lower when using low modulation frequencies. The alternative for using a low modulation frequency is to increase the amplitude of the modulation field. An increase in the maximum modulation field will result in an absolute increase of B_m at the position of the sample. Yet, there is a practical limit on the maximum modulation field i.e. a limit on the current through the modulation coils, which is related to the maximum current the current source of the EPR console can supply. A disadvantage of using higher modulation fields is that it tends to produce baseline distortions. The next paragraph will explain this in more detail.

One aspect we have not paid attention to so far, is that the resonator described in this chapter is designed to be resonant for a microwave frequency, but it happens to be resonant for 'acoustic' waves as well. Test measurements have indicated that these acoustic resonances appear at low temperatures ($T \leq 20$ K) if helium gas is present inside the cavity. These resonances cause severe baseline variations in the EPR spectrum. Therefore, the pod has to be evacuated in order to avoid the occurrence of these disturbances. It turns out that the acoustic resonances are driven by the modulation coils. These coils carry an alternating current which, when placed in a permanent magnetic field, will give rise to a Lorentz force exerted out the cavity walls. The magnitude of this force (F_m) depends upon the geometry of the coils, the distance between the modulation coils and the poles of the external magnet, the strength of the external magnetic field, the magnitude of the modulation field etc., and is given by [8]:

$$F_m \approx \frac{I\, B_m\, S}{z} \tag{4.3}$$

with : B_m the (alternating) modulation field.

I the current through the coils of the external magnet.

S the area of a pole of the external magnet.

z the distance between a modulation coil and a pole of the external magnet.

For the resonator assembly described in this chapter, one typically finds a magnetic force of $F_m = 2$ N. Because this force alternates with the modulation frequency, it can be held responsible for the generation of the acoustic resonances in the cavity. Equation 4.3 also shows that the magnetic force, and thus the baseline variations, increase with increasing amplitude of the modulation field. This prediction is confirmed by the test measurements.

References

[1] Hutchison Jr., C.A. and Pearson, G.A., 1967, *J. Chem. Phys.*, **47**, 520

[2] Varian Associates 611 Hansen way Palo Alto California 94303 USA

[3] Möbius, K., and Biehl, R., 1979, *Multiple Electron Resonance Spectroscopy* ed Dorio, M.M., and Freed, J.H., (New York Plenum)

[4] Böttcher, R., and Heinhold, D., 1986, *Experimentelle Technik der Physik*, **34**, 87

[5] Colligiani, A., Pinzino, C., and Bertolini, M., 1979, *J. Magn. Res.*, **33**, 511

[6] Miyagawa, I., Hayashi, Y., and Koiaki, Y., 1977, *J. Magn. Res.*, **25**, 183

[7] Kirmse, R., Böttcher, R., Willems, J.-P., Reijerse, E.J. and de Boer, E., 1991, *J. Chem. Soc. Faraday Trans.*, **87**, 3105

[8] Grant, I.S., and Phillips, W.R., 1975, *Electromagnetism* (John Wiley & Sons Ltd New York)

Chapter 5

Single-crystal ^{13}C, ^{14}N and ^{23}Na ENDOR on $Fe(CN)_6^{3-}$ Doped into NaCl[1]

A single-crystal ENDOR study on the 3d^5 (S=$\frac{1}{2}$) low-spin complex $Fe(CN)_6^{3-}$ doped into NaCl is reported. Among the various centres caused by different configurations of two charge-compensating cation vacancies the orthorhombic centre, I_a, which is characterised by a large g anisotropy has been selected for this investigation. ENDOR transitions due to ^{13}C , ^{14}N and ^{23}Na are observed; nearly all hyperfine and nuclear quadrupole coupling tensors were determined. The ^{14}N spectra are strongly influenced by the nuclear quadrupole interaction which reaches a magnitude comparable to that of the hyperfine and nuclear Zeeman interaction. The orientations of the principal axes of all tensors confirm the D_{2h} symmetry and the positions of the negatively charged cation vacancies assumed for the centre I_a. The ^{13}C couplings are quite large, indicating a noticeable covalency of the Fe-C bonds. The hyperfine and nuclear quadrupole data are used to discuss qualitatively the spin density distribution in the $Fe(CN)_6^{3-}$ unit. Comparison with other experimental studies on the spin distribution reveal that the effect on the vacancies on the spin distribution is large. For interpretation of the ^{14}N quadrupole data the Townes-Dailey model has been applied.

5.1 Introduction

The chemistry and many spectroscopic properties of hexa-coordinated 3d transition-metal cyanide complexes of the type $M(CN)_6^{3-}$ were investigated to a large extend because the CN^- ligand is the classic example of a ligand forming low-spin complexes [1-2] with covalent metal-carbon bonds. However, whereas several EPR studies on nitrosylpentacyanometallates $[M(CN)_5(NO)]^{3(4)-}$ and dihalogenotetracyanometallates $[M(CN)_4X_2]^{3(4)-}$, have been reported [3-8], the number of EPR studies on $M(CN)_6^{3-}$ complexes is small [9-14]. Attempts at detection of ligand hyperfine splitting by EPR for $M(CN)_6^{3-}$ complexes have

---

[1] The contents of this chapter has been published in J. Chem. Soc. Faraday Trans., **87**, 1991, pages 3105 to 3111, by: R. Kirmse, R. Böttcher, J.-P. Willems, E.J. Reijerse and E. de Boer.
A few figures and figure captions in this chapter are slightly different from those published in the paper. The reason for this is that the measurements have been repeated, using the resonator described in chapter 4.

failed up to now. They would provide, however, a detailed description of the spin density distribution over the molecule.

Very recently, an ENDOR and ESEEM study on $Fe(CN)_6^{3-}$ doped into KCl crystals has been reported by Wang and de Boer [13] in which for a hexacyanometallate a first analysis of the ligand hyperfine splitting interaction with the ^{13}C and ^{14}N was given. The signals of the four equatorially coordinated ^{14}N and ^{13}C nuclei of the CN ligands as well as those of the ^{13}C nuclei of the axial CN ligands were observed. For ^{13}C only the transitions of one spin manifold were found, leading to an uncertainty in the determination of the coupling constants and the directions of the corresponding principal axes.

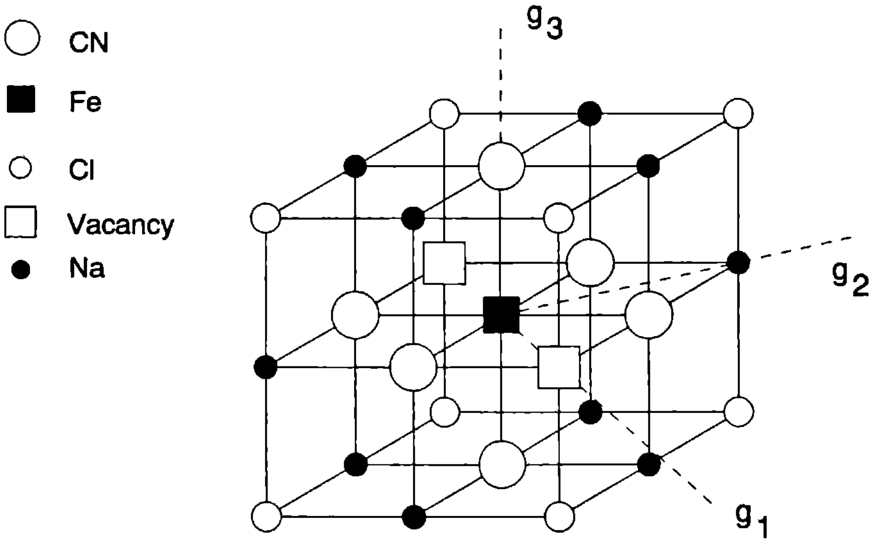

Figure 5.1
Model of I_a for $Fe(CN)_6^{3-}$ in NaCl. The orientations of the principal components of the g tensor have been indicated.

In this chapter we report a detailed ENDOR study on $Fe(CN)_6^{3-}$ incorporated in NaCl in order to obtain a more general picture about the ligand hyperfine splitting interactions. Besides the ^{14}N ENDOR transitions and the ENDOR signals of the two equatorially arranged ^{23}Na nuclei, the ^{13}C ENDOR transitions of both spin manifolds were observed, allowing an unambiguous determination of the coupling constants. Since the investigations on KCl:$Fe(CN)_6^{3-}$ and NaCl:$Fe(CN)_6^{3-}$ were made on the same centre, called I_a (see figure 5.1), the results obtained from both studies can be compared. The ligand hyperfine splitting parameters and the nuclear quadrupole data will be used to discuss the spin density distribution in the $Fe(CN)_6^{3-}$ centre.

5.2 Experimental

The crystal growth and the EPR spectra of NaCl:$Fe(CN)_6^{3-}$ crystals have been reported [14]. The ENDOR spectrometer used has been described previously [15] (see also chapter 4). The ENDOR spectra were measured at a temperature of 4.2 K using a bath cryostat. Measurements have been made in the (g_1, g_2) plane ($\vec{B}_0 \perp$ [001]), in a plane containing the [100] and [111] axes, and for some angles in the plane spanned by the [110] and [001] axes. Depending on the complexity of the spectra, recordings were made at 5° or 2.5° intervals. The data analysis was performed using the universal program package MAGRES [16].

5.3 Results

EPR spectra

The incorporation of $Fe(CN)_6^{3-}$ into the NaCl lattice leads to a replacement of an $NaCl_6^{5-}$ unit. Consequently, two cation vacancies are produced to maintain the neutrality of the lattice. Since the charge compensating vacancies may be differently oriented with respect to the incorporated $Fe(CN)_6^{3-}$ unit, a large number of paramagnetic centres with local symmetries D_{2h}, C_2 and C_s are expected. This was observed in the EPR spectra [14]. The orthorhombic centre (I_a) is more highly populated than the others. Therefore, this centre was chosen for our ENDOR studies.

The EPR spectra of centre I_a can be described by an effective spin Hamiltonian with $S=\frac{1}{2}$:

$$\mathcal{H} = \beta_e \vec{B}_0 \cdot \bar{\bar{g}} \cdot \vec{S}.$$

The principal values of the g tensor were found to be: g_1=2.262, g_2=2.918 and g_3=0.635; the directions of the principal axes are $g_1 \parallel$ [110], $g_2 \parallel$ [-110] and $g_3 \parallel$ [001] [14]. Neither ^{57}Fe nor ligandhyperfine interactions were observed. A similar situation was found for $Fe(CN)_6^{3-}$ incorporated into KCl crystals [13]. The g values observed in that case for I_a (g_1=2.079, g_2=3.056 and g_3=0.400) differ only slightly from the values found for NaCl:$Fe(CN)_6^{3-}$.

Two features of the EPR spectra, which are due to the large g-anisotropy of the system studied, should be briefly commented in this section because of their importance for the ENDOR measurements:

- there is a strong change in the EPR line intensity among the symmetry related sites.
- the linewidth depends critically on the direction of the $\vec{B}_0$ field with respect to the principal axes of g. The EPR linewidth (ΔB_{pp}) is quite narrow at low fields (ca. 1 mT), but it increases significantly at higher fields; for $\vec{B}_0 \parallel g_3$: $\Delta B_{pp} > 15$ mT.

According to this the observation of ENDOR spectra becomes most difficult for $\vec{B}_0$ orientations outside the (g_1, g_2) plane because of the noticeable decrease of the signal intensity.

ENDOR spectra

General remarks

In the ENDOR spectra transitions belonging to the nuclei ^{13}C (in natural abundance), ^{14}N and ^{23}Na were observed. They can be clearly distinguished by their frequency regions, their linewidths and intensities.

The ^{14}N ENDOR transitions were found in the range 0-6MHz, those of the ^{13}C nuclei, which were the least intense transitions in the spectra, were detected between 6.5 and 17.5 MHz. The linewidth of the ^{14}N transitions is very small, 12-18 kHz, depending on the $\vec{B}_0$ orientations. The linewidth of the ^{13}C transitions is noticeable larger: ca 60 kHz. ^{23}Na ENDOR transitions were observed in the 3-4 MHz range for all spectra studied. They lie, therefore, in the same region as the ^{14}N transition; however, they are easily distinguished by their angular dependence and their line intensities, the latter being larger by a factor of ca two.

^{14}N ENDOR spectra

The ^{14}N ENDOR spectra are characterised by the signals of two magnetically distinguishable pairs of equatorial ^{14}N nuclei. In most cases four or five transitions per ^{14}N nucleus can observed. This indicates that the magnitude of the ^{14}N nuclear quadrupole interaction ($\mathcal{H}_Q$) reaches that of the sum of the nuclear hyperfine coupling ($\mathcal{H}_{HF}$) and the nuclear Zeeman interaction ($\mathcal{H}_{NZ}$). According to this, state mixing between the individual m_I states occurs and six transitions are expected for each ^{14}N nucleus because the '$\Delta m_I = \pm 2$' transitions acquire appreciable intensity [17-19]. The energy level scheme and the assignment of the transitions are given in figure 5.2. In figure 5.3 the angular dependence of the ^{14}N

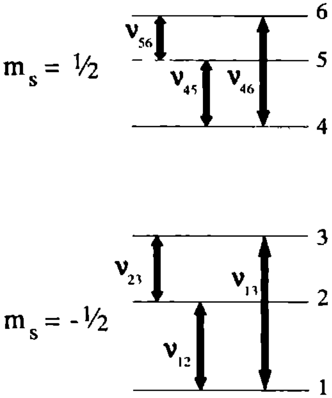

Figure 5.2
Energy-level diagram for $S = \frac{1}{2}$ *and* $I = 1$ *(*^{14}N*), with* $\vec{B}_0$ *at an arbitrary orientation, showing the possible ENDOR transitions*

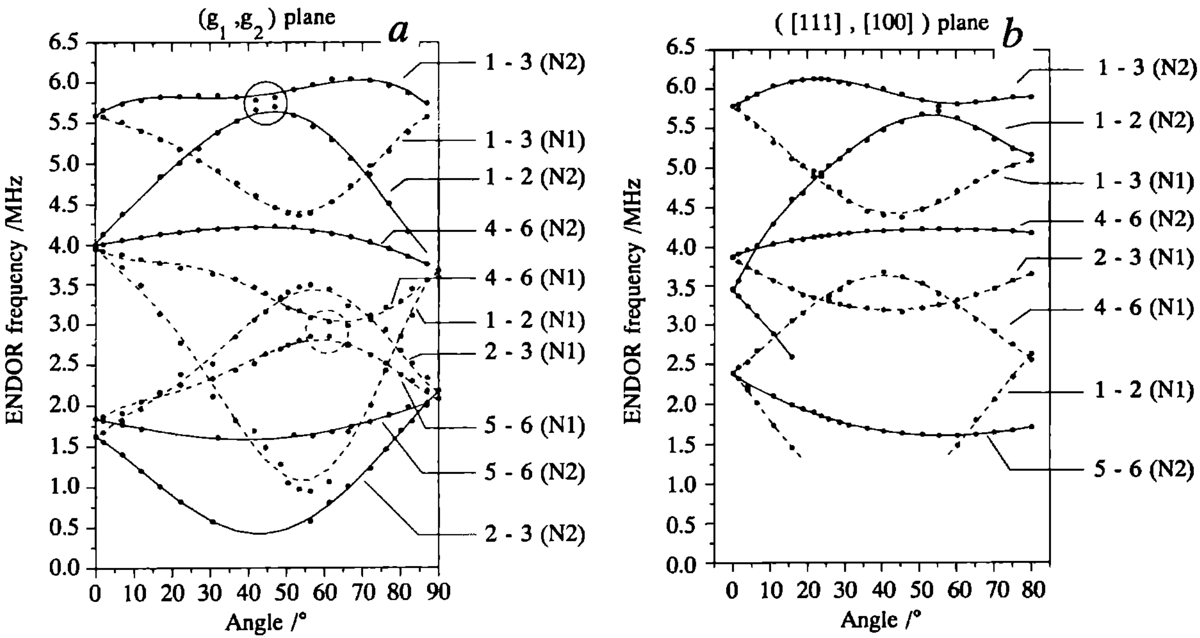

Figure 5.3
Experimentally obtained angular dependence of the ^{14}N ENDOR transitions. Dashed lines: atom 1, solid lines: atom 2.
a $\vec{B}_0 \parallel (g_1, g_2)$ plane. At an angle of 0°, $\vec{B}_0$ is parallel to the g_2 axis, at an angle of 90°, $\vec{B}_0$ is parallel to the g_1 axis. The circles indicate the level anticrossing.
b $\vec{B}_0 \parallel$ ([111], [100]) plane. At an angle of 0° $\vec{B}_0$ is parallel to the [111] axis.

ENDOR transitions for $\vec{B}_0 \perp [001]$ and for $\vec{B}_0 \perp [0\text{-}11]$ are reproduced. The intensities of the '$\Delta m_i = \pm 2$' transitions (1↔3, 4↔6) are very strong, while the other transitions are weaker and their intensity is very dependent on the direction of $\vec{B}_0$. The 4↔5 transitions could not be detected.

In the analysis of the ^{14}N spectra we used the standard spin Hamiltonian for a single nucleus coupled with one unpaired electron ($S=\frac{1}{2}$):

$$\mathcal{H} \;=\; \mathcal{H}_{EZ} + \mathcal{H}_{HF} + \mathcal{H}_{NZ} + \mathcal{H}_{Q}.$$

where

$$\begin{aligned} \mathcal{H}_{EZ} + \mathcal{H}_{HF} + \mathcal{H}_{NZ} &= \beta_e\, \vec{B}_0 \cdot \overline{\overline{\mathrm{g}}} \cdot \vec{S} + \vec{S} \cdot \overline{\overline{\mathrm{A}^N}} \cdot \vec{I} - g_N\, \beta_N\, \vec{B}_0 \cdot \vec{I} \\ \mathcal{H}_Q &= \vec{I} \cdot \overline{\overline{\mathrm{Q}^N}} \cdot \vec{I} \\ &= K\left[\left(3I_z^2 - I^2\right) + \eta\left(I_x^2 - I_y^2\right)\right] \\ \text{with} \qquad & 2K = Q_3 = e^2qQ/2h \qquad\qquad (5.1) \\ \text{and} \qquad & \eta = \left|\frac{Q_1 - Q_2}{Q_3}\right|. \end{aligned}$$

where eq = V_{33} is the largest principal value of the electric field gradient tensor. The order of the principal values of Q is taken as $\left|Q_1^N\right| \le \left|Q_2^N\right| \le \left|Q_3^N\right|$. The ENDOR frequencies have been analyzed by complete diagonalisation of the spin Hamiltonian. The principal values of the ^{14}N hyperfine splitting and the ^{14}N nuclear quadrupole tensor and their directions relative to the g tensor axis are given in table 5.1; the positions of the principal axes are illustrated in figure 5.4.

The angular dependence observed for the ^{14}N transitions is close to that recently reported for KCl:Fe(CN)$_6^{3-}$ [13]. As found for KCl:Fe(CN)$_6^{3-}$, level anti crossing between the spin energy levels is observed for the transitions 1↔3, 1↔2 (ca 44° away from the g_1 axis), and also for the transitions 4↔6,5↔6 (ca 26° away from g_1). This is important to note since otherwise the angular dependence could be misunderstood. Furthermore, the angular dependence show that the signals of the two ^{14}N pair become coincident for $\vec{B}_0 \parallel g_1$ ([100]), $\vec{B}_0 \parallel g_2$ ([-110]) and $\vec{B}_0 \parallel g_3$ ([001]). According to this, the planes spanned by (g_1,g_3) , (g_2,g_3) and (g_1,g_2) are mirror planes. This is also confirmed by the fact that one of the principal axes of the A^N and Q^N lies almost parallel to the g_3 ([001]) direction. The other two principal axes of A^N and Q^N are not found to lie exactly parallel to the bisector of the g_1, g_2 axes (the [010] axis). They appear to be rotated somewhat towards the position of the Na atoms.

Finally it should be noted that in the 3.3-3.8 MHz region there are two other transitions which can be followed over a limited angular region. According to their intensities they should be assigned to the axial ^{14}N nuclei. However, because of insufficient data being available a complete analysis could not be made.

^{13}C ENDOR

Six ^{13}C ENDOR transitions were observed in the frequency range 6.5-17.5 MHz, which is outside the range where the ^{14}N transitions were found. Figure 5.5 shows the ^{13}C ENDOR

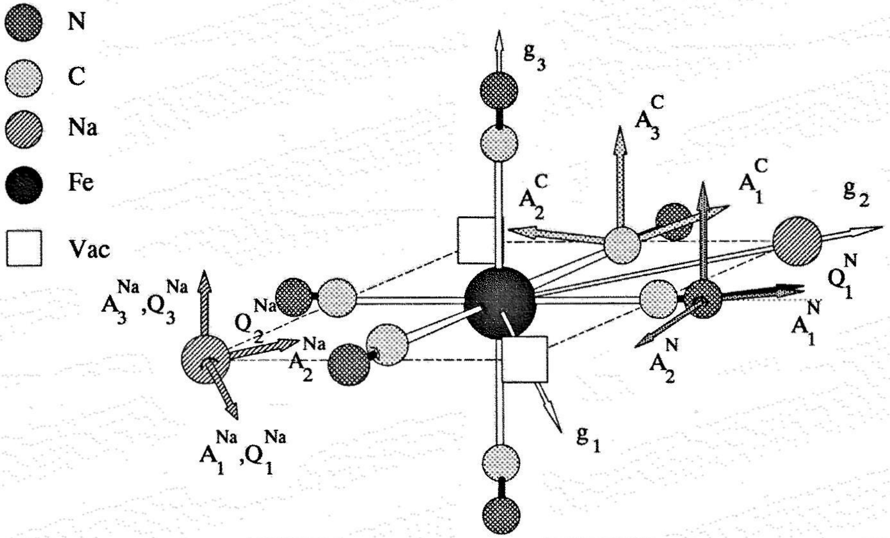

Figure 5.4
Directions of the principal axes of A^C, A^N, Q^N, A^{Na} and Q^{Na} in the molecular frame

spectrum obtained for $\vec{B}_0 \parallel [100]$. The three low-frequency transitions are by a factor 5-20 less intense than the corresponding ones in the high-frequency region. This indicates that they belong to different m_s manifolds. The behaviour found for the ^{13}C ENDOR transitions is quite normal and similar pictures were observed also for other systems [20-22]. It can be explained by the hyperfine enhancement factor, E, which for an isotopic

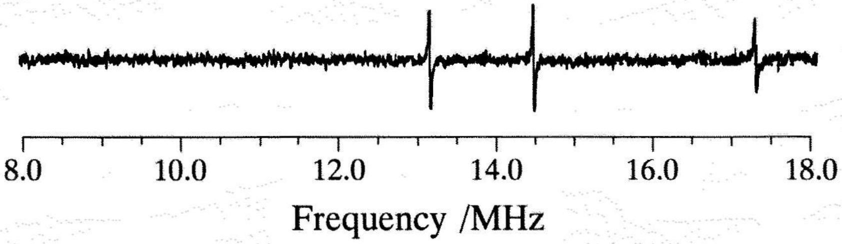

Figure 5.5
Experimental ^{13}C ENDOR spectrum of $Fe(CN)_6^{3-}$ in NaCl for $\vec{B}_0$ in the (g_1, g_2) plane; 2.5° away from [100]. Only the high frequency ^{13}C lines are visible.

Table 5.1
Principal values and the directions of the hyperfine and quadrupole tensors of $Fe(CN)_6^{3-}$ *in NaCl.*
All signs are relative. The principal values of the tensors of $Fe(CN)_6^{3-}$ *in KCl are also given for comparison.*

		Principal values / 10^{-4} cm^{-1}		Angles with respect to the principal axes of the g tensor		
		NaCl	KCl	g_1	g_2	g_3
A(^{14}N)	A_1^N	1.38	1.43	53	39	85
	A_2^N	0.61	0.45	141	51	90
	A_3^N	-1.71	-1.53	93	94	5
Q(^{14}N)	Q_1^N	0.22	0.32	141	50	90
	Q_2^N	0.41	0.32	87	86	175
	Q_3^N	-0.64	-0.64	51	40	85
A(^{13}C$_{eq}$)	A_1^C	6.69	6.06	57	33	90
	A_2^C	9.79	9.49	147	57	90
	A_3^C	-	-			
A(^{13}C$_{ax}$)	A_1^C	6.75	5.77	0	90	90
	A_2^C	8.66	8.85	90	0	90
	A_3^C	-	-			
A(^{23}Na)	A_1^{Na}	0.12		0	90	90
	A_2^{Na}	0.63		90	0	90
	A_3^{Na}	0.12		90	90	0
Q(^{23}Na)	Q_1^{Na}	-0.015		0	90	90
	Q_2^{Na}	-0.032		90	90	0
	Q_3^{Na}	0.047		90	0	90

system is defined by:

$$E = 1 - \frac{m_s A^C_{iso}}{\nu^C_I}. \tag{5.2}$$

where A^C_{iso} is the isotropic part of A^C and ν^C is the Larmor frequency of the ^{13}C nucleus [23] (see also section 2.2). In figure 5.6 the angular dependence of the ^{13}C transitions in the (g_1, g_2) plane is shown. The lines due to the equatorial carbons can be distinguished easily from those of the axial ones. The angular dependence of the four equatorial ^{13}C nuclei generally show the same behaviour as observed for the equatorial ^{14}N nuclei: two pairs of equivalent ^{13}C nuclei are found which become equivalent for $\vec{B}_0 \parallel g_1(g_2)$. Furthermore, as found for the ^{14}N nuclei the principal directions of the equatorial ^{13}C nuclei are somewhat rotated from the iron-cyanide direction, confirming the influence of the cation vacancies. The principal axes are given in table 5.1 and figure 5.4.

Owing to the low local symmetry the determination of the principal values of the ^{13}C tensor of the equatorial carbon atoms must be obtained by diagonalisation the corre-

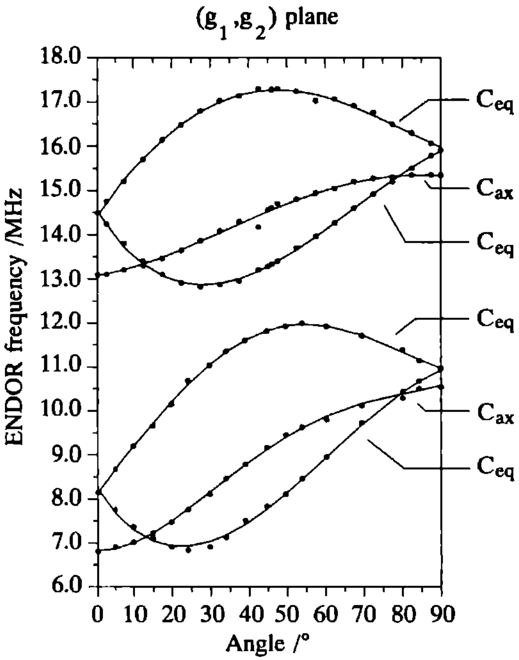

Figure 5.6
Experimentally obtained angular dependence of the ^{13}C *ENDOR transitions. At an angle of 0°,* $\vec{B}_0$ *is parallel to the* g_2 *axis, at an angle of 90°.* $\vec{B}_0$ *is parallel to the* g_1 *axis.*

sponding spin- Hamiltonian matrix [24,25]. The principal values of the ^{13}C tensors of the axial carbons can be obtained directly from the spectra for $\vec{B}_0 \parallel g_1(g_2)$. Unfortunately the complete ^{13}C tensors could not be obtained, since for $\vec{B}_0$ directions outside the (g_1, g_2) plane the intensity of the ^{13}C ENDOR transitions decrease rapidly as a consequence of the rapid decrease in the EPR intensity for those orientations.

In this context a comment should be made about the equatorial ^{13}C tensors reported for KCl:Fe$(CN)_6^{3-}$ [13]. In that case only the ^{13}C ENDOR transitions belonging to the one m_s manifold were observed. They have to be assigned to the low-frequency ^{13}C transitions. According to our present study this assignment is incorrect, they should have been assigned to the high-frequency transitions. Consequently, the correct values of the ^{13}C tensor components of the equatorial carbon atoms will be lower by a factor of $2\nu_l^C$ (ν_l^C is the Larmor frequency of ^{13}C), as has been reported [13]. In table 5.1 the principal values of A(^{14}N), Q(^{14}N), A($^{13}C_{eq}$) and A($^{13}C_{ax}$) for the system KCl:Fe$(CN)_6^{3-}$ are given.

^{23}Na ENDOR

Three ^{23}Na ENDOR transitions have been observed in the 3-4 MHz region of all ENDOR spectra. Figure 5.8 shows their angular dependence in the (g_1, g_2) plane. A typical ^{23}Na ENDOR spectrum also showing the ^{14}N ENDOR transitions has been reproduced in figure 5.7.

The behaviour of ENDOR spectra for $I=\frac{3}{2}$ (frequency and transition probabilities) has recently been described in detail [26]. According to this, the angular dependence of the observed ^{23}Na transitions can be explained assuming the relation $\mathcal{H}_{HF} + \mathcal{H}_{NZ} \gg \mathcal{H}_Q$. In this case three ^{23}Na ENDOR transitions with comparable intensity are expected. These transition belong to the same m_s manifold. The intensity of the corresponding transitions of the other m_s manifold is smaller.

In the analysis of the spectra the spin Hamiltonian given above was used. K is defined by:

$$12K = 6Q = e^2qQ/h. \tag{5.3}$$

The ^{23}Na hyperfine tensor is axially symmetric; the direction of the maximum component, A_2^{Na}, coincides with that of g_2. The magnitude of the ^{23}Na quadrupole interaction is ca 10 times smaller than the ^{23}Na hyperfine interaction. The maximum component of the ^{23}Na quadrupole tensor Q_3^{Na} lies parallel to A_2^{Na}. The Q^{Na} tensor is found to be rhombic. The principal values of the tensors are given in table 5.1 together with their directions with respect to the principal axes of the g tensor.

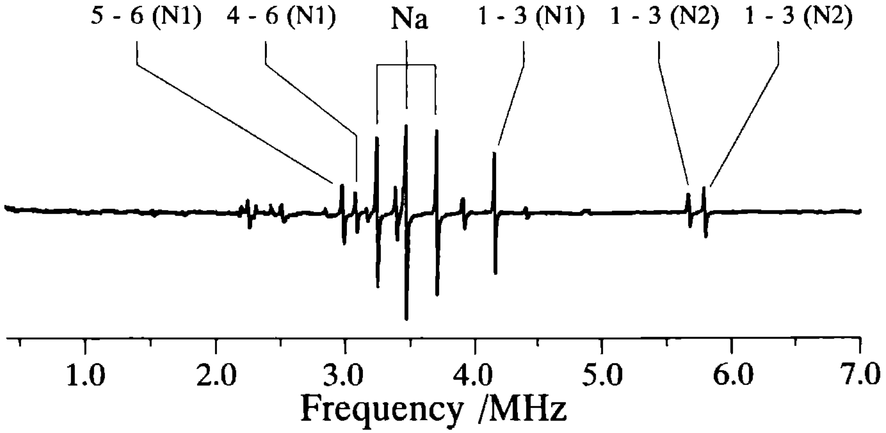

Figure 5.7
Experimentally obtained ENDOR spectrum of $Fe(CN)_6^{3-}$ in NaCl for $\vec{B}_0$ in the (g_1, g_2) plane, 2.5° away from [100]. The ^{23}Na transitions and a few ^{14}N transitions have been indicated.

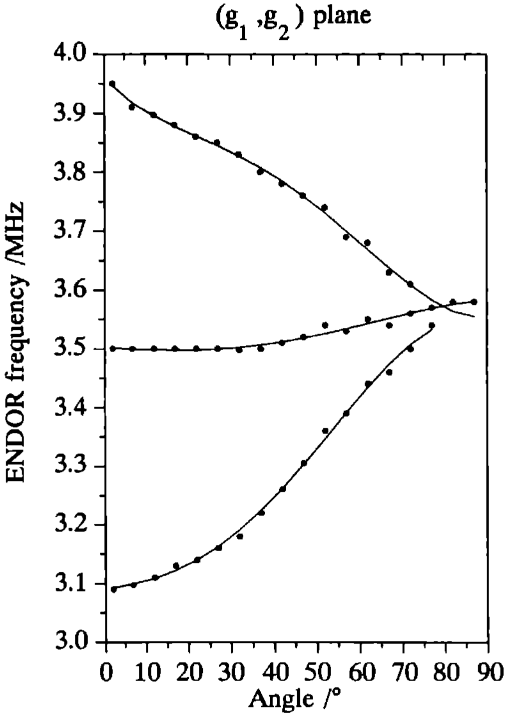

Figure 5.8
Angular dependence of the ^{23}Na ENDOR transitions having the highest signal intensity in the (g_1, g_2) plane. At an angle of 0° $\vec{B}_0$ is parallel to the g_2 axis; $\vec{B}_0$ is parallel to the g_1 axis at an angle of 90°. These transitions belong to the same m_s manifold.

5.4 Discussion

In this section the various tensors determined are discussed in terms of symmetry and bonding properties and the data obtained are also compared to those recently reported for KCl:Fe(CN)$_6^{3-}$ [13].

The principal values of A^N, Q^N, A^C, A^{Na} and Q^{Na} and their angles with respect to the g tensor axes are summarised in table 5.1: figure 5.4 illustrates the directions of the principal axes of the tensors in the 'molecular' frame. For all tensors two axes are found to lie in the (g_1, g_2) plane.

According to the angular dependence of their ENDOR transitions the equatorial ^{14}N and ^{13}C nuclei form two magnetically equivalent pairs. Also, the two ^{23}Na nuclei in the (g_1, g_2) plane and the axial ^{13}C nuclei are magnetically equivalent. This indicates the presence of three mirror planes (the planes spanned by g_1,g_3 and g_2,g_3 as well as the (g_1, g_2) plane) and confirms the orthorhombic symmetry of the centre under study. The C_{2v} symmetry, which may be possible according to the EPR spectra [13,14], can therefore be ruled out.

From figure 5.4 it can be seen that the tensor components A_1^C(eq), A_1^N and Q_3^N are somewhat rotated away from the iron-cyanide bond vector of a perfect octahedron, making an average angle of ca 37° with the g_2 axis instead of 45°. For the cyanide ligands which are characterised by a strong triple bond, the coupling tensors A^C, A^N and Q^N should have one common principal axis along the cyanide triple bond vector. Therefore, the deviation of the directions of A_1^C, A_1^N and Q_3^N from the iron-cyanide bond vector indicates a small rotation of the cyanide ligands from the [010] direction, caused by the negatively charged cation vacancies. This proves that the vacancy-occupied axis is g_1. According to the ^{23}Na ENDOR spectra the maximum component A^{Na}, A_2^{Na}, is found to lie parallel to g_2. This agrees with the fact that the lobes of the Fe 3d function, which mainly participates to the molecular orbital of the unpaired electron, lie along the g_1,g_2 axes, and it confirms also the location of the vacancies on the $(\pm)g_1$ axis.

$Fe(CN)_6^{3-}$ is the classical example of a typical low spin complex. Owing to the strong octahedral ligand field the t_{2g} and e_g states are well separated, resulting in a $3d^5$ $(S=\frac{1}{2})$ configuration which is commonly treated as a positive hole in the filled t_{2g} subshell [9,10]. The combined action of a low-symmetry ligand-field component and the spin-orbit interaction produces three Kramers doublets. According to a ligand-field calculation made for $Fe(CN)_6^{3-}$ incorporated in KCl [13] and NaCl [14] the splitting between the t_{2g} states amounts to a few hundred cm^{-1}. The three d orbitals d_{xz}, d_{yz} and d_{xy} (using the crystallographic axes) are mixed noticeable; the wavefunction describing the unpaired electron (ψ_0) for centre I_a in KCl, has approximately 71.7% d_{xy}, 20.1% d_{xz} and 8.2% d_{yz} character [13].

The observed ^{13}C , ^{14}N and ^{23}Na hyperfine splittings are quite large and indicate a considerable delocalisation of the unpaired electron. It is noteworthy that the axial ^{13}C hyperfine coupling constants are of the same magnitude as the equatorial ones. This is unexpected because the wavefunction has predominantly d_{xy} character. We believe that the coupling of the axial carbon atoms are influenced to a large extent by spin polarisation. To confirm this triple resonance experiments for the determination of the sign of the ^{13}C coupling constants are planned in our laboratory. Awaiting these results we abandon a detailed discussion of the various coupling constants in terms of spin densities. It is interesting to compare some of our results with results obtained by Daul et al [27]. These authors studied $Cs_2KFe(CN)_6$ with the aid of polarised neutron diffraction experiments. They found for the spin density distribution in the t_{2g} orbitals:

$$d_{xy}^{-0.61}\, d_{xy}^{0.78}\, d_{yz}^{0.72}\, d_{z^2}^{0.06}\, d_{x^2\ y^2}^{0.17}.$$

Thus the spin is mainly in the d_{xz} and d_{yz} orbitals, whereas d_{xy} and d_{z^2} contain considerable amounts of negative spin. For the complex studied by us the spin is mainly in the d_{xy} orbital. This result shows the large effect the vacancies have on the spin-density distribution in the ferricyanide ion. The spin hole in the d_{xy} orbital is stabilised by the negatively charged vacancies on the x axis. A study of the system $K_3Co(CN)_6$ doped with Fe^{3+} should reveal more clearly the effect of the vacancies on the spin density distribution since in this system no charge-compensating vacancies are present (see chapter 8. For the equatorial ^{14}N nuclei a pronounced quadrupole interaction is observed. Since nuclear quadrupole couplings in molecules are in general only qualitatively understood, and most of the attempts to calculate the electric field gradients were not particularly successful, we use the model originally proposed by Townes and Daily (abbreviated TD) [28] for the interpretation of our results. According to TD the observed quadrupole parameters are related to the electron population of an atom. The TD approach simply assumes that the electron field gradient on a nucleus is due to different populations of the three p orbitals $2p_x$, $2p_y$ and $2p_z$. Multicentre electronic and lattice contributions are neglected. The model yields the following relations between the experimental coupling constant $(e^2qQ/h)_{mol}$ and the population numbers N_j (p_z points to the metal):

$$\begin{aligned} f &= \frac{(e^2qQ/h)_{mol}}{(e^2qQ/h)_{at}} = -N_z + \frac{N_x + N_y}{2} \\ \text{and } f \cdot \eta &= \frac{3(N_x - N_y)}{2}. \end{aligned} \tag{5.4}$$

Where $(e^2qQ/h)_{at}$ is the experimentally determined value for the free atom [29]. s Electrons do not contribute because of the spherical symmetry.

Using the experimental Q_3^N value 5.1 yields $(e^2qQ/h)_{mol} = 3.84$ MHz. With $(e^2qQ/h)_{at} \approx (-)10$ MHz [29] one obtains f = 0.384. This means that the difference in population between the population in the N $2p_z$ and the average population in the N $2p_x$ and $2p_y$ orbitals amounts to 38%. The population difference (N_x - N_y) between the N $2p_x$ and $2p_y$ orbitals can now be estimated to be ca 0.09 (using equation 5.4 and $\eta = 0.36$). The values found are very typical for a ^{14}N nucleus in a cyanide group. From nuclear quadrupole resonance studies [30] on ^{14}N in the cyanide groups of cyano complexes f values in the range f = 0.35-0.42 have been derived.

Finally, a comparison of the data regarding NaCl:$Fe(CN)_6^{3-}$ with those reported for $Fe(CN)_6^{3-}$ in KCl [13] should be made. The ratio of the lattice constants of NaCl (564 pm) and KCl (629 pm) is 0.90. From this, considering the closer packing in the NaCl crystal, an enlarged influence of the negatively charged cation vacancies can be expected resulting in an increased rotation of the ^{13}C and ^{14}N tensor components towards the iron sodium direction. However, this has not been observed, the rotation of the tensor axes of the tensor axes of the equatorial N and C atoms in both systems is similar. Also the principal values of the various tensors do not differ much.

In contrast to the NaCl system for which ^{23}Na ENDOR transitions are observed no ENDOR transitions belonging to the ^{39}K nuclei could be detected for the system KCl:$Fe(CN)_6^{3-}$. This, however, can be understood by considering the magnetic moment of ^{39}K which is ca. five times smaller than that of ^{23}Na .

5.5 Conclusions

The ENDOR spectra of $Fe(CN)_6^{3-}$ in NaCl allowed a detailed analysis of the ligand hyperfine (A_{eq}^N, $A_{eq,ax}^C$, A^{Na}) and nuclear quadrupole tensors (Q^N, Q^{Na}).

The equatorial cyanide groups are rotated 6-8° away from their ideal octahedral positions due to the influence of the negatively charged cation vacancies. This fact and the directions of the principal axes of the ^{23}Na hyperfine and quadrupole tensor confirm the positions of the two vacancies in the centre studied.

The ligand hyperfine coupling point to a noticeable delocalisation of the unpaired electron to ligand nuclei, indicating strong covalent interactions in the $Fe(CN)_6^{3-}$ complex unit. The ^{13}C couplings of the axial ^{13}C nuclei are unexpectedly large, suggesting a significant contribution of the spin-polarisation. It is hoped that together with triple resonance experiments and MO calculations a complete picture of the spin density distribution will be reached. A simple relation between the data for NaCl:$Fe(CN)_6^{3-}$ and KCl:$Fe(CN)_6^{3-}$, which can be expected from the ratio of the lattice constants of both systems, has not been found.

We express our gratitude to S.M. Meijers for growing the crystals and to D. Heinhold for his assistance in the EPR and ENDOR measurements. We also acknowledge helpful discussions with Dr. D.M. Wang.

References

[1] Jorgensen, C.K., 1962, *Absorption spectra and Chemical Bonding in Complexes*, (Pergamon Press, Oxford).

[2] Schläfer, H.L. and Gliemann, G., 1967, *Einfhürung in die Ligandenfeldtheorie*, (Akademische Verslagsgesellschaft Geest & Portig, Leipzig).

[3] Kuska, H.A. and Rogers, M.T., 1965, *J. Chem. Phys.*, **42**, 3034.

[4] Vugman, N.V., Muniz, R.P.A. and Danon, J., 1972, *J. Chem. Phys.*, **57**, 1297.

[5] Symon, M.C.R., and Wilkinson, J.G., 1972, *J. Chem. Soc., Dalton Trans.*, 1086.

[6] Jain, S.C., Reddy, K.V. and Reddy, T.Rs., 1975, *J. Chem. Phys.*, **62**, 4366.

[7] Kasi Vinwanath, A. and Rogers, M.T., 1981, *J. Chem. Phys.*, **75**, 4183.

[8] Vugman, N.V. and Pinhal, N.M., 1983, *Mol. Phys.*, **49**, 1315.

[9] Baker, J.M., Bleaney, B. and Bowers, K.D., 1956, *Proc. Phys. Soc. B.*, **69**, 1205.

[10] Bleaney, B. and O'Brien, M.C.M., 1956, *Proc. Phys. Soc. B.*, **69**, 1216.

[11] Wang, D.M., and de Boer, E., 1989, *Phys. Rev. B.*, **39**, 11272.

[12] Wang, D.M. and Pilbrow, J.R., 1988, *J. Magn. Res.*, **77**, 411.

[13] Wang, D.M. and de Boer, E., 1990, *J. Chem. Phys.*, **92**, 4698.

[14] Wang, D.M., Meijers, S.M. and de Boer, E., 1990, *Mol. Phys.*, **70**, 1135.

[15] Böttcher, R., Heinhold, D. and Windsch, W., 1985, *Chem. Phys.*, **93**, 339.

[16] Keijzers, C.P., Reijerse, E.J., Stam, P., Dumont, M.F. and Gribnau, M.C.M., 1987, *J. Chem. Soc., Faraday Trans. 1*, **83**, 3493.

[17] Reijerse, E.J., Paulissen, M.L.H. and Keijzers, C.P., 1984, *J. Magn. Res.*, **60**, 66.

[18] Böttcher, R., Kirmse, R., Stach, J., Reijerse, E.J. and Keijzers, C.P., 1986, *Chem. Phys.*, **107**, 145.

[19] Reijerse, E.J. van Aerle, N.A.J.M., Keijzers, C.P., Böttcher, R., Kirmse, R. and Stach, J., 1986, *J. Magn. Reson.*, **67**, 114.

[20] Kirmse, R., Stach, J., Abram, U., Dietzsch, W., Böttcher, R., Gribnau, M.C.M. and Keijzers, C.P., 1984, *Inorg. Chem.*, **23**, 3333.

[21] Böttcher, R., Kirmse, R., Stach, J. and Keijzers, C.P., 1985, *Mol. Phys.*, **55**, 1431.

[22] Stach, J., Kirmse, R., Sieler, J., Abram, U., Dietzsch, W., Böttcher, R., Hansen, L.K., Vergoossen, H., Gribnau, M.C.M. and Keijzers, C.P., 1986, *Inorg. Chem.*, **25**, 1369.

[23] Geschwind, S., 1967, *Hyperfine Interactions, ed. A.J. Freeman and R.B. Frankel*, (Academic Press, New York).

[24] Schweiger, A. and Günthard, H., 1978, *Chem. Phys.*, **32**, 35.

[25] Schweiger, A., 1982, *Stuct. Bonding (Berlin)*, **51**, 1.

[26] Köhler, K., Kirmse, R., Böttcher, R., Abram, U., Gribnau, M.C.M., Keijzers, C.P. and

de Boer, E., 1990, *Chem. Phys.*, **143**, 83.

[27] Daul, C.A., Day, P., Figgis, B.N., Gudel, H.U., Herren, F., Lupi, A. and Reynolds, P.A.,

1988, *Proc. R. Soc. London Ser. A*, **419**, 205.

[28] Townes, C.H. and Dailey, B.P., 1949, *J. Chem. Phys.*, **17**, 782.

[29] Lucken, E.A.C., 1969 *Nuclear Quadrupole Coupling Constants*, Academic Press, New York.

[30] Guibe, L., 1972, *Top. Curr. Chem.*, **30**, 77.

Chapter 6

Triple resonance on $Fe(CN)_6^{3-}$ doped into NaCl

Chapter 5 reported about the results of an ENDOR study performed on $Fe(CN)_6^{3-}$ doped into NaCl [1]. The hyperfine and quadrupole coupling constants of ^{13}C , ^{14}N and ^{23}Na were reported. However, the sign(s) of these coupling constants could not be determined. One of the remarks made in the previous chapter was: "...It is noteworthy that the axial ^{13}C hyperfine coupling constants are of the same magnitude as the equatorial ones. This is unexpected because the wavefunction has predominantly d_{xy} character. We believe that the coupling of the axial carbon atoms are influenced to a large extent by spin polarisation. To confirm this, triple resonance experiments for the determination of the sign of the ^{13}C coupling constants are planned...". Therefore, the results of triple resonance experiments will be described in this chapter.

6.1 Experimental

The experimental triple set-up has been described in detail in chapter 3, while a description about the resonator used for these experiments can be found in chapter 4 [2]. As in the experiment described by Kirmse et al.[1], the orthorhombic centre I_a has been selected for the triple resonance investigation. Again, ENDOR transitions due to ^{13}C , ^{14}N and ^{23}Na could be observed. Like the ENDOR spectra, the triple resonance spectra were measured at a temperature of 4.2 K, employing a bath cryostat. The spectra were recorded at some orientations in the (g_1, g_2) plane. The comparison between the results described in the previous chapter and in this chapter is facilitated because the experimental measurement conditions are similar. An important difference between the experiments described in this chapter and the experiments described by Kirmse et al. is that a 'physically' different crystal has been used i.e. the exact dope concentration, the shape and size of the single crystal used for the triple experiments is (slightly) different from that of the single crystal used for the ENDOR experiments. The result is that the signal to noise ratio (S/N) visible in the spectra displayed in this chapter, is worse than the S/N of the spectra displayed in chapter 5. As a consequence, the low frequency ^{13}C signals are not detectable in the spectra shown in this chapter.

The microwave power needed to saturate the EPR transition was 1.1 mW. The RF power of the swept frequency amounted 32 W, while the power of the fixed RF frequency was 42 W.

6.2 Results

^{14}N and ^{23}Na spectra

General triple measurements have been performed on NaCl:Fe(CN)$_6^{3-}$. Figure 6.1a shows an ordinary ENDOR spectrum, while figure 6.1b shows a triple spectrum. Comparison of these figures reveals the effects of general triple resonance on the signal intensity of the ^{23}Na and ^{14}N ENDOR lines. The fixed triple resonance frequency has been set on one of the ^{23}Na lines, indicated by the arrow in figure 6.1b. Köhler et al. [3] calculated the

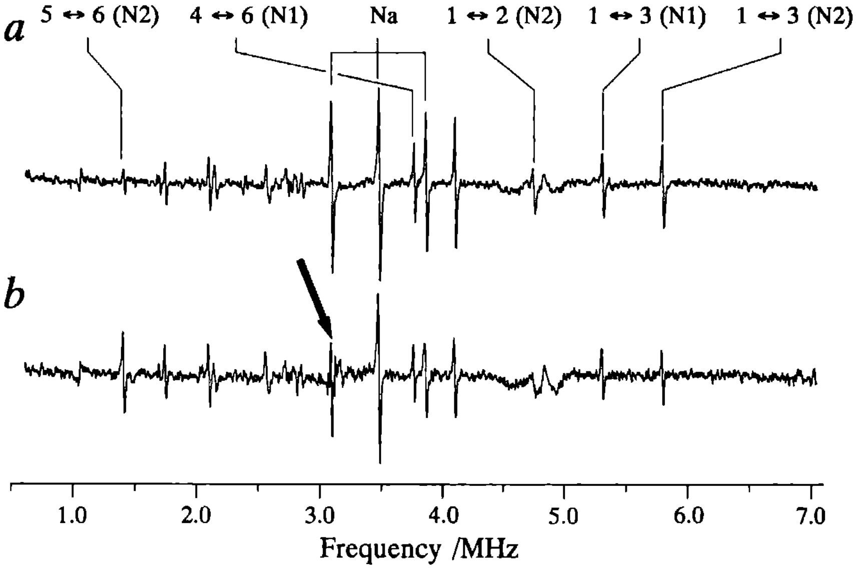

Figure 6.1
The effect of general triple resonance. The displayed spectra have been recorded in the (g_1, g_2) *plane, 15° from the* g_2 *axis.*
The microwave frequency was 9.28076 GHz.
a A normal ENDOR spectrum; some transitions have been indicated. The arrow marks the ENDOR signal which frequency value has been taken for the fixed triple frequency.
b A triple resonance spectrum, microwave and RF powers are equal to those used to record the spectrum shown in figure 'a'. Clearly visible is that several signals belonging to one m_s *manifold have decreased in intensity compared to the corresponding ones in the upper figure, while some signals belonging to the other* m_s *manifold show an increase in signal intensity.*

frequencies and intensities of the ENDOR lines for a system having S = $\frac{1}{2}$ and I = $\frac{3}{2}$ in case the hyperfine tensor is anisotropic. They found that the ENDOR lines having the highest intensities, belong to the high frequency NMR transitions. Therefore, the ^{23}Na lines having the highest intensities in figure 6.1, belong to the high frequency NMR transitions of this atom. The low frequency NMR transitions of ^{23}Na are not visible, neither in figure 6.1a (showing the ordinary ENDOR spectrum) nor in figure 6.1b (showing the general triple resonance spectrum). Figure 6.1b clearly demonstrates that e.g. the 1 ↔ 3 transitions of nitrogen atoms N1 and N2 decrease in signal intensity compared to the ordinary ENDOR spectrum, while the e.g. 5 ↔ 6 transition of N2 increases in intensity compared to the ordinary ENDOR spectrum. The figure also shows that all ^{23}Na signals decrease in intensity as well. Contrary to expectations, the transition 4↔6 (N1) does not show an increase in signal intensity, as can be seen in figure 6.1b: its intensity remains the same.

The fixed RF frequency has also been set on the 4↔6 N2 transition (not shown). As was expected, the signal intensity of the lines which show a decrease in intensity in figure 6.1b, now show a (slight) intensity increase. The lines belonging to the other spin manifold were completely buried in the noise.

^{13}C spectra

Figures 6.2a and 6.2b show the effects of general triple resonance on the signal intensity of ^{13}C ENDOR lines. The fixed triple resonance frequency has been set again on the same ^{23}Na line, indicated by the arrow in figure 6.1b. The low frequency ^{13}C lines are unfortunately not detectable in the ordinary ENDOR spectrum. The triple resonance spectrum (figure 6.2b) clearly shows a decrease in signal intensity of all high frequency ^{13}C lines. One would expect that the low frequency ^{13}C lines show an increase in signal intensity in the triple spectrum. However, even in the triple resonance spectrum, the low frequency ^{13}C lines could not be discerned.

6.3 Discussion

It can be concluded from the decrease in line intensity of the 1 ↔ 3 and 1 ↔ 2 transitions, that these transitions belong to the same m_s manifold as the high frequency ^{23}Na lines. Therefore, the hyperfine coupling constants for both nitrogen atoms have equal signs, as was to be expected. Since the intensities of high frequency ^{23}Na transitions diminish, the sign of the ^{23}Na hyperfine coupling constants must be equal to the signs of the ^{14}N hyperfine coupling constants.

The dipolar operator, $\mathcal{H}_{dd}$, for interaction between an electron spin and a nuclear spin can be written as [4]:

$$\mathcal{H}_{dd} = g_e\,\beta_e\,g_n\,\beta_n\,\frac{1}{r^3}\left(\frac{3\left(\vec{r}\cdot\vec{S}\right)\left(\vec{r}\cdot\vec{I}\right)}{r^2} - \vec{I}\cdot\vec{S}\right).$$

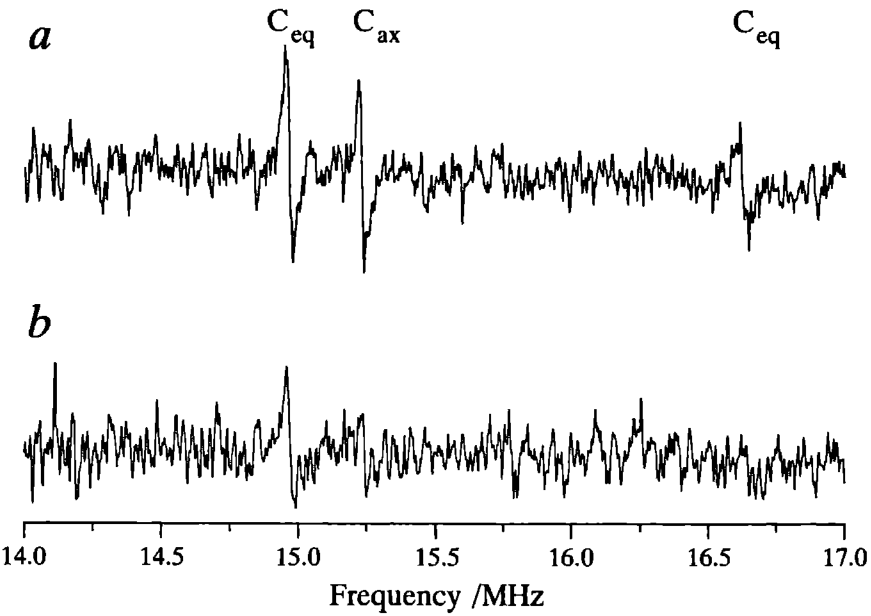

Figure 6.2
The effect of general triple resonance. The displayed spectra have been recorded in the (g_1, g_2) *plane, 15° from the* g_2 *axis.*
The microwave frequency was 9.28076 GHz
a An ordinary ^{13}C *ENDOR spectrum.*
b A triple resonance spectrum, microwave and RF powers are equal to those used to record the spectrum shown in figure 'a'. It is evident that all high frequency ^{13}C *signals have decreased in intensity compared to the corresponding ones in the upper figure.*

Therefore, the contribution of $\mathcal{H}_{dd}$ to the anisotropic hyperfine interaction tensor ($\overline{\overline{\mathrm{T}}}$) is given by:

$$\overline{\overline{\mathrm{T}}} = \langle\psi|\mathcal{H}_{dd}|\psi\rangle .$$

where ψ denotes the wavefunction describing the unpaired electron. This wavefunction for centre I_a in KCl, has approximately 71.7% d_{xy}, 20.1% d_{xz} and 8.2% d_{yz} character [5] (using the crystallographic axes) i.e.:

$$\begin{aligned} |\psi\rangle &= \sqrt{0.717}\,|d_{xy}\rangle + \sqrt{0.201}\,|d_{xz}\rangle + \sqrt{0.082}\,|d_{yz}\rangle \\ &\equiv \sum_{\substack{i,j=x,y,z \\ i>j}} c_{ij}|d_{ij}\rangle \end{aligned}$$

where: $c_{xy} = \sqrt{0.717}$, $c_{xz} = \sqrt{0.201}$ and $c_{yz} = \sqrt{0.082}$.

Therefore, to a first approximation, the anisotropic part of the hyperfine tensor is given by:

$$\overline{\overline{\mathrm{T}}} = g_e\,\beta_e\,g_n\,\beta_n \sum_{\substack{i,j,k,l=x,y,z\\ i>j\,,\,k>l}} c_{ij}\,c_{kl}\,\langle d_{ij}|\mathcal{H}_{dd}|d_{kl}\rangle\,.$$

The spherical components of these wavefunctions can be expressed in terms of linear combinations of the spherical harmonic functions $Y_{l,m}$ (in this particular case: $l = 2$, $m = 0, \pm 1, \pm 2$), yielding:

$$\begin{aligned}
T_{xx} &= g_e\,\beta_e\,g_n\,\beta_n \left(\frac{2}{7}\,c_{xy}^2 + \frac{2}{7}\,c_{xz}^2 - \frac{4}{7}\,c_{yz}^2\right)\left\langle\frac{1}{r^3}\right\rangle \\
&= 0.215\,g_e\,\beta_e\,g_n\,\beta_n\left\langle\frac{1}{r^3}\right\rangle \\
T_{yy} &= g_e\,\beta_e\,g_n\,\beta_n \left(\frac{2}{7}\,c_{xy}^2 - \frac{4}{7}\,c_{xz}^2 + \frac{2}{7}\,c_{yz}^2\right)\left\langle\frac{1}{r^3}\right\rangle \\
&= 0.113\,g_e\,\beta_e\,g_n\,\beta_n\left\langle\frac{1}{r^3}\right\rangle \\
T_{zz} &= g_e\,\beta_e\,g_n\,\beta_n \left(-\frac{4}{7}\,c_{xy}^2 + \frac{2}{7}\,c_{xz}^2 + \frac{2}{7}\,c_{yz}^2\right)\left\langle\frac{1}{r^3}\right\rangle \\
&= -0.329\,g_e\,\beta_e\,g_n\,\beta_n\left\langle\frac{1}{r^3}\right\rangle \\
T_{yx} = T_{xy} &= g_e\,\beta_e\,g_n\,\beta_n\,\frac{2}{7}\,c_{xz}\,c_{yz}\left\langle\frac{1}{r^3}\right\rangle \\
&= 0.037\,g_e\,\beta_e\,g_n\,\beta_n\left\langle\frac{1}{r^3}\right\rangle \\
T_{zy} = T_{yz} &= g_e\,\beta_e\,g_n\,\beta_n\,\frac{2}{7}\,c_{xy}\,c_{xz}\left\langle\frac{1}{r^3}\right\rangle \\
&= 0.108\,g_e\,\beta_e\,g_n\,\beta_n\left\langle\frac{1}{r^3}\right\rangle \\
T_{zx} = T_{xz} &= g_e\,\beta_e\,g_n\,\beta_n\,\frac{2}{7}\,c_{xy}\,c_{yz}\left\langle\frac{1}{r^3}\right\rangle \\
&= 0.069\,g_e\,\beta_e\,g_n\,\beta_n\left\langle\frac{1}{r^3}\right\rangle
\end{aligned}$$

where $\left\langle\frac{1}{r^3}\right\rangle$ denotes the interaction of the radial part of the dipolar interaction, with the radial part of the wavefunctions.

Because the calculated off-diagonal elements are not small enough compared to the diagonal elements, they cannot be neglected: the tensor has to be diagonalised. The principal values of the calculated diagonalised tensor $\overline{\overline{\mathrm{T}}}'$, are (with respect to the x',y',z' axes):

$$\begin{aligned}
T'_{x'x'} &= 0.246\,g_e\,\beta_e\,g_n\,\beta_n\left\langle\frac{1}{r^3}\right\rangle \\
T'_{y'y'} &= 0.113\,g_e\,\beta_e\,g_n\,\beta_n\left\langle\frac{1}{r^3}\right\rangle \\
T'_{z'z'} &= -0.360\,g_e\,\beta_e\,g_n\,\beta_n\left\langle\frac{1}{r^3}\right\rangle .
\end{aligned}$$

Thus, the calculated $T'_{x'x'}$ and $T'_{y'y'}$ components are positive, while the calculated $T'_{z'z'}$ component is negative. If the signs in table 5.1 (chapter 5) are correct, then the isotropic hyperfine value for the nitrogen atoms is positive. This means that the principal components of the anisotropic part of the hyperfine coupling tensor are given by (in units of 10^{-4} cm^{-1}): T_{xx} = 1.29, T_{yy} = 0.52 and T_{zz} = -1.81. In table 6.1 the ratios of the measured anisotropic hyperfine components and the ratios of the first order calculated components are listed. On comparing them it can be concluded that the signs agree with each other and that the numerical values in fair correspondence. It can also be concluded that the equal signs of the hyperfine components of ^{23}Na and ^{14}N agree with the calculated signs, see table 5.1 (chapter 5). Thus, the isotropic hyperfine values for both ^{23}Na and ^{14}N are positive. Therefore, it can be deduced that the high frequency NMR transitions of ^{23}Na and thus the 1 ↔ 3, 1 ↔ 2 and 2 ↔ 3 ^{14}N transitions, belong to the $m_s = -\frac{1}{2}$ manifold.

Table 6.1
The ratios of the measured anisotropic components and the ratios of the calculated anisotropic components for the nitrogen hyperfine tensor.

	Experimental	Theoretical
T_{xx} / T_{yy}	2.48	2.18
T_{zz} / T_{yy}	-3.48	-3.19
T_{xx} / T_{zz}	-0.71	-0.68

In the calculations of the anisotropic hyperfine components a number of approximations has been made: higher order contributions to the hyperfine tensor have been omitted, it is assumed that the wavefunction describing the unpaired electron for centre I_a in NaCl is equal to that in KCl, and the small angle the e.g. A_1^N component makes with the crystallographic y axis has been neglected. In order to avoid these approximations, we are currently involved in theoretical calculations which will result in, among others, a more reliable theoretical description of the hyperfine tensors [6].

It has been remarked in the preceding paragraph that some signals which belong to the $m_s = +\frac{1}{2}$ manifold (e.g. the 4↔6 transition) do not show an increased signal intensity in case an NMR transition belonging to the $m_s = -\frac{1}{2}$ manifold is excited by means of the fixed RF frequency. Thus, it can be deduced that the additional relaxation path created by the fixed RF frequency in this particular triple resonance experiment, does not increase the efficiency of the relaxation. Therefore, the conclusion can be drawn that the cross-relaxation time, T_x, is equal or even smaller than the electron spin relaxation time, T_{1e}.

From figure 6.2b it can be deduced that all high frequency ^{13}C signals belong to the same m_s manifold as the high frequency ^{23}Na lines and the 1 ↔ 3, 1 ↔ 2 and 2 ↔ 3 nitrogen transitions: they all belong to the $m_s = -\frac{1}{2}$ manifold.

A discussion of the signs for the calculated and measured anisotropic parts of the ^{13}C hyperfine tensors, like is done for ^{14}N, cannot be carried out, because only two of the three principal hyperfine components for ^{13}C could be resolved experimentally [1]. Therefore, the anisotropic parts of the hyperfine tensors cannot be determined.

The question of the large hyperfine splitting of the axial ^{13}C atom still remains unanswered. We are, however, currently involved in theoretical studies [6], which can elucidate this problem.

6.4 Conclusions

From the general triple experiment it can be deduced that the signs of the hyperfine coupling constants of all ^{13}C , ^{14}N and ^{23}Na atoms are equal. According to the first order calculations described in the former paragraph, the signs of the hyperfine coupling constants listed in table 5.1 (chapter 5) are correct, i.e. all hyperfine coupling constants are positive. Consequently, all high frequency ^{13}C transitions belong to the $m_s = -\frac{1}{2}$ manifold.

For the experimental conditions described in this chapter, the following relation can be deduced between the cross-relaxation time, T_x, and the electron spin relaxation time, T_{1e}: $T_x \leq T_{1e}$.

References

[1] Kirmse, R., Böttcher, R., Willems, J.-P., Reijerse, E.J. and de Boer, E., 1991, *J. Chem. Soc. Faraday Trans.*, **87**, 3105.

[2] Willems, J.-P., Klaassen, A.A.K., Reijerse,, E.J., Janssen, G.E. and de Boer, E., 1992, *Rev. Sci. Instrum.*, **63**(11), 5362

[3] Köhler, K., Kirmse, R., Böttcher, R., Abram, U., Gribnau, M.C.M, Keijzers, C.P., and de Boer, E., 1990, *Chem. Phys.*, **143**, 83.

[4] Atkins, P.W., 1983, *Molecular Quantum Mechanics, (second edition)*, (Oxford University Press, Oxford)

[5] Wang, D.M. and de Boer, E., 1990, *J. Chem. Phys.*, **92**, 4698.

[6] Sommerdijk, H.T. and van der Avoird, A, *To be published.*

Chapter 7

EPR measurements on $K_3Co(CN)_6$ doped with $K_3Fe(CN)_6$

a determination of the polytype crystal structure of $K_3Co(CN)_6$ [1]

In this chapter it will be shown that with EPR the polytype structure of $K_3Co(CN)_6$ single crystals doped with $Fe(CN)_6^{3-}$, can be determined easily. The number of resonance lines for an arbitrary orientation of the magnetic field is indicative for the type of crystal studied. This is substantiated by the known crystallographic data concerning $K_3Co(CN)_6$.

7.1 Introduction

Before 1961 a confused situation existed in the literature with respect to the crystallographic parameters of $K_3Co(CN)_6$ [1,2]. Kohn and Townes [3] showed that $K_3Co(CN)_6$ displays polytypism. They reported the existence of 1M (one-layer monoclinic), 2Or (two-layer orthorhombic), 3M (three-layer monoclinic) and 7M (seven-layer monoclinic, see appendix A) structures. A 4Or (four-layer orthorhombic) structure of $K_3Co(CN)_6$ was found by Reynhardt and Boeyens [4] in 1972. The 2Or, 3M, 7M and 4Or structure types, are related by stacking of (100) one-layer monoclinic lamellae. In figure 7.1 this has been illustrated for the 2Or and 3M structures. The work of Kohn and Townes [3] and the work of Reynhardt and Boeyens [4] show that the number of atoms in the unit cell (Z), is directly related to the shape and size of the unit cell of the particular structure. This has been exemplified for the 1M, the 2Or and the 3M structure types in table 7.1.

Usually, a crystal structure is determined by means of an X-ray diffraction study. In the situation of polytypism, it may well be possible that, in the reciprocal space, a super-structure (such as the 1M structure) is found instead of a the real structure. The intensities of the reflections caused by the stacking of the 1M units can be low; therefore, these reflections may be overlooked easily. In this paper it will be shown that, in such a situation, the EPR spectra directly reveal the type of crystal structure.

In our study, we doped diamagnetic crystal of $K_3Co(CN)_6$ with the paramagnetic compound $Fe(CN)_6^{3-}$. In this way, the polytypism of $K_3Co(CN)_6$ can be studied by measuring the EPR spectrum of the paramagnetic 'spin label' $Fe(CN)_6^{3-}$. The determination of the

---

[1] Except for appendix B, the contents of this chapter has been published in J. Mol. Phys. **80**, March 1993, pages 607 to 623, by J.-P. Willems, M.P.J.W. Clephas and E. de Boer

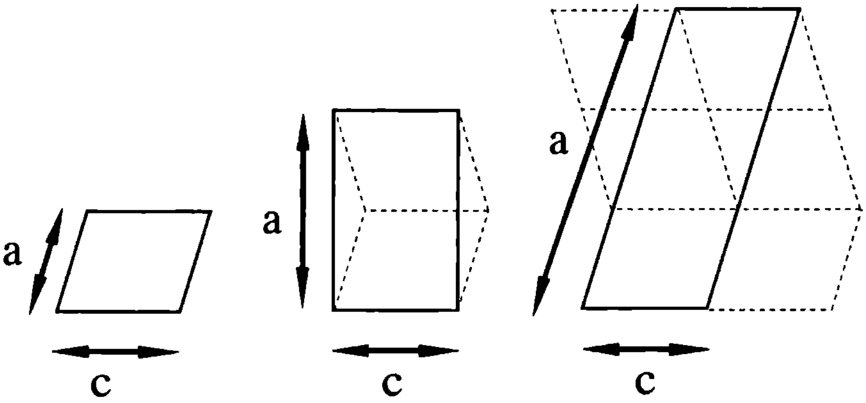

Figure 7.1
Relation between the projections along the b axis of the unit cells of the 1M (left), the 2Or (centre) and the 3M (right) crystal structures. The stacking of the 1M like unit cells is given by dashed lines.

g tensors of the various sites in the crystal enables us to verify the stacking mechanism proposed by Kohn and Townes [3].

In 1956, Baker et al.[5] already performed EPR measurements on a crystal of $K_3Co(CN)_6$ doped with $Fe(CN)_6^{3-}$. They reported the principal values and the direction of the g tensors of two sites. We now believe that Baker et al.[5] measured a crystal having an 1M structure. At that time, however, they were not aware of the fact that $K_3Co(CN)_6$ exhibits polytypism.

7.2 Experimental

The crystals were grown by the following procedure. To a 40 ml (0.03 M) solution of $K_3Co(CN)_6$ (Aldrich) in water, $K_3Fe(CN)_6$ (Merck) was added, such that its concentra-

Table 7.1
Unit cell parameters for the 1M, 2Or and 3M structure types as established by Kohn and Townes [3]

	1M	2Or	3M
a/Å	7.00 ± 0.02	13.31 ±0.01	21.00 ± 0.06
b/Å	10.38 ± 0.01	10.37 ± 0.01	10.38 ± 0.01
c/Å	8.37 ± 0.02	8.35 ± 0.01	8.37 ± 0.02
$\beta/°$	107.19 ± 0.03	-	107.19 ± 0.03
Z	2	4	6
Space group	$P2_1/c$	Pnca	$P2_1/c$

tion in the final solution was 1 mol %. Placing this solution into a vacuum desiccator, double prismatic crystals were obtained after three weeks. The volume of the crystals is about 4 mm^3. From the morphology of the crystals, the crystal structure, monoclinic or orthorhombic, cannot be derived. The crystals contained 0.57 mol% Fe as determined by atomic absorption spectroscopy.

The $Fe(CN)_6^{3-}$ compound is a low spin ($S = \frac{1}{2}$) complex, which exhibits a large g anisotropy [6]. The EPR spectra can be described by the Hamiltonian:

$$\mathcal{H} = \beta_e \vec{B} \cdot \bar{\bar{g}} \cdot \vec{S}.$$

The measurements were performed using a standard Bruker ESP300 X-band spectrometer. The EPR spectra were taken at a sample temperature of 7 K in an Oxford CF200 flow cryostat. Measurements were made in the planes spanned by (g_1, g_2), (g_1, g_3) and (g_2, g_3). Recordings of the spectra were made at 3°-5° intervals. The insert used has been described elsewhere [7]. The data analysis was performed using the universal program package MAGRES [8].

7.3 Results and Discussion

The one-layer monoclinic structure (1M)

According to table 7.1, the 1M single crystal possesses two sites. This means that the EPR spectrum of this monoclinic crystal will exhibit two lines for an arbitrary orientation of the magnetic field and one line for the field parallel to the b axis and the (a,c) plane. Figure 7.2 shows the spectrum measured for $\vec{B}_0$ almost parallel to the g_2 tensor axis of site 1. Two resonance lines are observed with a linewidth of about 0.7 mT. The angular dependence of these two lines in three perpendicular planes (see experimental part) is shown in the figures 7.3a to 7.3c. From these figures it can be inferred that the g_3 axis (belonging to g min) lies almost parallel to one of the crystal axes. Consequently, only in figure 7.3c one notices twice coincidence of the resonance lines, i.e. for the directions of the magnetic field parallel to the crystal axes. Utilising the results of Baker et al.[5], it is possible to give the direction cosines of the g tensor axes with respect to the crystal axes. Analyzing our data yielded for the average principal g values for the two sites: $g_1 = 2.344 \pm 0.006$,

Table 7.2
Principal values of the g tensor and direction cosines of the g tensor axes with respect to the crystal axes for the one-layer monoclinic structure (1M).

	Site 1			Site 2		
	g_1	g_2	g_3	g_1	g_2	g_3
a*	-0.865	-0.502	-0.001	0.863	0.505	-0.001
b	0.501	-0.863	0.068	0.503	-0.862	0.068
c	0.028	0.062	-0.998	0.040	0.056	0.998
principal values	2.351	2.1040	0.898	2.338	2.1039	0.905

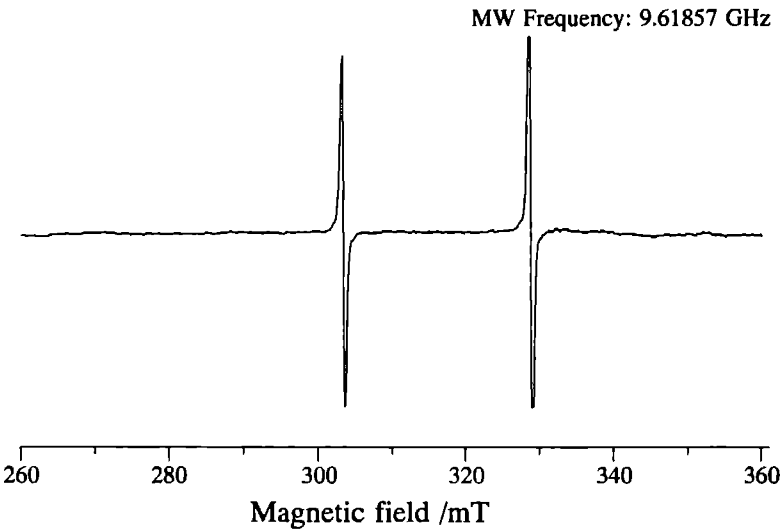

Figure 7.2
Typical EPR spectrum of the 1M crystal. This spectrum has been measured for $\vec{B}_0$ almost parallel to the g_2 axis of site 1.

$g_2 = 2.1039 \pm 0.0001$, $g_3 = 0.902 \pm 0.004$. The direction cosines of the principal g axes with respect to the crystal axes are given in table 7.2. It is noteworthy to remark that the g_3 axes of the two sites do not coincide and are also not parallel to the crystallographic c axis. This is clearly seen in the figures 7.3a and 7.3b, where the minima of the g curves of the two sites do not coincide. This observation is not supported by the work of Baker et al.[5], who found that the g_3 axes for both sites were parallel to the c axis of the crystal.

The two-layer orthorhombic structure (2Or)

Figure 7.4 shows an EPR spectrum of the 2Or crystal for $\vec{B}_0$ in an arbitrary direction. Four lines are observed, corresponding to the four sites present in the unit cell. This number of sites was to be expected considering table 7.1. The linewidth of the resonance lines is about 0.8 mT. An explanation of the different intensities of the lines will be given at the end of this section.

Figure 7.5 depicts the angular dependence of the four EPR lines in three orthogonal planes (see experimental part). In general one would expect, for arbitrary planes, three times collapsing of the resonance lines into two pairs. This does not occur in figure 7.5, because accidentally one of the g tensor axes (the g_3 axis in our case) lies parallel to a crystallographic axis (the c axis). One notices in figure 7.5c a collapsing of all lines into one, at an angle of about 65°, because at this direction the field is parallel to the b axis. Figures 7.5a and 7.5b show the amalgamation of the four resonance lines into two pairs.

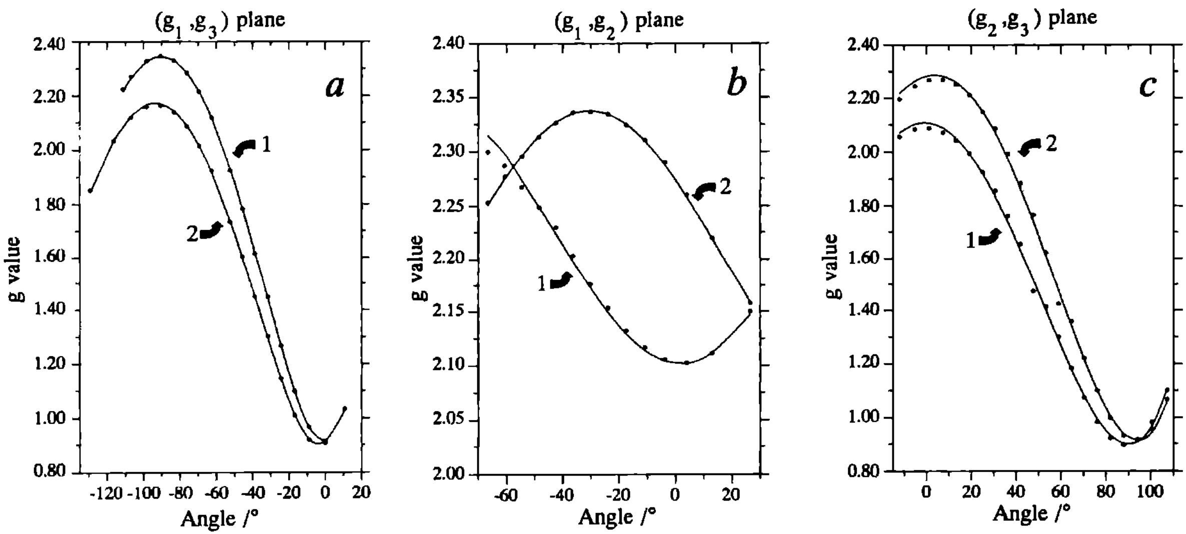

Figure 7.3
Angular dependence of the EPR lines in three perpendicular planes for the two sites in the 1M crystal. The dots represent the measured values, the lines are the fits. The numbering of the sites in this figure agrees with the numbering of the sites in table 7.2.
a: Angular dependence for $\vec{B}_0$ in the (g_1, g_3) plane of site 1. At an angle of 0°, the magnetic field is parallel to the g_3 axis of site 1; at an angle of -90°, the magnetic field is parallel to the g_1 axis of site 1.
b Angular dependence for $\vec{B}_0$ in the (g_1, g_2) plane of site 1. At an angle of 0°, the magnetic field is parallel to the g_2 axis of site 1.
c Angular dependence for $\vec{B}_0$ in the (g_1, g_3) plane of site 1. At an angle of 0°, the magnetic field is parallel to the g_2 axis of site 1; at an angle of 90°, the magnetic field is parallel to the g_3 axis of site 1.

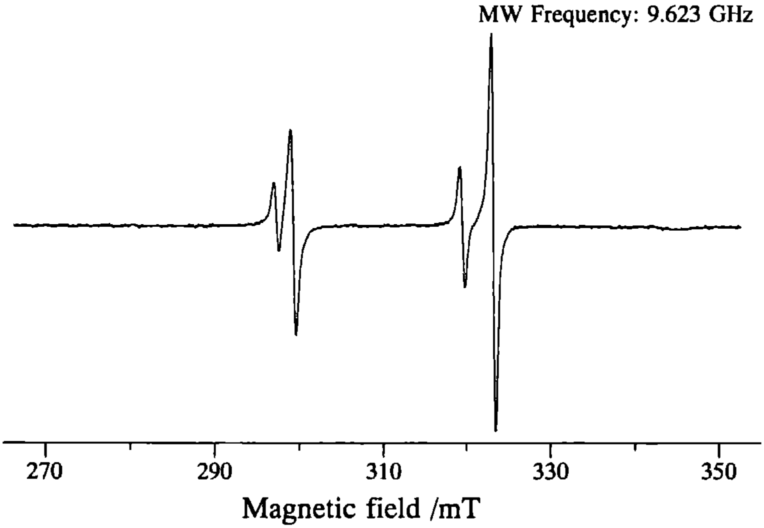

Figure 7.4
Typical EPR spectrum for the 2Or crystal. This spectrum has been measured for $\vec{B}_0$ in an arbitrary direction.

This occurs with the direction of the magnetic field parallel to the ab plane. The data were analyzed in the same way as pointed out for the 1M crystal.

The average principal g values were calculated as $g_1 = 2.352 \pm 0.006$ (sites 1 and 2), $g_1 = 2.41 \pm 0.01$ (sites 3 and 4), $g_2 = 2.114 \pm 0.009$ (for all sites) and $g_3 = 0.90 \pm 0.01$ (for

Table 7.3
Principal values of the g tensor and direction cosines of the g tensor axes with respect to the crystal axes for the two-layer orthorhombic structure (2Or).

	Site 1			Site 2		
	g_1	g_2	g_3	g_1	g_2	g_3
a	-0.878	-0.467	-0.103	-0.828	-0.550	0.106
b	0.474	-0.878	-0.060	0.558	-0.827	0.064
c	0.062	0.101	-0.993	-0.053	-0.113	-0.992
principal values	2.358	2.122	0.91	2.346	2.118	0.90

	Site 3			Site 4		
	g_1	g_2	g_3	g_1	g_2	g_3
a	0.839	0.533	0.113	0.856	0.508	-0.096
b	0.539	-0.841	-0.038	0.513	-0.857	0.037
c	-0.075	-0.093	0.993	0.064	0.081	0.995
principal values	2.40	2.118	0.90	2.42	2.099	0.87

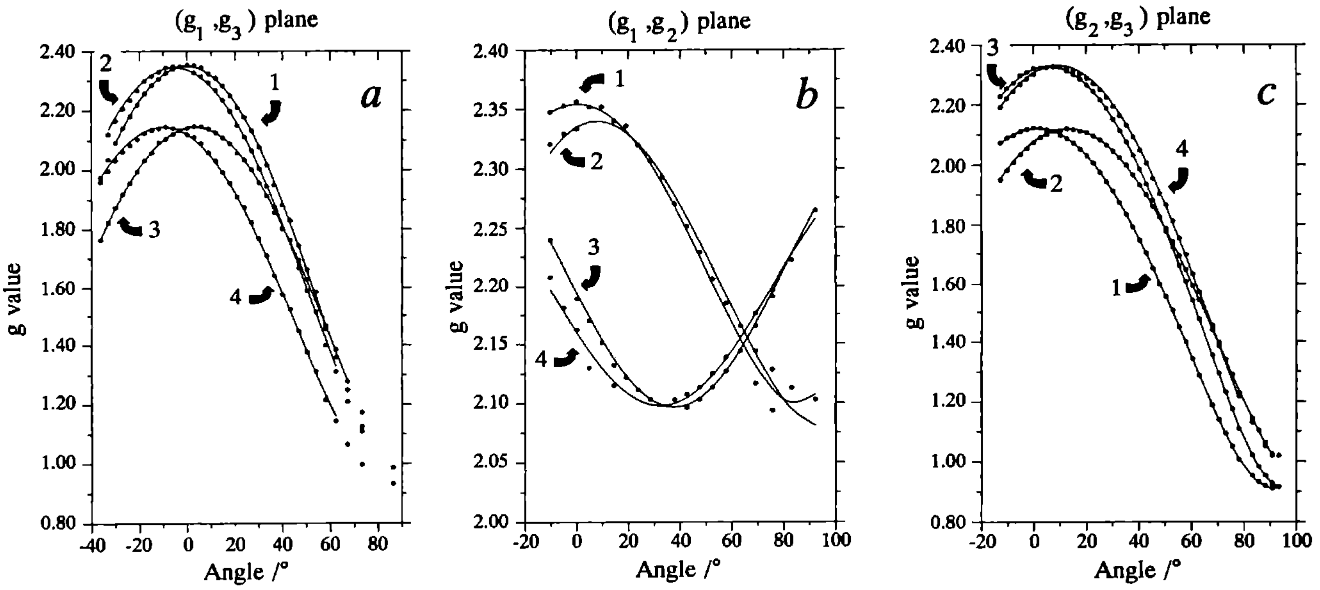

Figure 7.5
Angular dependence of the EPR lines in three perpendicular planes for the four sites in the 2Or crystal. The dots represent the measured values, the lines are the fits. The numbering of the sites in this figure agrees with the numbering of the sites in table 7.3.
a Angular dependence for $\vec{B}_0$ in the (g_1, g_3) plane of site 1. At an angle of 0°, the magnetic field is parallel to the g_1 axis of site 1; at an angle of 90°, the magnetic field is parallel to the g_3 axis of site 1.
b Angular dependence for $\vec{B}_0$ in the (g_1, g_2) plane of site 1 At an angle of 0°, the magnetic field is parallel to the g_1 axis of site 1, at an angle of 90°, the magnetic field is parallel to the g_2 axis of site 1.
c Angular dependence for $\vec{B}_0$ in the (g_1, g_3) plane of site 1. At an angle of 0°, the magnetic field is parallel to the g_2 axis of site 1, at an angle of 90°, the magnetic field is parallel to the g_3 axis of site 1.

all sites). It is not clear why the values of g_1 for sites 3 and 4 differ that much from the value found for sites 1 and 2.

Table 7.3 presents the direction cosines of the principal g axes for the four sites with respect to the crystal axes. Figures 7.6a and b contain the g tensor axes of the two sites lying in one of the 1M units composing the 2Or unit cell (see figure 7.1). The g tensor axes of site 1 and 3 (figure 7.6a) are related by the symmetry elements of the monoclinic space group, as are the g tensor axes of the tensors 2 and 4 (figure 7.6b). But still another symmetry operation can be discerned which exists between figures 7.6a and 7.6b. For instance, if the g tensor axes of site 1 in figure 7.6a are rotated over 180° around the crystallographic c axis, these axes correspond with the g tensor axes of site 2 in figure 7.6b. If the g tensor of site 4 is manipulated likewise, this tensor equals the g tensor of site 3. This phenomenon is in agreement with the model of Kohn and Townes. They found that the 2Or unit cell is composed of two stacked 1M unit cells which are related to each other by a rotation of 180° around the c axis (see figure 7.1). Now we can give a possible explanation for the different intensities of the EPR lines in figure 7.4. The different intensities of the lines can be explained by assuming that the 2Or crystal contains domains having a 1M structure. The existence of these domains has been reported by Fukada et al.[9]. These domains contribute to the intensity of only two of the four observed EPR

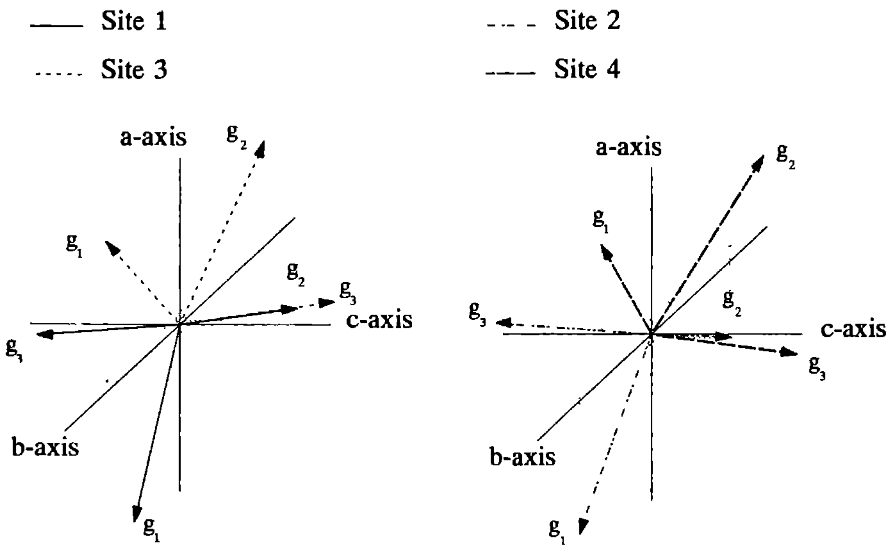

Figure 7.6
a Orientations of the principal g tensor axes of site 1 and site 3 with respect to the crystal axes.
b Orientations of the principal g tensor axes of site 2 and site 4 with respect to the crystal axes.

lines, because the g tensors in the 1M domains are oriented parallel to the g tensors in one of the two stacked 1M unit cells which construct the 2Or unit cell.

The three-layer monoclinic structure (3M)

Figure 7.7 shows an EPR spectrum of the 3M crystal for $\vec{B}_0 \approx 7°$ away from the c axis.

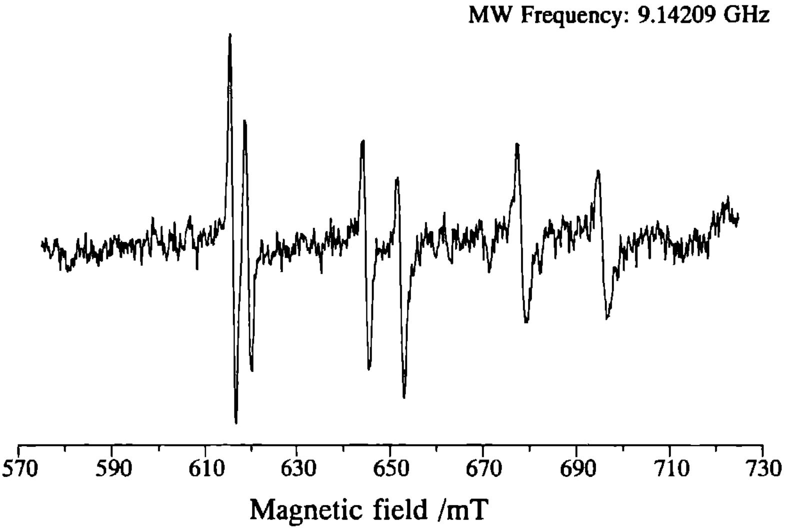

Figure 7.7
Typical EPR spectrum for the 3M crystal. This spectrum has been measured for $\vec{B}_0 \approx 7°$ *away from the c axis.*

Clearly, six lines are observed, corresponding to the six sites present. This number of sites was to be expected considering table 7.1. The linewidth of the resonance lines is about 0.8 mT.

Figure 7.8 depicts the angular dependence of the six EPR lines in three orthogonal planes (see experimental part). In the figures 7.8a and 7.8b one can observe once more that the g_3 axis (for all sites) lies close to the c axis. In figure 7.8c one notices (as with figure 7.5c) an amalgamation of all lines into one at an angle of about 65°, because in this direction the field is parallel to the b axis. The data were analyzed in the same way as pointed out for the 1M crystal.

The average principal g-values were calculated as $g_1 = 2.342 \pm 0.005$, $g_2 = 2.095 \pm 0.004$ and $g_3 = 0.94 \pm 0.03$. Table 7.4 presents the direction cosines of the principal g axes for the six sites. In the figures 7.9a to 7.9c we have drawn the g tensor axes of those sites which lie in one of the 1M units composing the 3M structure (see figure 7.1). It can be checked that in all three figures the g tensor axes of the corresponding two sites fulfil the monoclinic symmetry relations. Also the conditions formulated by Kohn and Townes are

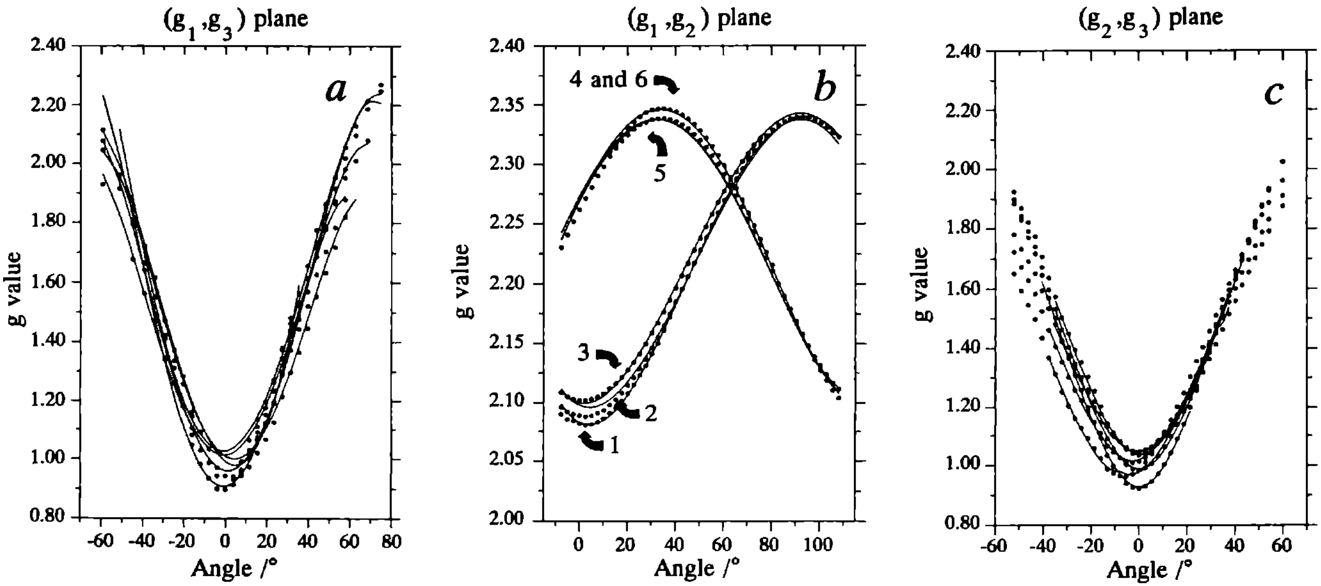

Figure 7.8

Angular dependence of the EPR lines in three perpendicular planes for the two sites in the 3M crystal. The dots represent the measured values, the lines are the fits The numbering of the sites in the figures 7 8a and c has been omitted for clarity reasons. The numbering of the sites in figure 7 8c agrees with the numbering of the sites in table 7.4.

a Angular dependence for $\vec{B}_0$ in the (g_1, g_3) plane of site 1. At an angle of 0°, the magnetic field is parallel to the g_3 axis of site 1.

b Angular dependence for $\vec{B}_0$ in the (g_1, g_2) plane of site 1 At an angle of 0°, the magnetic field is parallel to the g_2 axis of site 1, at an angle of 90°, the magnetic field is parallel to the g_1 axis of site 1.

c Angular dependence for $\vec{B}_0$ in the (g_2, g_3) plane of site 1. At an angle of 0°, the magnetic field is parallel to the g_3 axis of site 1.

Table 7.4
Principal values of the g tensor and direction cosines of the g-tensor axes with respect to the crystal axes for the three-layer monoclinic structure (3M).

	Site 1			Site 2			Site 3		
	g_1	g_2	g_3	g_1	g_2	g_3	g_1	g_2	g_3
a^*	-0.879	-0.475	-0.036	-0.881	-0.472	-0.023	0.880	0.475	0.027
b	0.476	-0.877	-0.064	0.472	-0.882	0.003	0.475	-0.879	-0.028
c	0.000	0.073	-0.997	0.018	0.013	-1.000	0.010	-0.037	0.999
principal values	2.339	2.091	0.92	2.345	2.103	0.97	2.351	2.089	0.89

	Site 4			Site 5			Site 6		
	g_1	g_2	g_3	g_1	g_2	g_3	g_1	g_2	g_3
a^*	0.873	0.486	0.034	-0.851	-0.523	0.049	0.859	0.508	-0.069
b	0.489	-0.872	-0.093	0.524	-0.851	0.018	0.510	-0.860	0.011
c	-0.012	-0.048	0.994	-0.032	-0.041	-0.999	0.054	0.044	0.998
principal values	2.342	2.095	0.96	2.338	2.097	0.96	2.338	2.097	0.94

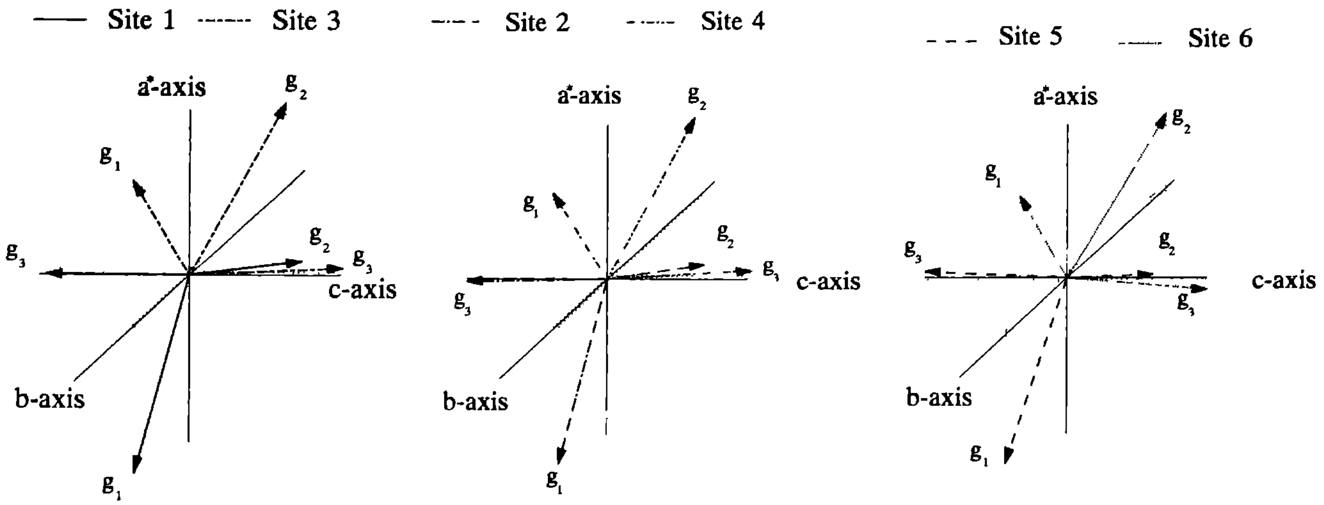

Figure 7.9
a Orientations of the principal g tensor axes of site 1 and site 3 with respect to the crystal axes
b Orientations of the principal g tensor axes of site 2 and site 4 with respect to the crystal axes
c Orientations of the principal g tensor axes of site 5 and site 6 with respect to the crystal axes.

satisfied: if the g tensor axes of site 2 in figure 7.9b are rotated over 180° around the crystallographic c axis, these axes correspond with the g tensor axes of site 5 in figure 7.9c. If the g tensor of site 6 is manipulated likewise, this tensor equals the g tensor of site 4. In addition to this, the g tensors of sites 1 and 5, and those of 3 and 6 are (almost) the same (table 7.4). These phenomena are also in agreement with the model of Kohn and Townes. They found that the 3M unit cell is composed of a 2Or like unit cell which is stacked on an 1M like unit cell (see figure 7.1).

7.4 Conclusion

It has shown with EPR that the structure of $K_3Co(CN)_6$ exhibiting polytypism can be determined easily by doping it with $Fe(CN)_6^{3-}$. The number of resonance lines for an arbitrary orientation of the magnetic field is indicative for the type of crystal studied: 1M, 2Or, 3M, 4Or or 7M. The model of Kohn and Townes developed for this type of crystals is supported by the measured orientations of the g tensors of the various sites.

We would like to express our thanks to J. Smits for the careful X-ray studies performed on the crystals reported in this article. The authors would also like to express their gratitude to A.A.K. Klaassen and G.E. Janssen for their technical support.

7.5 Appendix A

The 7M (seven-layer monoclinic) unit cell can be constructed in N different ways. The value of N is given by a simple equation. In order to derive this equation, a basic requirement should be fulfilled the lower corners of the 7M unit cell have to coincide with the lower corners of a 1M like unit cell, and the upper corners of the 7M unit cell have to coincide with the upper corners of another 1M like unit cell (see figure 7.10). The mathematical formulation of this requirement is given by equation 7.1:

$$7\,a\cos(\phi) \;=\; k\,c + n\,a\cos(\phi) \;-\; (7-n)\,a\cos(\phi)\quad k,n \in \mathbb{N}\quad k \geq 1. \tag{7.1}$$

in which a = 7.00 ± 0.02 Å, c = 8.37 ± 0.02 Å, $\phi = 180^\circ - \beta = 72.8^\circ$, $7a\cos(\varphi)$ is the projection of the a axis of a 7M unit cell on the c axis, and $na\cos(\phi)$ is defined analogously (n is the number of 1M like unit cells of type I belonging to a particular value of k). Equation 7.1 can be rewritten as:

$$2\,n = 2\cdot 7 - \frac{c\,k}{a\,\cos(\phi)}. \tag{7.2}$$

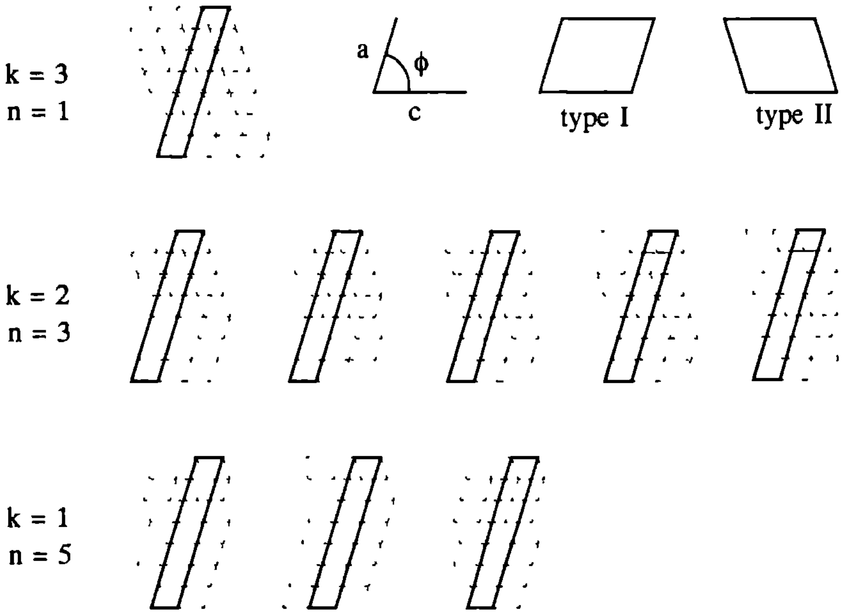

Figure 7.10
Nine different stacking sequences which construct a 7M unit cell. The different types of 1M like unit cells are schematically indicated by their projections along the b axis

When the numerical values of a, c and ϕ are entered into equation 7.2 this results in:

$$n = 7 - 2\,k. \tag{7.3}$$

Equation 7.3 gives the upper limit for k (because n > 0) therefore: $1 \leq k \leq 3$. This reduces the problem to the question: in how many different ways can n unit cells be distributed over a total of seven unit cells, for a given value of k? The answer for all possible values of k is given by equation 7.4:

$$N = \sum_{k=1}^{3} \frac{(7-1)!}{(7-2k)!\,(2k)!}. \tag{7.4}$$

Using equation 7.4, we find that a 7M unit cell can be constructed in nine different ways (see figure 7.10). Erroneously, Kohn and Townes [3] reported a number of eight.

7.6 Appendix B

The one layer monoclinic (1M) crystal as well as the three layer monoclinic (3M) crystal, belong to the space group $P2_1/c$ (no 14). There are four symmetry operations associated with this space group [10]:

- The unity operator.
- The inversion operator, which transfers an arbitrary point (x,y,z) to (-x,-y,-z).
- A twofold screw axis parallel to the b axis of the crystal. This operation transfers the point (x,y,z) to (- x,y+$\frac{1}{2}$b,-z+$\frac{1}{2}$c).
- An 'axial' glide plane parallel to the ac plane, which transfers (x,y,z) to the point (x,-y+$\frac{1}{2}$b,z+$\frac{1}{2}$c).

It is obvious that these symmetry operations will also have an effect on the directions principal components of the g tensor, though the results of these operators may be only partially detectable by EPR. The result of a translation operator cannot be discerned by an EPR experiment, therefore, the result from a twofold screw axis cannot be distinguished from the effect of a twofold rotation axis. Likewise, the impact of a glide plane is indistinguishable from that of a mirror plane. Furthermore, the inversion operator cannot be detected because the g tensor is invariant for this operator. Consequently, only two symmetry operators can be discerned by observing the orientations of the principal g tensor components:

- A twofold rotation axis around the b axis.
- A mirror parallel to the ac plane.

The two layer orthorhombic (2Or) crystal, belong to the space group Pnca (no 60). There are eight symmetry operations associated with this space group [10]:

- The unity operator.
- The inversion operator, which transfers an arbitrary point (x,y,z) to (-x,-y,-z).
- A twofold screw axis parallel to the a axis of the crystal. This operation transfers (x,y,z) to the point (x+$\frac{1}{2}$a,-y+$\frac{1}{2}$b, -z+$\frac{1}{2}$c).
- A twofold rotation axis parallel to the b axis of the crystal. This operation transfers the point (x,y,z) to (-x,y,- z+$\frac{1}{2}$c).
- A twofold screw axis parallel to the c axis of the crystal. This operation transfers the point (x,y,z) to the point (-x,-y+$\frac{1}{2}$b,z+$\frac{1}{2}$c).
- An 'diamond' glide plane parallel to the bc plane, which transfers (x,y,z) to the point (-x+$\frac{1}{2}$a,y+$\frac{1}{2}$b, z+$\frac{1}{2}$c).

- An 'axial' glide plane parallel to the ac plane, which transfers (x,y,z) to (x,-y,z+$\frac{1}{2}$c).
- An 'axial' glide plane parallel to the ab plane, which transfers the (x,y,z) to the point with the coordinates (x+$\frac{1}{2}$a,y,-z+$\frac{1}{2}$c).

For the reasons mentioned above, only three symmetry operators can be discerned by observing the orientations of the principal g tensor components:

- A mirror parallel to the ab plane.
- A mirror parallel to the ac plane.
- A mirror parallel to the bc plane.

References

[1] Groth, P , 1906, *Chemische Kristallographie*, **1**, 418

[2] Barkhatov, V and Zhadonov, H , 1942, *Acta Phys -Chem , URSS*, **16**, 43

[3] Kohn, J A and Townes, W D , 1961, *Acta Cryst* , **14**, 617

[4] Reynhardt, E C and Boeyens, J C A , 1972, *Acta Cryst* , **B28**, 524

[5] Baker, J M , Bleaney, B and Bowers, B , 1956, *Proc phys Soc B* , **69**, 1216

[6] Wang, D M , Meyers, S M and de Boer, E , 1990, *Mol Phys* , **70**(6), 1135

[7] Willems, J P , Klaassen, A A K , Reijerse, E J , Janssen, G E and de Boer, E , 1992, *Rev Sci Instrum* , **63**(11), 5362

[8] Keijzers, C P , Reijerse, E J , Stam, P , Dumond, M F and Gribnau, M C M , 1987, *J Chem Soc Faraday Trans 1*, **83**, 3493

[9] Fukada, S Horiuchi, K Asaji, T and Nakamura, D , 1986, *Ber Bunsenges Phys Chem* , **90**, 22

[10] Hahn, T , 1983, *International Tables for Crystallography, Volume A*, (D Reidel Publishing Compagny, Dordrecht)

Chapter 8

A single-crystal ESEEM study of $Fe(CN)_6^{3-}$ doped into $K_3Co(CN)_6$

Indications for a structural phase transition [1]

An ESEEM study has been performed on $Fe(CN)_6^{3-}$ doped into $K_3Co(CN)_6$. The experimental facts indicate that a phase transition occurs between 10 and 65 K. Analysis of the ESEEM spectra measured at 7 K leads to the conclusion that the $Fe(CN)_6^{3-}$ ion has lost its inversion centre below the phase-transition temperature. From the angular dependence of the ESEEM lines it was inferred that, compared with the structure at room temperature the $M(CN)_6^{3-}$ ($M = Fe^{3+}$, Co^{3+}) unit at low temperature is rotated by an angle of 54.7° around the c axis of the crystal. After this rotation the major principal axes of the hyperfine and quadrupole tensors coincide with the iron-cyanide bonds. This is in agreement with what could be expected on the basis of earlier ENDOR studies of the same complex in other hosts.

8.1 Introduction

The $Fe(CN)_6^{3-}$ complex is an example of a low-spin ($S = \frac{1}{2}$) complex, and therefore is a good candidate for the investigation of the electron spin distribution with electron paramagnetic resonance (EPR). An elaborate study on this complex at $T = 4.2$ K doped into a single crystal of KCl using EPR, electron nuclear double resonance (ENDOR) and electron spin echo envelope modulation (ESEEM) was carried out by Wang and de Boer [1]. This study was followed by an EPR investigation by Wang et al. [2] on the same complex at 4.2 K in KCl and NaCl. A year later Kirmse et al. [3] reported the results of an ENDOR study performed at 4.2 K on $Fe(CN)_6^{3-}$ doped into NaCl.

When the $Fe(CN)_6^{3-}$ complex is doped into an alkali halide crystal the Fe^{3+} ion replaces an alkali ion and six Cl^- ions are replaced by CN^- groups. Due to the necessity of charge compensation, replacement of the monovalent alkali ion by the trivalent Fe^{3+} ion introduces two negatively charged vacancies. In the above-mentioned studies it was found that the effect of the presence of these vacancies is quite pronounced. One of the principal g tensor axes is directed towards a vacancy. The axis having the lowest g value was found to be perpendicular to the plane in which the vacancies are located (see figure 8.1). Moreover,

---

[1] The contents of this chapter has been published in J. Mol. Phys., **83**, December 1994, pages 1155 to 1169, by: J.-P. Willems, E.J. Reijerse and E. de Boer

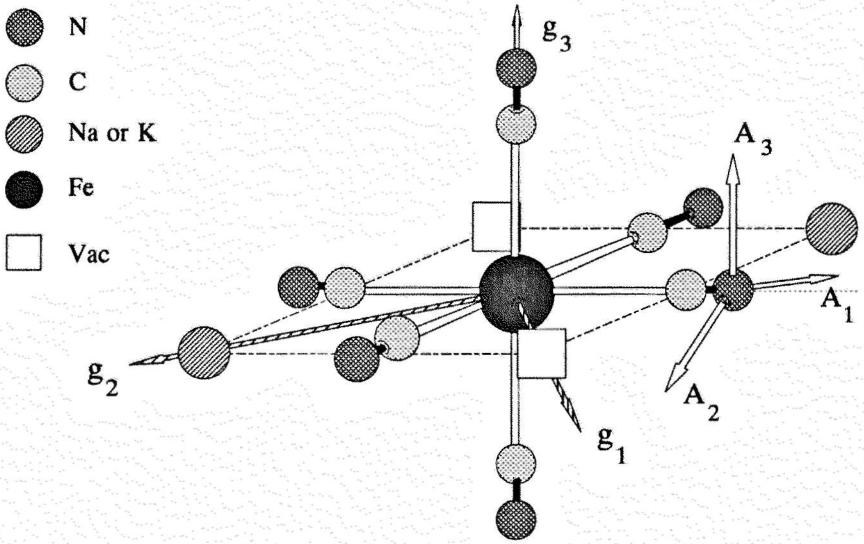

Figure 8.1
Orientations of the g and ^{14}N hyperfine tensors in $Fe(CN)_6^{3-}$ doped NaCl.

it was found that one of the principal ^{14}N hyperfine tensor axes and one of the principal ^{14}N quadrupole tensor axes deviated from the direction of an Fe-CN bond. The reported deviation from this bond direction was 6° for the hyperfine tensor axis and 8° for the quadrupole tensor axis. The vacancies were held responsible for this deviation. Given the major influence of the vacancies on the directions of the g tensor axes, the hyperfine tensor axes and the quadrupole tensor axes, and thus in general on the electron distribution, it is of interest to eliminate these vacancies and to assess the effect of this on the electron distribution in $Fe(CN)_6^{3-}$. In the present study therefore, the $Fe(CN)_6^{3-}$ complex has been doped into the diamagnetic host $K_3Co(CN)_6$. An earlier EPR study on this system has been carried out by Baker et al. [4] in 1956, and has led, among other results, to the determination of the g tensor. To obtain the electron distribution in $Fe(CN)_6^{3-}$, we have performed ESEEM experiments. During the course of these experiments unexpected effects were encountered. In this chapter we report on these and in a following paper the experimental g, hyperfine and quadrupole tensors will be compared with theoretical calculations [5].

The ESEEM spectra only show signals originating from nitrogen atoms, and hence no information could be obtained regarding ^{13}C, ^{39}K, ^{57}Fe and ^{59}Co. The absence of ^{13}C and ^{57}Fe signals can be explained by the low natural abundances of these nuclei which are 1.11 and 2.15 %, respectively. This explanation does not hold for the absence of signals from ^{59}Co (100% abundance) and ^{39}K (93% abundance). It is likely that the interactions with cobalt and potassium ions are mainly isotropic, so that no ESEEM signals can occur. This suggestion is substantiated by the appearance of cobalt lines in the measured ENDOR spectra. These cobalt lines did not shift very much by varying the direction of the external magnetic field. Unfortunately we were not able to analyze these spectra due to the overwhelming number of ENDOR lines from nitrogen (I = 1) and cobalt (I = 7/2) atoms lying in the same frequency range (3 - 5 MHz) of the spectrum.

8.2 Experimental

The crystal growth and the EPR spectra of $Fe(CN)_6^{3-}$ doped into $K_3Co(CN)_6$ have been reported elsewhere [6]. It is well known that $K_3Co(CN)_6$ exhibits polytypism [6-10]. EPR and X-ray [11] measurements guaranteed that the crystal studied by us is a so-called one-layer monoclinic (1M) crystal. The crystal parameters are listed in table 8.1.

Table 8.1
The unit cell parameters of the one-layer monoclinic (1M) crystal of $K_3Co(CN)_6$ *[7-9], [11], [17].*

a/Å	b/Å	c/Å	β/°	Space group
7.070 ± 0.002	10.402 ± 0.004	8.360 ± 0.003	107.20 ± 0.02	$P2_1/c$

The ESEEM experiments were carried out on a Bruker ESP 380 X-band FT-EPR spectrometer, equipped with a homebuilt 3-loop/2-gap resonator especially designed for single crystal experiments [12]. The spectra were recorded at 7 K, using an Oxford CF200 flow cryostat. A stimulated echo pulse sequence was used: $\frac{1}{2}\pi - \tau - \frac{1}{2}\pi - T - \frac{1}{2}\pi - \tau -$echo. The pulses are trapeze shaped with rise and fall times of typically 4 ns. A four-step phase cycle was employed to eliminate unwanted echoes [12,13]. The width of the pulses was 56 ns, the value of τ was 256 ns and the initial value of T was set on 200 ns. The time T was increased in steps of 32 ns, and each spectrum consists of 2048 points, leading to a frequency resolution in the ESEEM spectra of 15.3 kHz. Measurements were taken in the planes spanned by (g_1, g_2) , (g_1, g_3) and (g_2, g_3) . The magnetic field could be oriented parallel to a principal g tensor axis with an accuracy of 0.5°, enabling us to verify that the spectra were indeed recorded in the above-mentioned planes. Recordings of the spectra were made at intervals of 4°± 0.5°. The data analysis was performed using the universal spin-Hamiltonian program MAGRES [14]. To facilitate the interpretation of the ESEEM spectra, some HYSCORE (hyperfine sublevel correlation) experiments were performed [12,15,16]. The pulse sequence used in these experiments was: $\frac{1}{2}\pi - \tau - \frac{1}{2}\pi - T1 - \pi - T2 - \frac{1}{2}\pi - \tau -$ echo. Again a four-step phase cycle was employed to eliminate unwanted echoes. The $\frac{1}{2}\pi$ pulses were 56 ns wide, the π pulse was 96 ns wide, τ had a value of 200 ns and the initial values of T1 and T2 were 200 ns. The times T1 and T2 were independently increased in steps of 32 ns. A typical HYSCORE spectrum consisted of 256 × 256 points, leading to a frequency resolution of 61 kHz.

8.3 Results

g tensor

Figure 8.2 shows the principal directions of the g tensor with respect to the positions of the cyanide groups in the complex. The axes of the unit cell, determined at room temperature, are given as a reference axes system [9],[17]. The principal values of the g tensor, determined by Baker et al. [4] and by us [6] at 7 K, are: $g_1 = 2.344 \pm 0.006$, $g_2 = 2.1039 \pm 0.0001$, $g_3 = 0.902 \pm 0.004$ (see also table 8.2). There is a remarkable resemblance between the orientation of the g components in NaCl and KCl as shown in

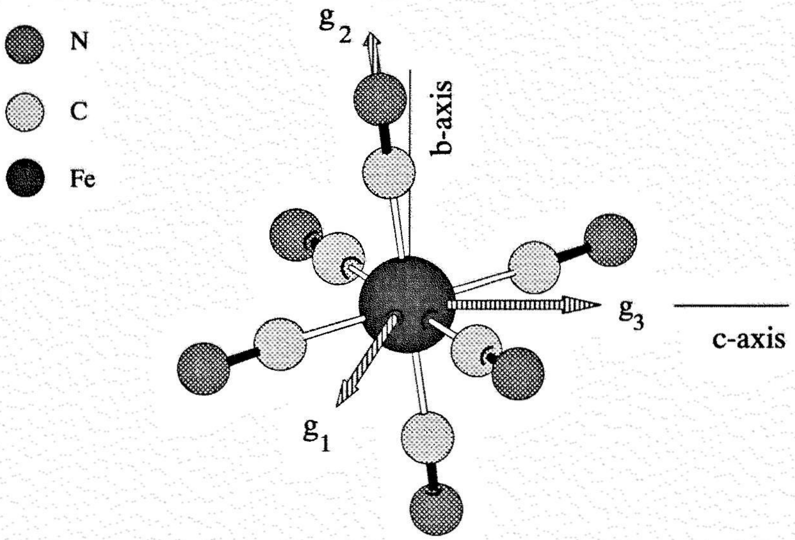

Figure 8.2
Orientation of the g tensor of $Fe(CN)_6^{3-}$ *doped into* $K_3Co(CN)_6$ *with respect to the crystal axes.*

Table 8.2
Principal values of the g tensor and the direction cosines of the principal components with respect to the crystal axes [6].

	g_1	g_2	g_3
a^*	-0.865	-0.502	-0.001
b	0.501	-0.863	0.068
c	0.028	0.062	-0.998
principal values	2.344 ± 0.006	2.1039 ± 0.0001	0.902 ± 0.004

figure 8.1 and the orientation in $K_3Co(CN)_6$ as displayed in figure 8.2. In all these hosts only one axis of the g tensor is parallel to an iron-cyanide bond, while the other two g tensor axes are parallel to the bisectors of the iron-cyanide bonds. However, there is one noteworthy difference: the g tensor component having the lowest principal value is along an iron-cyanide bond in NaCl and KCl, but in $K_3Co(CN)_6$ it is along a bisector of the iron-cyanide bonds.

ESEEM

Figure 8.3 shows a schematic diagram of the energy levels and the assignments of the ESEEM transitions of ^{14}N for both electron-spin manifolds ($m_s = \pm\frac{1}{2}$). For each ^{14}N nucleus a maximum of six ESEEM lines can be expected. Hence for $Fe(CN)_6^{3-}$ having an inversion centre a maximum of 18 ESEEM lines should be observed: six lines from every pair of equivalent ^{14}N nuclei. Figure 8.4 presents a typical ESEEM spectrum measured at 7 K. The linewidth of the ESEEM lines is approximately 40 kHz. It is clear that more than the predicted 18 lines can be distinguished. In fact the spectra suggest that each line has split into two. In figure 8.4 this splitting has been indicated for three lines with the symbol ⊓. Thus the ^{14}N ESEEM spectra of $Fe(CN)_6^{3-}$ doped into $K_3Co(CN)_6$ seem to arise from more than three magnetically distinguishable ^{14}N nuclei. This suggests that the $M(CN)_6^{3-}$ unit (M = Fe^{3+}, Co^{3+}) of $Fe(CN)_6^{3-}$ doped into $K_3Co(CN)_6$ has lost

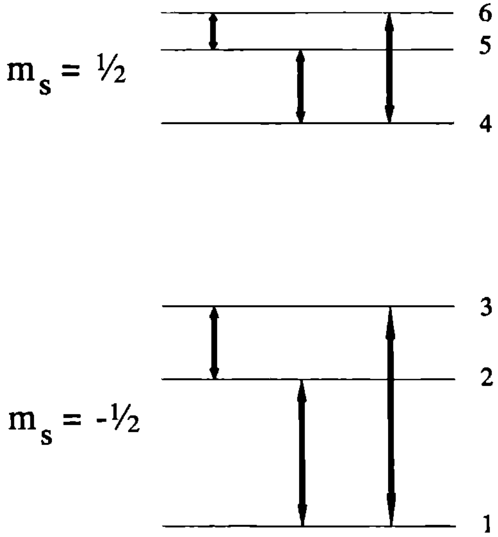

Figure 8.3
Energy level scheme and possible ESEEM transitions of ^{14}N

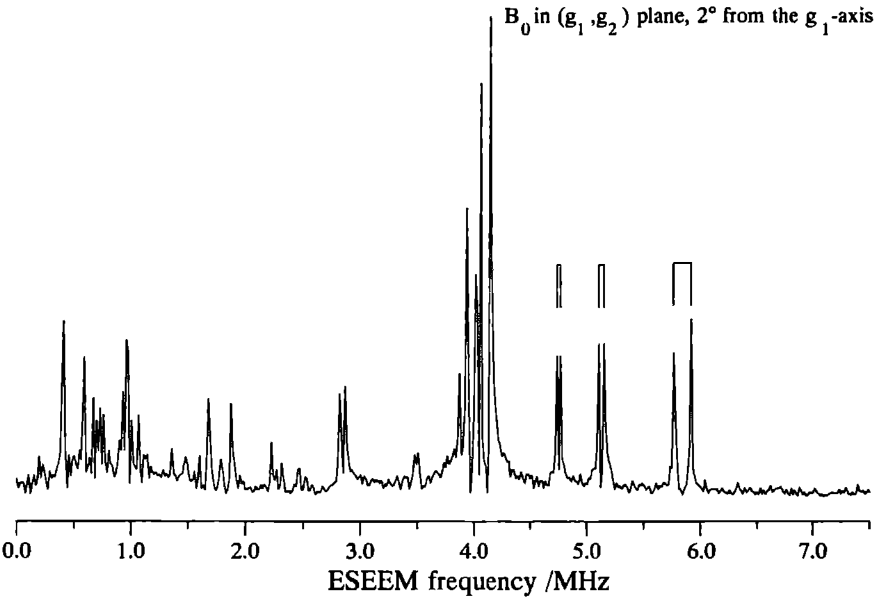

Figure 8.4
Typical ESEEM spectrum of $Fe(CN)_6^{3-}$ doped into $K_3Co(CN)_6$. This spectrum has been measured in the (g_1, g_2) plane with the $\vec{B}_0$ field 2° away from the g_1 axis. For three lines the splitting has been indicated by the symbol ⊓.

its inversion symmetry. For many orientations in the (g_1, g_2)) plane at least 5 of the 6 possible transitions per ^{14}N nucleus could be observed. This leads to a total of 30 observable transitions. In the two other planes a maximum of only four transitions was observable per ^{14}N nucleus, resulting in a maximum of 24 lines.

Figures 8.5a to 8.5c show the positions of the measured ESEEM signals for a set of three of the six inequivalent ^{14}N nuclei, as a function of the orientation of the external magnetic field in three mutually perpendicular planes. The symbols represent the experimental data points. Similar plots were obtained for the other set of three inequivalent ^{14}N nuclei, which are related above the phase-transition temperature to the presented set of inequivalent ^{14}N nuclei by inversion symmetry.

At several orientations of the magnetic field, level anticrossing occurs between levels having the same symmetry. For instance in figure 8.5b ((g_1, g_2) plane) level anticrossing is observed for the 1↔3 and 2↔3 transitions approximately 36° away from the g_2 axis (the g_2 axis lies parallel to the field at an angle of 0°). Level anticrossing of ESEEM lines belonging to the same ^{14}N nucleus (N1) in the same plane is found for the 4↔6 and 5↔6 transitions approximately 32° away from the g_2 axis. In the (g_1, g_3) plane (figure 8.5a) level anticrossing is found for the 1↔3 and 2↔3 transitions circa 56° away from the g_1 axis (the g_1 axis is found at 0°).

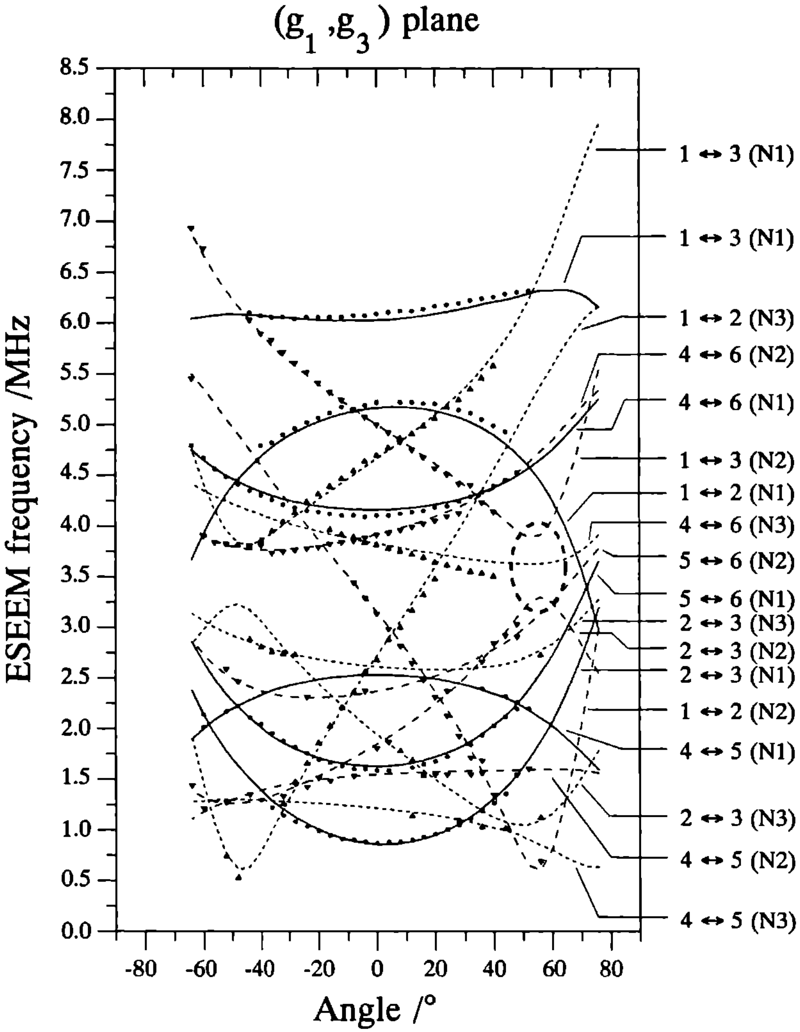

Figure 8.5 a

This figure show the ^{14}N ESEEM lines of only three of the six inequivalent ^{14}N atoms in the (g_1, g_3) plane The lines represent the fits, the symbols represent the experimental data points. Solid lines, circles. Signals of nucleus N1. Dashed lines, triangles down. Signals of nucleus N2. Dotted lines, diamonds. Signals of nucleus N3. The level anticrossing between two transitions has been indicated by an ellipse At the angle of 0° the external magnetic field, $\vec{B}_0$, is parallel to the g_1 axis. The microwave frequency was 9.9518 GHz.

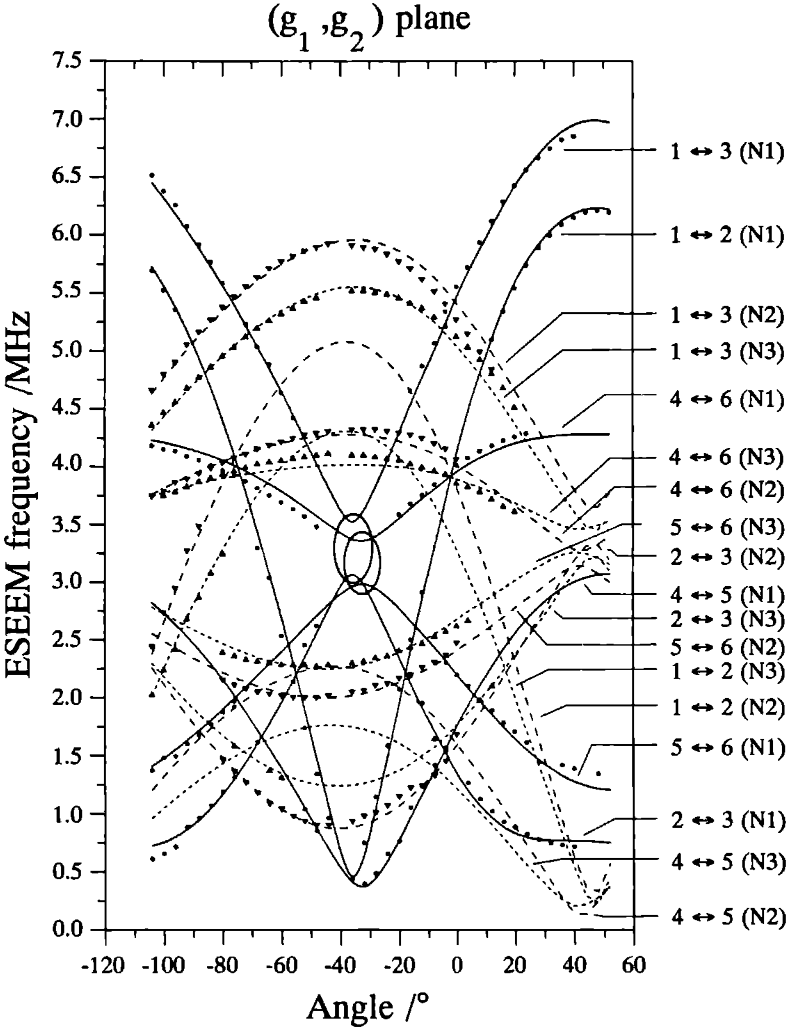

Figure 8.5 b

This figure show the ^{14}N ESEEM lines of only three of the six inequivalent ^{14}N atoms in the (g_1,g_3) plane. The lines represent the fits, the symbols represent the experimental data points. Solid lines, circles: Signals of nucleus N1. Dashed lines, triangles down: Signals of nucleus N2. Dotted lines, diamonds: Signals of nucleus N3. The level anticrossing between two transitions has been indicated by an ellipse. At the angle of 0° the external magnetic field, $\vec{B}_0$, is parallel to the g_2 axis. The microwave frequency was 9.9157 GHz.

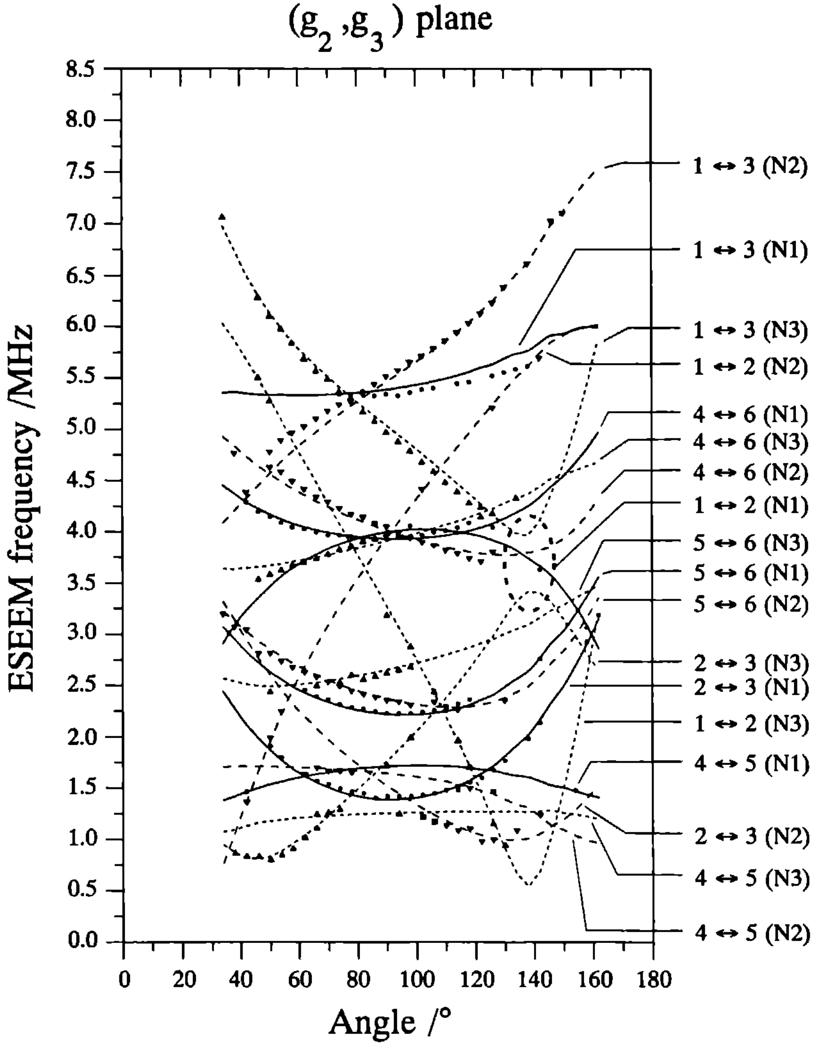

Figure 8.5 c

This figure show the ^{14}N ESEEM lines of only three of the six inequivalent ^{14}N atoms in the (g_2, g_3) plane. The lines represent the fits, the symbols represent the experimental data points. Solid lines, circles Signals of nucleus N1. Dashed lines, triangles down Signals of nucleus N2 Dotted lines, diamonds: Signals of nucleus N3. The level anticrossing between two transitions has been indicated by an ellipse. At the angle of 90° the external magnetic field, $\vec{B}_0$, is parallel to the g_2 axis The microwave frequency was 9.9299 GHz.

The ESEEM spectra could be analyzed using the following spin Hamiltonian:

$$\mathcal{H} \;=\; \beta_e \vec{B}_0 \cdot \overline{\overline{g}} \cdot \vec{S} + \vec{S} \cdot \overline{\overline{A}} \cdot \vec{I} - g_n \beta_n \vec{B}_0 \cdot \vec{I} + \vec{I} \cdot \overline{\overline{Q}} \cdot \vec{I}. \tag{8.1}$$

The dotted, dashed and solid lines in the figures 8.5a to 8.5c represent the fits. The mean square error of all fits is less than 55 kHz: less than one and a half times the linewidth of an ESEEM line. Some of the fits (e.g. the 4↔6 transition of atom N3 in figure 8.5b) seem to have a systematical deviation from the measured points. Preliminary theoretical results indicate that this might be caused by the fact that the Hamiltonian used to analyze the spectra may not be entirely adequate.

The ESEEM lines originating from an inequivalent ^{14}N nucleus could be uniquely determined by verifying the sum rule for the double-quantum transitions. The HYSCORE spectra were a great help in the analysis of the complicated ESEEM spectra. A careful study of these spectra shows that the line splitting is also visible in the HYSCORE spectra. Figure 8.6 shows a HYSCORE spectrum in the (g_1, g_2) plane. The correlation peaks at the following frequency coordinates (in MHz): (0.9,4.3), (2.4,5.5) and (2.0,5.9) are clearly visible. The first correlation peak relates transition 2↔3 to transition 4↔6 (nucleus N2). The second peak correlates transition 1↔3 and transition 5↔6 of nucleus N2, and the third peak correlates transitions 1↔3 and 5↔6 (nucleus N3).

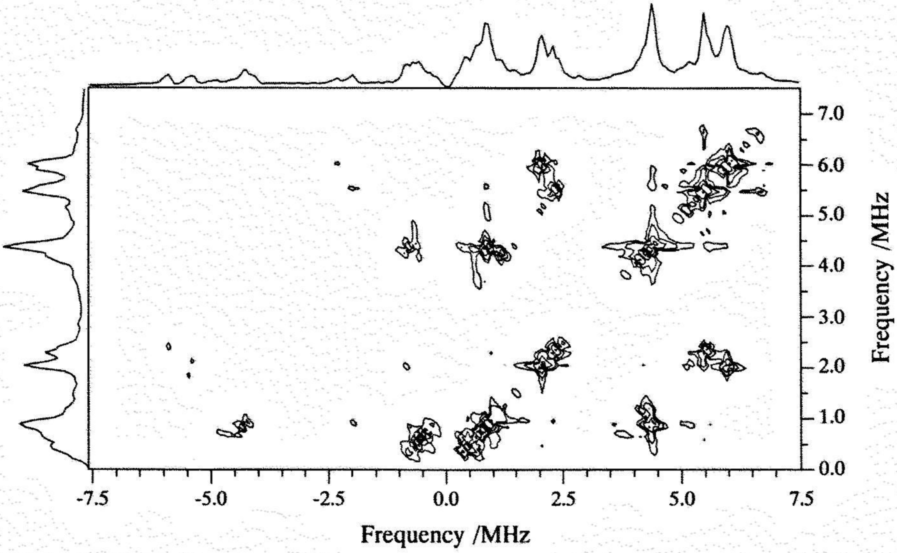

Figure 8.6
A HYSCORE spectrum for $\vec{B}_0$ 44° away from the g_2 axis.

8.4 Discussion

Line splitting

We attribute the observed line splitting (figure 8.4) to a structural phase transition at low temperatures. Such a phase transition was found by Fukada et al. [18] by investigating Fe^{3+} doped into $K_3Co(CN)_6$ using nuclear quadrupole resonance. They found a phase transition both in the monoclinic crystal 1M and in the orthorhombic crystal 2Or. This phase transition led to an inequivalence of the six nitrogen atoms and was interpreted in terms of a softening of a translational mode of the anions and/or cations. Because we were able to determine all six hyperfine and quadrupole tensors (see next section), we can compare our data with the results reported by Fukada et al. Table 8.3 shows the values of the quadrupole coupling constant e^2Qqh^{-1} and the asymmetry parameter η, as could be calculated using the quadrupole tensors found in our study. The values found by Fukada et al. are given for comparison. The quadrupole coupling constants obtained by us for the 1M crystal correspond quite satisfactorily to those which Fukada et al. reported for the 2Or crystal. In appreciating the results it should be realised that Fukada et al. measured the quadrupole tensor of ^{14}N nuclei surrounding a cobalt atom, whereas in the current study the quadrupole tensors of ^{14}N nuclei surrounding an iron atom have been measured. The values of the asymmetry parameters in our study are too diverse to make a comparison meaningful.

Table 8.3
Quadrupole coupling constants, e^2Qqh^{-1}, and asymmetry parameters, η, as obtained in the current study and as obtained by Fukada et al.[18] The symbol prime refers to the splitting.

	current study		Fukada et al. (1986)	
	e^2Qqh^{-1} / kHz	η	e^2Qqh^{-1} / kHz	η
N1	3651 ± 2	0.043 ± 0.004	undetermined	
N1'	3734 ± 12	0.10 ± 0.08		
N2	3832 ± 1	0.087 ± 0.005	3672.5	0.048
N2'	3825 ± 6	0.323 ± 0.008		
N3	3832 ± 5	0.071 ± 0.005	3361.7	0.055
N3'	3887 ± 6	0.088 ± 0.003		

Hyperfine and quadrupole tensors

The result of the analysis of the ESEEM spectra is given in tables 8.4 to 8.6. The symbol prime was used to indicate the tensor components related by inversion symmetry existing above the phase transition. These related components do not differ much, which could be expected from the small line splitting of each ESEEM line. Instead of giving the orientations of the principal components of the hyperfine and quadrupole tensors with respect to the crystal axes, as is usually done, we prefer to give the orientation of these

Table 8.4
Principal values of the ^{14}N hyperfine tensors. The orientations of these tensors with respect to the g tensor has also been presented.

		Angles/° with respect to the principal g tensor axes.		
	Values / 10^{-4} cm^{-1}	g_1	g_2	g_3
A_{1x}	1.685 ± 0.002	36.09 ± 0.01	126.01 ± 0.01	88.0 ± 0.1
A_{1y}	0.059 ± 0.005	121.7 ± 0.4	133.9 ± 0.6	60 ± 1
A_{1z}	0.032 ± 0.005	74.6 ± 0.7	65.4 ± 0.8	30 ± 1
A_{1iso}	0.592 ± 0.008			
A_{2x}	1.57 ± 0.01	58.63 ± 0.08	51.44 ± 0.05	125.7 ± 0.1
A_{2y}	0.10 ± 0.01	41 ± 3	131 ± 2	92 ± 3
A_{2z}	-0.17 ± 0.02	66 ± 3	65 ± 3	35.8 ± 0.3
A_{2iso}	0.50 ± 0.02			
A_{3x}	1.54 ± 0.01	64.1 ± 0.3	58.6 ± 0.5	42.8 ± 0.7
A_{3y}	0.0 ± 0.1	154 ± 2	75 ± 3	69 ± 2
A_{3z}	-0.01 ± 0.01	90 ± 3	35.4 ± 0.8	125 ± 2
A_{3iso}	0.5 ± 0.1			

components with respect to the g tensor axes. The justification for this is that the crystal axes system has been determined at a temperature above the critical temperature of the phase transition whereas the tensors presented in this study have been determined below this temperature. Table 8.2 gives the direction cosines of the components of the g tensor with respect to the crystal axes.

The hyperfine tensors are almost axial, so that the given angles for the "equatorial"

Table 8.5
As for table 8.4, but now the hyperfine parameters refer to the three related nitrogen atoms (indicated by the primes).

		Angles/° with respect to the principal g tensor axes.		
	Values / 10^{-4} cm^{-1}	g_1	g_2	g_3
A'_{1x}	1.667 ± 0.005	37.2 ± 0.1	127.1 ± 0.1	88.3 ± 0.7
A'_{1y}	0.02 ± 0.01	122.3 ± 0.6	132.9 ± 0.1	59.9 ± 0.8
A'_{1z}	-0.01 ± 0.01	74 ± 1	65.4 ± 0.2	30.2 ± 0.7
A'_{1iso}	0.56 ± 0.02			
A'_{2x}	1.56 ± 0.02	59.4 ± 0.3	50.38 ± 0.01	125.3 ± 0.3
A'_{2y}	0.07 ± 0.02	41 ± 3	131 ± 2	94 ± 3
A'_{2z}	-0.2 ± 0.2	65 ± 4	66 ± 3	35.6 ± 0.4
A'_{2iso}	0.5 ± 0.2			
A'_{3x}	1.55 ± 0.01	64.6 ± 0.2	59.0 ± 0.2	42.1 ± 0.7
A'_{3y}	0.020 ± 0.005	138 ± 3	48.1 ± 0.5	92 ± 2
A'_{3z}	-0.033 ± 0.009	59 ± 2	57 ± 3	132 ± 2
A'_{3iso}	0.51 ± 0.01			

Table 8.6
Principal values of the ^{14}N quadrupole tensors. The orientations of these tensors with respect to the g tensor has also been presented.

	Values / 10^{-4} cm^{-1}	Angles/° with respect to the principal g tensor axes.		
		g_1	g_2	g_3
Q_{1x}	0.318 ± 0.008	73 ± 17	90 ± 24	178 ± 43
Q_{1y}	0.291 ± 0.007	53 ± 18	36 ± 26	89 ± 39
Q_{1z}	-0.6088 ± 0.0005	143.4 ± 0.2	53.5 ± 0.2	92.0 ± 0.3
Q'_{1x}	0.34 ± 0.03	87 ± 14	89 ± 22	177 ± 36
Q'_{1y}	0.28 ± 0.04	54 ± 16	36 ± 21	87 ± 34
Q'_{1z}	-0.623 ± 0.002	144.0 ± 0.1	54.0 ± 0.1	92 ± 1
Q_{2x}	0.35 ± 0.01	50 ± 3	137 ± 2	103 ± 2
Q_{2y}	0.29 ± 0.01	53 ± 2	72 ± 3	42.0 ± 0.8
Q_{2z}	-0.6391 ± 0.0004	61.4 ± 0.3	52.5 ± 0.3	129.2 ± 0.5
Q'_{2x}	0.42 ± 0.02	55 ± 2	72 ± 4	40.7 ± 0.2
Q'_{2y}	0.22 ± 0.02	132 ± 3	45 ± 2	76 ± 2
Q'_{2z}	-0.638 ± 0.001	63 ± 1	49.75 ± 0.06	128 ± 1
Q_{3x}	0.342 ± 0.001	55 ± 1	142.0 ± 0.9	77.1 ± 0.8
Q_{3y}	0.297 ± 0.004	134 ± 1	109 ± 1	50.7 ± 0.3
Q_{3z}	-0.6391 ± 0.0009	64.8 ± 0.3	58.7 ± 0.2	42.2 ± 0.1
Q'_{3x}	0.353 ± 0.002	65 ± 2	145 ± 1	68 ± 1
Q'_{3y}	0.296 ± 0.002	143 ± 1	98 ± 2	54.3 ± 0.5
Q'_{3z}	-0.648 ± 0.001	64.8 ± 0.3	123.42 ± 0.03	44.6 ± 0.2

components are somewhat inaccurate. For $Fe(CN)_6^{3-}$ doped into NaCl or KCl, the ^{14}N hyperfine tensors for the equatorial ^{14}N atoms are rhombic. For $Fe(CN)_6^{3-}$ doped into NaCl was found that: $A_1 = 1.38$, $A_2 = 0.61$, $A_3 = -1.71$ and $A_{iso} = 0.09$ (values in 10^{-4} cm^{-1}), and for $Fe(CN)_6^{3-}$ doped into KCl: $A_1 = 1.43$, $A_2 = 0.45$, $A_3 = -1.53$ and $A_{iso} = 0.12$ (values in 10^{-4} cm^{-1}).

The quadrupole tensors listed in table 8.6 are also practically axial; thus here also not too much significance can be attached to the angles which the two "equatorial" components make with the principal g tensor axes. For $Fe(CN)_6^{3-}$ doped into NaCl, the quadrupole components for the equatorial ^{14}N atoms are: $Q_1 = 0.22$, $Q_2 = 0.41$ $Q_3 = -0.64$ (values in 10^{-4} cm^{-1}) and for $Fe(CN)_6^{3-}$ doped into KCl: $Q_1 = 0.32$, $Q_2 = 0.32$ $Q_3 = -0.64$ (values in 10^{-4} cm^{-1}). These values are comparable to those observed for the nitrogen atoms of $Fe(CN)_6^{3-}$ doped into $K_3Co(CN)_6$.

Tables 8.4 and 8.5 show that the hyperfine tensor axes of N1 and N1', and the hyperfine tensor axes of N2 and N2' are similarly oriented, while the orientations of the hyperfine tensor axes of N3 and N3' are slightly different. The principal values of the hyperfine tensors of N2 and N2' and of the hyperfine tensors of N3 and N3' are equal, while the principal values of the hyperfine tensors of N1 and N1' are (somewhat) different. The isotropic hyperfine constants are small and all equal to about 0.5 10^{-4} cm^{-1}, considerably larger than was found for $Fe(CN)_6^{3-}$ in NaCl and KCl. Table 8.6 demonstrates that the quadrupole tensor axes of N1 and N1', and the quadrupole tensor axes of N3 and N3' are similarly oriented, while the orientations of the quadrupole tensor axes of N2 and N2' are different. The slightly different orientations of the hyperfine and quadrupole components, combined with slightly different values of the principal values, result in a line splitting in the ESEEM spectra.

Finally, we note that the largest components of the hyperfine and quadrupole tensors have the same orientations (see tables 8.4 to 8.6). In figure 8.7 these components are depicted with respect to the framework of $Fe(CN)_6^{3-}$. Contrary to expectations, they are not directed along the iron-cyanide bonds. In the following section an explanation for this extraordinary behaviour will be presented.

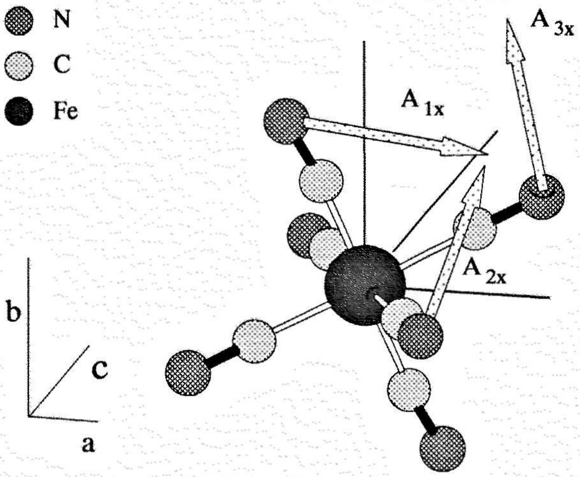

Figure 8.7
Orientations of the largest principal components of the ^{14}N hyperfine tensors with respect to the complex. The principal directions of the quadrupole tensors coincide with the directions of the hyperfine tensors (see tables 8.4 to 8.6). The crystal axes have been given as a reference axes system.

Below the phase transition

We have seen already that below the phase transition temperature the complex $M(CN)_6^{3-}$ ($M = Co^{3+}$, Fe^{3+}) has lost its inversion symmetry, resulting in a splitting of the ESEEM lines. The rotational plot in figure 8.5b indicates that the $Fe(CN)_6^{3-}$ complex also has lost all other symmetry elements, as is evident since the rotational plots for all nitrogen nuclei are different. From the behaviour of the plots it may be concluded that the deviation from the octahedral symmetry is minute.

There is still another experimental observation one to which so far we have not paid attention. This can best be illustrated with the aid of the figures 8.2 and 8.5b. If the external magnetic field ($\vec{B}_0$) is directed along the g_2 axis and therefore along an iron-cyanide bond (see figure 8.2), one set of two nitrogen atoms is equivalent and another set of four nitrogen atoms also (we disregard the slight deviation from octahedral symmetry). This would lead in the ESEEM spectrum to the appearance of 12 lines. In verifying this with the experimental spectrum one should bear in mind that, because of the deviation from octahedral symmetry, lines which should coincide under octahedral symmetry are now dispatched slightly from each other. For instance, the transitions 1↔3 of the nitrogen atoms N1, N2 and N3 should coincide for $\vec{B}_0 \parallel g_2$ for octahedral symmetry, but are in fact slightly displaced from each other by the deviation from octahedral symmetry, as can be seen in figure 8.5b. Taking this into consideration, at most 6 transitions for $\vec{B}_0 \parallel g_2$ can be distinguished instead of the 12 predicted.

If $\vec{B}_0$ is parallel to the bisector of the g_1 and the g_2 axis (in mathematical notation: $\vec{B}_0 \parallel \sphericalangle(g_1, g_2)$) it makes the same angles with three iron-cyanide bonds (assuming octahedral symmetry) and hence all nitrogen atoms are equivalent and one should observe only 6 lines in the ESEEM spectrum. It is clear that more than six lines are observed for $\vec{B}_0 \parallel \sphericalangle(g_1, g_2)$, even taking into account the deviation from octahedral symmetry. To be more specific, for instance, the transitions 1↔3 from the three nitrogen atoms considered in figure 8.5 (N1, N2 and N3) should coincide for $\vec{B}_0 \parallel \sphericalangle(g_1, g_2)$, which is certainly not the case, because transition 1↔3 of nitrogen atom N1 will never for this orientation coincide with those of nitrogen atoms N2 and N3. Interestingly, this situation occurs for $\vec{B}_0 \parallel g_2$, as can be seen in figure 8.5b. Puzzled by these facts, we checked the orientation of the g tensor as given by Baker et al. It was found to be correct. To reconcile the above-mentioned observations we had to assume that $\vec{B}_0$ makes equal angles with respect to the iron-cyanide bonds when $\vec{B}_0 \parallel g_2$ ($\vec{B}_0$ is parallel to the body diagonal formed by the iron-cyanide bonds). This can only be effected by a rotation of the cyanide complex by 54.7° (the magic angle) around the c axis (g_3 axis), since such a rotation brings the g_2 axis parallel to the body diagonal. The situation for $\vec{B}_0 \parallel \sphericalangle(g_1, g_2)$ is now also clarified because after the rotation by 54.7° around the c axis $\vec{B}_0$ is parallel to an iron-cyanide bond, so that more than 6 lines should be observable. To our satisfaction this rotation brings the largest components of the hyperfine and quadrupole tensors parallel to the iron-cyanide bonds (see figure 8.8). We consider this as strong evidence for the occurrence of this rotation of the cyanide groups over the magic angle around the c axis. The orientations of the principal directions of the hyperfine and the quadrupole tensor sketched in figure 8.7 is unrealistic and not acceptable. The finding of the rotation of the complex ion around the c axis by the magic angle solves this problem, but poses another one: why does it occur? We are unable to answer this question.

The final result depicted in figure 8.8 is in line with the results obtained on $Fe(CN)_6^{3-}$ in NaCl and KCl. The principal axes of the nitrogen hyperfine and quadrupole tensors of $Fe(CN)_6^{3-}$ present in these alkali halide hosts are also directed parallel to the iron-cyanide

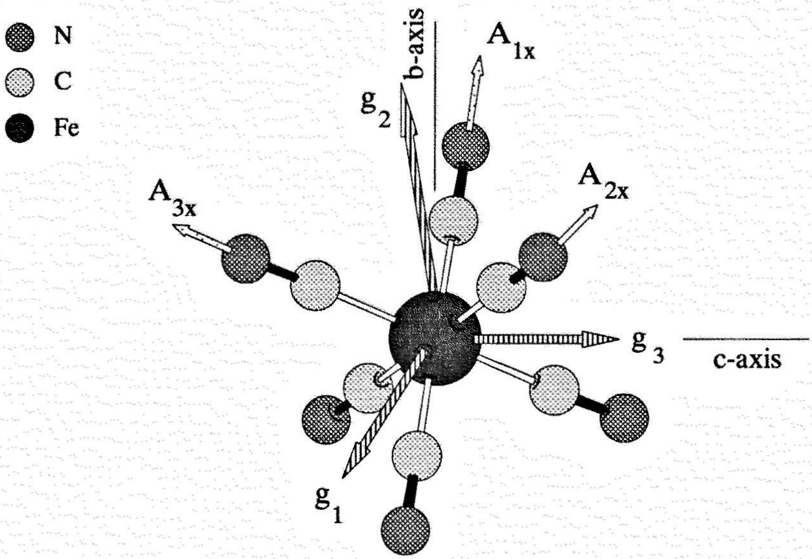

Figure 8.8
Orientations of the largest principal components of the ^{14}N *hyperfine tensors with respect to the complex. The principal directions of the quadrupole tensors coincide with the directions of the hyperfine tensors. The cyanide groups have been rotated by 54.7° around the c axis.*

bonds (see figure 8.1). As pointed out before, the slight deviations of the $^{N}A_1$ (and $^{N}Q_3$) component from the iron-cyanide bond in the latter case is caused by the perturbative effects of the charged vacancies, which are absent in $K_3Co(CN)_6$ doped with $Fe(CN)_6^{3-}$.

Unfortunately, the critical temperature of the phase transition in $K_3Co(CN)_6$ cannot be established by means of ESEEM measurements. The intensity of the ESEEM and EPR signals rapidly decrease at higher temperatures. When the temperature is above 15 K the signals disappear completely. Hence we can only give an upper and lower temperature limit for the transition temperature. From the results of Fukada et al. and our observations it can be inferred that the transition temperature T_c must lie in the range: 10 K $< T_c \leq$ 65 K. Below 10 K the EPR and ESEEM signals are still measurable.

8.5 Conclusion

The attained results for the nitrogen hyperfine and quadrupole tensors of $Fe(CN)_6^{3-}$ doped into $K_3Co(CN)_6$ were unexpected. The analysis of the ESEEM spectra lead to an acceptable result only if, below the phase-transition temperature, a rotation by 54.7° around the c axis of the cyanide groups takes place. In this way the largest ^{14}N hyperfine components as well as the largest quadrupole components are directed along the iron-cyanide bonds. A second interesting feature is the slight deviation from inversion symmetry of the $Fe(CN)_6^{3-}$ complex, resulting in the occurrence of a splitting of all ESEEM lines.

The different orientation of the smallest g tensor component (g_3) in NaCl: $Fe(CN)_6^{3-}$ and in $K_3Co(CN)_6$:$Fe(CN)_6^{3-}$ points to a strong dependence of the g tensor on the electron distribution. We are currently involved in theoretical calculations to obtain a better insight in this intriguing situation [5].

We are not able to give an explanation for the observed phase transition. Additionally, it would be of interest to determine the crystal structure below the phase-transition temperature. We hope to report on both aspects in the (near) future.

The authors would like to express their gratitude towards A.A.K. Klaassen and G.E. Janssen for their substantial technical support. We would also like to thank Prof. J.S. Wood for the helpful discussions about the crystal structure, and H.T. Sommerdijk for critically reading this manuscript. Special thanks are due to Drs M.P.J.W. Clephas who performed the initial exploratory ESEEM experiments and to J. Smits, who performed the X-ray measurements.

References

[1] Wang, D.M. and de Boer, E., 1990, *J. Chem. Phys.*, **92**, 4698.

[2] Wang, D.M., Meijers, D.M., and de Boer, E., 1990, *Mol. Phys.*, **70**, 1135.

[3] Kirmse, R., Böttcher, R., Willems, J.-P., Reijerse, E.J. and de Boer, E., 1991, *J. Chem. Soc. Faraday Trans.*, **87**, 3105.

[4] Baker, J.M., Bleaney, B., Bowers, B., 1956, *Proc. phys. Soc., B*, **69**, 1216.

[5] Sommerdijk, H.T. and van der Avoird, A, *To be published.*

[6] Willems, J.-P., Clephas, M.P.J.W., and de Boer, E, 1993, *Mol. Phys.*, **80**, 607.

[7] Kohn, J.A., and Townes, W.D., 1961, *Acta Cryst.*, **14**, 617.

[8] Reynhardt, E.C., and Boeyens, J.C.A., 1972, *Acta Cryst.*, **28**, 524.

[9] Vannerberg, N.G., 1972, *Acta Chem. Scan.*. **26**, 19.

[10] Jagner, S., 1985, *Acta Chem. Scan. A*, **39**, 717.

[11] Prof. J.S. Wood, 1993-1994, Private communications.

[12] Shane J.J., 1993, *Electron Spin Echo Envelope Modulation Spectroscopy on disordered Solids*, (FEBO druk, Enschede)

[13] Fauth, J.M., Schweiger, A., Braunschweiler, L., Forrer, J. and Ernst, R.R., 1986, *J. Magn. Reson.*, **66**, 74.

[14] Keijzers, C.P., Reijerse, E.J., Stam, P., Dumond, M.F., and Gribnau, M.C.M., 1987, *J. Chem. Soc. Faraday Trans. 1*, **83**, 3493.

[15] Höfer, P., Grupp, A., Nebenfür, H. and Mehring, M., 1986, *J. Chem. Phys.*, **132**, 279.

[16] Shane, J.J., Höfer, P., Reijerse, E.J. de Boer, E., 1992, *J. Magn. Reson.*, **99**, 596.

[17] Curry, N.A., and Runciman, W.A., 1959, *Acta Cryst.*, **12**, 674.

[18] Fukada, S., Horiuchi, K., Asaji, T., and Nakamura, D., 1986, *Ber. Bunsenges. Phys. Chem.*, **90**, 22.

Samenvatting

Dit proefschrift beschrijft de resultaten van éénkristalstudies aan de diamagnetische kristallen NaCl en $K_3Co(CN)_6$, die gedoteerd zijn met het paramagnetische complex $Fe(CN)_6^{3-}$. Gebruikmakend van magnetische resonantie technieken kon informatie worden verkregen over de algemene structuur van het gastheerkristal. Bovendien was het mogelijk om gegevens te verkrijgen over de lokale structuur in de directe omgeving van het $Fe(CN)_6^{3-}$ complex. Voorts is informatie verkregen over de elektronendichtheid verdeling in het molekuul.

In het eerste hoofdstuk vindt u een korte beschouwing over magnetische resonantie technieken. In hetzelfde hoofdstuk worden eveneens de motieven beschreven die geleid hebben tot de uitvoering van dit onderzoeksproject.

De theoretische concepten ten aanzien van ENDOR (Electron Nuclear Double Resonance), triple resonantie en ESEEM (Electron Spin Echo Envelope Modulation) worden vermeld in hoofdstuk 2. In dit hoofdstuk worden ook een aantal verschillen en overeenkomsten tussen deze drie technieken opgesomd.

Een beschrijving van de experimentele opstellingen is terug te vinden in hoofdstuk 3. In dit hoofdstuk wordt eveneens aangetoond dat manipulatie van de gegevens, die gewoonlijk wordt toegepast na een ESEEM experiment, tot een foutieve interpretatie van sommige spectrale eigenschappen kan leiden. Voorts geeft dit hoofdstuk een korte beschrijving van de specifieke problemen die optreden bij het onderzoek aan éénkristallen.

Het ontwerp van een ENDOR resonator geschikt voor éénkristal studies wordt weergegeven in hoofdstuk 4. De mechanische en elektronische constructie van deze resonator wordt in grote lijnen geschetst. In dit hoofdstuk wordt voornamelijk aandacht besteed aan de constructie die geschikt is voor studies bij een temperatuur van 4.2 K, maar het ontwerp kan eenvoudig worden aangepast aan een flow cryostaat voor metingen bij verschillende temperaturen. De efficiëntie van de RF-spoel blijkt hoog en redelijk constant te zijn in een frequentiegebied van 0.3 tot 20 MHz. Metingen aan een testverbinding laten een goede stabiliteit van de basislijn zien in het eerder genoemde frequentiegebied. De signaal/ruis verhouding is zeer goed, zelfs voor kernen met een laag natuurlijk voorkomen zoals ^{13}C.

In hoofdstuk 5 worden de resultaten gegeven van een éénkristal ENDOR studie aan het $3d^5$ ($S = \frac{1}{2}$) 'low-spin' complex $Fe(CN)_6^{3-}$ gedoopt in NaCl. Uit de diverse centra die veroorzaakt worden door de verschillende configuraties van de twee ladingscompenserende cation vacatures, is het orthorombische centrum I_a geselecteerd voor dit onderzoek. Dit centrum wordt gekarakteriseerd door een hoge g anisotropie. ENDOR overgangen van ^{13}C, ^{14}N en ^{23}Na zijn waargenomen: bijna alle hyperfijn- en quadrupoolkoppelingstensoren zijn bepaald. De ^{14}N spectra zijn sterk beïnvloed door de quadrupoolinteractie, die een waarde bereikt vergelijkbaar met die van de hyperfijn- en de kern-Zeemaninteractie. De oriëntatie van de hoofdwaarden van alle tensoren bevestigd zowel de D_{2h} symmetrie als de positie van de negatief geladen cation vacatures, welke verondersteld is voor het I_a centrum. De ^{13}C koppelingen zijn vrij groot, hetgeen wijst op een opmerkelijke covalentie van de Fe-C bindingen. De hyperfijn- en quadrupoolinformatie wordt gebruikt om een kwalitatieve beschrijving te geven van de spindichtheiddistributie in het $Fe(CN)_6^{3-}$ complex. Wanneer een vergelijking wordt gemaakt met andere experimentele studies aan de spindistributie, dan blijkt het effect van de vacatures groot te zijn. Voor de interpretatie van de ^{14}N quadrupool gegevens is het Townes-Dailey model toegepast.

De resultaten van triple resonantie-experimenten worden beschreven in hoofdstuk 6. De tekens van de hyperfijnkoppelingsconstanten van ^{23}Na , ^{14}N en ^{13}C blijken alle gelijk te zijn.

In hoofdstuk 7 wordt aangetoond dat met behulp van EPR de polytype structuur van $K_3Co(CN)_6$ éénkristallen gedoopt met $Fe(CN)_6^{3-}$ eenvoudig kan worden bepaald. Het aantal resonantie lijnen voor een willekeurige oriëntatie van het magneetveld is indicatief voor het type van kristal dat bestudeerd wordt. Deze observaties worden gestaafd door de ons bekende kristallografische gegevens betreffende $K_3Co(CN)_6$.

Een ESEEM studie is uitgevoerd aan $Fe(CN)_6^{3-}$ gedoopt in $K_3Co(CN)_6$. De experimentele feiten vermeld in hoofdstuk 8, wijzen op een fase overgang tussen 10 en 65 K. Analyse van de ESEEM spectra gemeten bij een temperatuur van 7 K, leidt tot de conclusie dat het $Fe(CN)_6^{3-}$ ion zijn inversie centrum heeft verloren beneden de fase-overgangstemperatuur. Uitgaande van de hoekafhankelijkheid van de ESEEM lijnen kon het worden afgeleid dat, vergeleken met de structuur bij kamertemperatuur, het $M(CN)_6^{3-}$ ($M = Fe^{3+}, Co^{3+}$) complex bij lage temperatuur, gedraaid is over een hoek van 51.7° rond de c as van het kristal. Na deze rotatie vallen de hoofdwaarden van de hyperfijn- en quadrupooltensoren samen met de ijzercyanide bindingen. Dit is in overeenstemming met hetgeen kon worden verwacht op grond van eerdere ENDOR studies aan hetzelfde complex in andere soorten kristallen.

Abstract

This thesis reports about the results of single-crystal studies on the paramagnetic complex $Fe(CN)_6^{3-}$, doped into the diamagnetic hosts NaCl and $K_3Co(CN)_6$ By utilising magnetic resonance techniques, information could be obtained about the general structure of the host crystal and about the local structure around the $Fe(CN)_6^{3-}$ complex In addition, information could be obtained about the electron spin distribution over the molecule

The first chapter offers a general consideration about magnetic resonance techniques The motivations which lead to the initialisation and continuation of the research described in this thesis, can also be found in this chapter

The theoretical principles concerning ENDOR (Electron Nuclear Double Resonance), triple resonance and ESEEM (Electron Spin Echo Envelope Modulation) are described in chapter 2 Particular emphasis is given on the similarities and the differences of these three resonance techniques

Chapter 3 presents the experimental set up, both for the ENDOR and the ESEEM experiments It is demonstrated that the commonly used data manipulation performed after an ESEEM experiment, can lead to misinterpretations of some features of the resulting spectrum A short survey will be given about the specific difficulties involved when performing single crystal measurements

The design of an ENDOR resonator suitable for single crystal studies is described in chapter 4 A detailed outline is given of the mechanical and electronic construction of the resonator Special attention is given to the construction suitable for studies at 4 2 K, but the design can be easily adapted to a flow cryostat for variable temperature measurements The RF coil efficiency has been measured and is high and fairly constant over the frequency range from 0 3 to 20 MHz Measurements on a test compound, show that the baseline stability is good over the frequency range mentioned above Even for low abundant nuclei as ^{13}C , the signal to noise ratio is very good

Chapter 5 reports about a single-crystal ENDOR study on the $3d^5$ ($S=\frac{1}{2}$) low-spin complex $Fe(CN)_6^{3-}$ doped into NaCl Among the various centres caused by different configurations of two charge-compensating cation vacancies, the orthorhombic centre, I_a, which is characterised by a large g anisotropy, has been selected for this investigation ENDOR transitions due to ^{13}C , ^{14}N and ^{23}Na have been observed, nearly all hyperfine and nuclear quadrupole coupling tensors were determined The ^{14}N spectra are strongly influenced by the nuclear quadrupole interaction which reaches a magnitude comparable to that of the hyperfine and nuclear Zeeman interaction The orientations of the principal axes of all tensors confirm the D_{2h} symmetry and the corresponding positions of the negatively charged cation vacancies assumed for the centre I_a The ^{13}C couplings are quite large, indicating a noticeable covalency of the Fe-C bonds The hyperfine and nuclear quadrupole

data are used to discuss qualitatively the spin density distribution in the $Fe(CN)_6^{3-}$ unit. Comparison with other experimental studies on the spin distribution reveal that the effect of the vacancies on the spin distribution is large. For interpretation of the ^{14}N quadrupole data the Townes-Dailey model has been applied.

The results of triple resonance experiments are described in chapter 6. The signs of the hyperfine coupling constants of ^{23}Na , ^{14}N and ^{13}C are found to be equal.

In chapter 7 it is shown that with EPR the polytype structure of $K_3Co(CN)_6$ single crystals doped with $Fe(CN)_6^{3-}$ can be determined easily. The number of resonance lines for an arbitrary orientation of the magnetic field is indicative for the type of crystal studied. This is substantiated by the known crystallographic data concerning $K_3Co(CN)_6$.

An ESEEM study has been performed on $Fe(CN)_6^{3-}$ doped into $K_3Co(CN)_6$. The experimental facts revealed in chapter 8 indicate that a phase transition occurs between 10 and 65 K. Analysis of the ESEEM spectra measured at 7 K leads to the conclusion that the $Fe(CN)_6^{3-}$ ion has lost its inversion centre below the phase-transition temperature. From the angular dependence of the ESEEM lines it was inferred that, compared with the structure at room temperature the $M(CN)_6^{3-}$ ($M = Fe^{3+}$, Co^{3+}) unit at low temperature is rotated by an angle of 54.7° around the c axis of the crystal. After this rotation the major principal axes of the hyperfine and quadrupole tensors coincide with the iron-cyanide bonds. This is in agreement with what could be expected on the basis of earlier ENDOR studies of the same complex in other hosts.

Curriculum Vitae

1967: Geboren te Nijmegen op 27 juni.

1979 - 1984: HAVO aan het Elshofcollege in Nijmegen.

1984 - 1986: VWO aan het Elshofcollege in Nijmegen.

1986 - 1990: Studie Natuurkunde aan de KUN.
Het propedeutisch examen werd behaald op 31 augustus 1987. Het doctoraal examen vond plaats op 26 september 1990. Het afstudeeronderzoek is verricht op de afdeling Experimentele Vaste Stof Fysica 2 o.l.v. Prof. Dr. H. van Kempen. Dit onderzoek behelsde infrarood spectroscopie aan hoge T_c supergeleiders.

1991 - 1995: Promotie onderzoek aan de KUN o.l.v. Prof. Dr. E. de Boer op de afdeling Molecuul Spectroscopie.